

**DEVELOPMENT OF AN IMPROVED DISSIPATIVE PASSIVE
HAPTIC DISPLAY**

**A Thesis
Presented to
The Academic Faculty**

by

Matthew Robert Reed

**In Partial Fulfillment
of the Requirements for the Degree
Master of Science in Mechanical Engineering**

**Georgia Institute of Technology
November 2003**

DEVELOPMENT OF AN IMPROVED DISSIPATIVE PASSIVE HAPTIC DISPLAY

Approved by:

Dr. Wayne Book, Advisor, 11/12/03

Dr. Imme Ebert-Uphoff, 11/12/03

Dr. Aldo Ferri, 11/12/03

ACKNOWLEDGMENTS

I would first like to thank my advisor, Dr. Wayne Book, for his support of this research. His knowledge and experience were critical to the completion of this project. I would also like to thank my committee members, Dr. Imme Ebert-Uphoff and Dr. Aldo Ferri, for their assistance.

Special thanks also goes my colleagues in the Intelligent Machine Dynamics Laboratory and surrounding labs for the contributions they made to this research. They include, but are not limited to, L.J. Tognetti, Steve Askins, Davin Swanson, and Kris Kozak.

Acknowledgment must also be made to John Graham and Donald Long in the machine shop for their cooperation in the fabrication process.

This project was partially supported by the HUSCO/Ramirez Chair in Fluid Power and Motion Control.

TABLE OF CONTENTS

ACKNOWLEDGMENTS	iii
LIST OF TABLES	viii
LIST OF FIGURES	ix
SUMMARY	xiii
CHAPTER 1 INTRODUCTION.....	1
1.1 Haptic Displays.....	1
1.2 Research Goals.....	5
1.3 Organization.....	6
CHAPTER 2 BACKGROUND	8
2.1 Controllable Fluids.....	8
2.1.1 Fluid Comparison	8
2.1.2 MR Fluid Modeling.....	9
2.2 Passive Haptic Displays.....	10
2.2.1 Existing Designs	11
2.2.2 PTER Control History	13
CHAPTER 3 BRAKE MODELING.....	18
3.1 Brake Selection	18
3.2 Experimental Setup.....	19
3.3 Initial Testing.....	20
3.3.1 Current Step.....	20
3.3.2 Speed Ramp.....	22

3.3.3 Sinusoidal Motion.....	23
3.4 Model Development.....	25
3.4.1 Torque Gain.....	26
3.4.2 Time Constant.....	29
3.4.3 Backlash Modeling.....	33
3.5 Model Verification.....	34
3.6 SDOF Control Experiments.....	37
CHAPTER 4 ROBOT DESIGN.....	41
4.1 Selection Criteria	41
4.2 Design Concepts	42
4.2.1 X-Y Table	42
4.2.2 Scaled PTER.....	43
4.2.3 Three-Brake Five-Bar Linkage.....	44
4.2.4 Four-Brake Five-Bar Linkage	45
4.3 Selection of Robot Geometry.....	46
4.4 Mechanical Design.....	53
4.5 Singularity Analysis and Joint Constraints.....	56
4.6 Equipment Selection	59
CHAPTER 5 ROBOT MODELING AND SIMULATION.....	60
5.1 Kinematics	60
5.1.1 Forward Kinematics	60
5.1.2 Inverse Kinematics	63
5.1.3 Jacobian	66

5.2	Equations of Motion	67
5.3	Simulation.....	72
5.3.1	Encoders	72
5.3.2	Forward Kinematics and Velocity.....	73
5.3.3	Controller.....	73
5.3.4	Brakes	74
5.3.5	Acceleration.....	74
5.4	Simulation Verification.....	77
CHAPTER 6 CONTROLLER DEVELOPMENT AND TESTING		81
6.1	Controller Design.....	81
6.1.1	Desired Velocity	82
6.1.2	Velocity Control	82
6.1.3	Jacobian	85
6.1.4	Current Gain	85
6.2	SDOF Velocity Control	85
6.3	Proportional Velocity Control.....	87
6.4	Simulation Proof of Concept	90
6.5	Preliminary Testing.....	95
6.5.1	Experiment Design	95
6.5.2	Performance Evaluation	98
6.6	Results.....	100
CHAPTER 7 CONCLUSIONS AND FUTURE WORK		105
7.1	Conclusions	105

7.2	Contributions	107
7.3	Future Work.....	109
APPENDIX A	DERIVATION OF EQUATIONS OF MOTION	112
APPENDIX B	ROBOT SIMULATION VERIFICATION RESULTS.....	118
APPENDIX C	RESULTS FROM HUMAN OPERATOR EXPERIMENTS.....	128
REFERENCES		131

LIST OF TABLES

2.1	ER and MR Fluid Comparison.....	9
3.1	Backlash Width for Each Brake.....	23
3.2	Torque Gain Curve Fit Data.....	27
3.3	Time Constant Surface Fit Data.....	33
4.1	Robot Dimensions.....	50
4.2	Joint Angle Ranges	58
5.1	Key Dimensions and Variables for Robot Model.....	72
6.1	Control Methods	96
6.2	Controller Abbreviations.....	102
C.1	Average Performance Metrics for Human Operator 1 in 3-Brake Configuration	129
C.2	Average Performance Metrics for Human Operator 2 in 3-Brake Configuration	129
C.3	Average Performance Metrics for Human Operator 3 in 3-Brake Configuration	129
C.4	Average Performance Metrics for Human Operator 1 in 4-Brake Configuration	130
C.5	Average Performance Metrics for Human Operator 2 in 4-Brake Configuration	130
C.6	Average Performance Metrics for Human Operator 3 in 4-Brake Configuration	130

LIST OF FIGURES

1.1	PTER (Passive Trajectory Enhancing Robot).....	4
2.1	Scooter Cobot.....	11
2.2	3-DOF PADyC Prototype.....	12
2.3	Dissipative Passive Haptic Display with ER Fluid Brakes.....	13
2.4	PTER (Passive Trajectory Enhancing Robot).....	14
3.1	Photograph of MR Fluid Brake.....	19
3.2a	Brake Testing Apparatus.....	20
3.2b	Close-up of Mounted Brake.....	20
3.3	Torque Response to Current Step of 0.8 A at 4 RPM.....	21
3.4	Torque Response to Ramp in Speed at 0.8 A.....	22
3.5	Torque Response to Sinusoidal Velocity at 1 Hz. and 1.0 A.....	24
3.6	Block Diagram of First Order Brake Model.....	26
3.7	Torque Gain vs. Current and Speed.....	27
3.8	Torque Gain Fit Applied to Data.....	28
3.9	Standard Deviation of Torque vs. Current.....	29
3.10	Rising Time Constant vs. Current and Speed.....	30
3.11	Falling Time Constant vs. Current and Speed.....	30
3.12	Rising Time Constant Surface Fit.....	32
3.13	Falling Time Constant Surface Fit.....	32
3.14	Backlash Schematic.....	33
3.15	Comparison of Model to Current Step Response.....	35

3.16	Comparison of Model to Sinusoidal Data.....	36
3.17	Comparison of Model to Sinusoidal Current Data.....	37
3.18	Control Experiment Apparatus	38
3.19	Open Loop Controller	39
3.20	Closed Loop Controller.....	39
3.21	Virtual Spring Control Experiment.....	40
3.22	Virtual Wall Control Experiment.....	40
4.1	X-Y Table Design Concept.....	43
4.2	PTER (Passive Trajectory Enhancing Robot).....	44
4.3	3-Brake Five-Bar Linkage	45
4.4	4-Brake Five-Bar Linkage	46
4.5	Robot Geometry	47
4.6a	Illustration of Unachievable Forces with Two Brakes.....	48
4.6b	Illustration of Unachievable Forces with Four Brakes	48
4.7	Local SDOF Paths for $L_{ED} = L_{AB} = .9$	50
4.8	Contour Plot of Maximum Angle Between Local SDOF Paths for 3-Brake Configuration	51
4.9	Contour Plot of Maximum Angle Between Local SDOF Paths for 4-Brake Configuration	51
4.10	SDOF Paths for 3-Brake Configuration.....	52
4.11	SDOF Paths for 4-Brake Configuration.....	52
4.12	3-Brake Assembly Drawing.....	54
4.13	4-Brake Assembly Drawing.....	54
4.14	Photograph of 3-Brake Robot	55

4.15	Photograph of 4-Brake Robot	55
4.16a	Positioning Ring and Plate Assembly	58
4.16b	Close-up of Positioning Ring and Plate Assembly	58
4.17	Workspace Boundaries	59
5.1	Key Dimensions for Forward Kinematics	62
5.2	Key Dimensions for Inverse Kinematics ($L_{AB} \neq 0$)	64
5.3	Key Dimensions for Inverse Kinematics ($L_{AB} = 0$)	65
5.4	Key Dimensions and Variables for Robot Model	71
5.5	Block Diagram for Robot Simulation	73
5.6	Schematic of Model Verification Tests	77
5.7a	Comparison of Model to Data for 3-Brake Configuration with Free Motion.....	79
5.7b	Comparison of Model to Data for 3-Brake Configuration with Brake A Locked.....	79
5.8a	Comparison of Model to Data for 4-Brake Configuration with Free Motion.....	80
5.8b	Comparison of Model to Data for 4-Brake Configuration with Brake A Locked.....	80
6.1	Controller Block Diagram.....	82
6.2	Sample Desired Velocity Field	83
6.3	SDOF Velocity Control Schematic.....	87
6.4	Proportional Velocity Control Schematic.....	88
6.5	SDOF Velocity Control Simulation for 3-Brake Configuration.....	91
6.6	SDOF Velocity Control Simulation for 4-Brake Configuration.....	92
6.7	Proportional Velocity Control Simulation for 3-Brake Configuration	93
6.8	Proportional Velocity Control Simulation for 4-Brake Configuration	94

6.9	Experimental Setup for Human Subject Tests	96
6.10	User Interface	97
6.11	Desired Paths Selected for Control Experiments	98
6.12	Sample of Human Subject Data Using Low Gain Proportional Velocity Control in the 3-Brake Configuration	101
6.13	Average Path Error by Configuration and Controller	103
6.14	Average Tip Force by Configuration and Controller	104
6.15	DFT Sum of Acceleration by Configuration and Controller	104
B.1	3-Brake Configuration Free Motion	119
B.2	3-Brake Configuration with Brake A Locked	120
B.3	3-Brake Configuration with Brake E Locked	121
B.4	3-Brake Configuration with Brake B Locked	122
B.5	4-Brake Configuration Free Motion	123
B.6	4-Brake Configuration with Brake A Locked	124
B.7	4-Brake Configuration with Brake E Locked	125
B.8	4-Brake Configuration with Brake B Locked	126
B.9	4-Brake Configuration with Brake C Locked	127

SUMMARY

This project focuses on the design and modeling of a two degree-of-freedom dissipative passive haptic display. Haptic displays are man-machine interfaces that transmit forces to the human operator. A dissipative passive haptic display is one that may only remove energy from the system using actuators such as brakes and dampers, thus ensuring the safety of the human operator. These devices may be used to implement virtual constraints such as desired paths and obstacles. Traditional friction brakes have previously been used as dissipative and coupling elements in a two degree-of-freedom parallel manipulator, resulting in undesired effects such as vibration, stiction, and slow response times. Alternatively, the new robot is actuated by rheological brakes, which feature fast response times and smooth application of torque. This approach aims to improve upon the accuracy and “feel” of the previous design.

A commercial magnetorheological (MR) fluid brake was selected and put through an extensive series of tests. The data was used to develop a model that characterizes MR fluid behavior in low speed braking applications. A parallel five bar linkage was designed and built that has separate configurations corresponding to 3-brake and 4-brake operation. The length of each arm was chosen by means of a geometrical optimization that weighs the size and area of the workspace and actuator effects. A simulation was then developed by incorporating the brake model into the equations of motion of the robot. Next, two forms of path following velocity control were devised and tested in simulation. Finally, the accuracy, workload, and smoothness of both controllers and both configurations were examined in preliminary tests with human operators.

CHAPTER 1

INTRODUCTION

1.1 Haptic Displays

Haptic interfaces comprise a broad range of robotic mechanisms that aid humans in performing certain tasks by interacting directly with the user's sense of touch. They are designed to give the user tactile cues regarding the operation being performed. This extra information can help the user to perform a task faster, more safely, and with greater accuracy. For example, imagine an automobile that generates additional torque on the steering wheel if it detects that the yellow line is crossed or that a passing automobile is too close. Many passive haptic displays give the user the option of overriding the control by applying additional force in the appropriate direction. Such action may need to be taken in order to prevent injury to a nearby person or piece of equipment in the event of controller error or other unexpected circumstance. Applications for these devices include teleoperation [5], vehicle control [15], medical training devices [20], computer-assisted surgery [3], and physical therapy [9].

Large-scale robotic mechanisms that are capable of generating large forces pose a potential risk to the human operator, particularly if they become unstable. Stability of the system and safety of the human operator can be ensured by making the device energetically passive. Passive devices are also useful in delicate operations such as robot-assisted surgery, where it is advantageous to keep the motive force in the hands of the surgeon. Unlike active robots that can add energy to the system via electric motors,

hydraulic power, and other mechanisms, passive devices may only dissipate, redirect, or store energy using actuators such as brakes, dampers, and continuously variable transmissions (CVTs).

An active device generally has actuators equal in number to its degrees of freedom and may apply force in any direction when not in a singular position. A passive device, on the other hand, is limited in that it may only apply force in a direction that opposes velocity. In order to compensate for this limitation, additional actuators may be used in order to increase the range of directions in which force can be applied. Many dissipative devices also have the ability to lock an actuator. By doing so, the robot is effectively reduced to a single degree of freedom (SDOF) system. Thus the number of SDOF paths available for selection at each point in the workspace can be increased by using additional actuators.

Passive haptic displays are designed for the purpose of implementing programmable constraints. In two degrees of freedom, this includes simulating paths and hard obstacles such as walls. In path following exercises, the device should ideally guide the user along a smooth and frictionless path regardless of the direction of force applied at the handle. One application of this technology is rehabilitation exercises for the upper limbs. For instance, the device can be programmed for a path following exercise and the patient can move the manipulator along the path with the assistance of the machine. As the patient begins to experience restored motor function, the degree to which the device aids in the path following can be reduced until the patient is able to negotiate the path without assistance.

Alternatively, in obstacle avoidance exercises, it is essential to transmit a sudden increase in force in the appropriate direction at the point of impact in order to alert the user of the obstacle's location. After the collision, the user should ideally be allowed to trace along the edge of the obstacle and feel a hard, smooth surface. When not in contact with the obstacle, the user should be able to move the tip in an unconstrained fashion. This type of control has applications in computer-assisted surgery, for instance, where the surgeon's tool may be restricted to operate only within a predetermined region.

Passive haptic displays can generally be divided into two classes: steerable and dissipative. A dissipative device has actuators such as brakes or dampers that attempt to redirect the user by removing energy from the system. A steerable device is always constrained to move in a number of kinematic degrees of freedom fewer than that of its workspace. They use continuously variable transmissions (CVTs) or motorized castors in order to restrict the user's motion. Unlike dissipative devices, steerable devices are capable of near perfect path following control. Control techniques involve the relatively simple task of motor positioning control. Conversely, steerable devices do a poor job of simulating impacts with walls or other obstacles because the device must essentially steer the user around it. Also, they are incapable of true free motion. They must sense the direction of applied force and steer in that direction. Dissipative displays, on the other hand, excel at simulating impacts with walls and obstacles because they generally have the ability to lock an actuator. Also, when nothing is actuated, the system allows full range of movement in all available degrees of freedom. The challenge in dissipative passive haptic displays lies in path following control.

PTER (Passive Trajectory Enhancing Robot), shown in Figure 1.1, is a dissipative passive haptic display designed and constructed by Charles at the Georgia Institute of Technology [2]. It is a two degree-of-freedom (DOF) parallel five-bar linkage that operates in a horizontal plane. The user grasps the handle, which is equipped with a force sensor, in order to move the tip within the workspace. It is actuated by four electromagnetic dry friction clutches located on the central axis that exert forces on the handle. Clutches 1 and 2 independently brake links A and B, respectively. Clutches 3 and 4 provide direct and reverse coupling of links A and B. Thus PTER is capable of locking the tip into any one of four local SDOF paths in the workspace or generating a net force from some combination of the four clutch torques. PTER has been used as a testbed for evaluating path following and obstacle avoidance tasks for dissipative passive haptic displays.

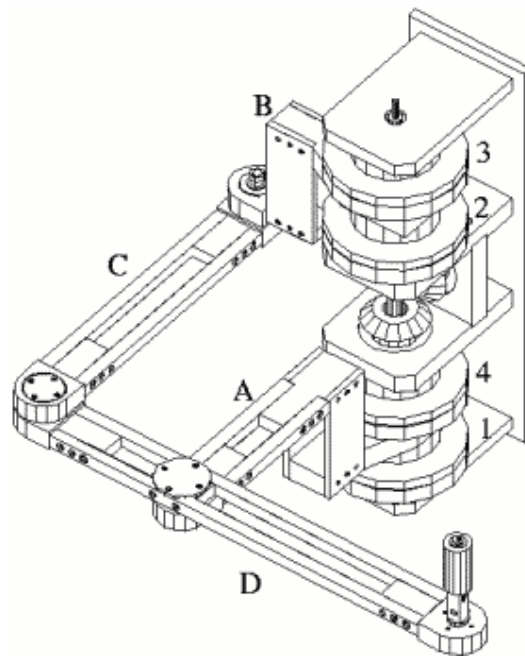


Figure 1.1. PTER (Passive Trajectory Enhancing Robot)

The performance of PTER is limited primarily by its actuators. Torque is generated by mechanical contact, which often adds vibration to the system, particularly when activated by a rapidly switching controller. Furthermore, the friction material has a higher kinetic coefficient of friction than static, resulting in stick-slip behavior. This phenomenon has led to discontinuity in braking torques [17]. Control is further complicated by large response times and time delays. Tognetti, Munir, and Book investigated several alternative braking methods with the intent of eliminating or improving some of these problems [16, 24]. None of these methods was deemed an improvement over the existing system. However, later research by Vallabh identified a viable braking alternative in controllable fluids [26].

Electrorheological (ER) and magnetorheological (MR) fluids belong to a class of controllable fluids that achieve rapid and reversible changes in rheological properties with the application of an electric or magnetic field, respectively. They consist of colloidal suspensions of polarizable or magnetizable particles that form structural chains parallel to the field. Thus shear stress can be controlled by modulating the field intensity. In actuators utilizing this technology, the moving parts are surrounded by a thin layer of fluid. Therefore there is no mechanical contact, resulting in smooth transitions between shear stress levels.

1.2 Research Goals

The goal of this project was to design, model, fabricate, and perform initial tests on an improved dissipative passive haptic display using controllable fluid brakes as actuators. The use of fluid brakes could virtually eliminate the jerky feel of the system while

decreasing response time. The first step was to research and select a fluid actuator that met the design criteria and determine its effectiveness for this application. This was accomplished through an extensive series of tests, which were used to generate a model that characterized fluid behavior in a low-speed braking device. The brake model is a key component in the overall robot simulation, which is a valuable tool for the assessment of new control techniques and mechanical changes. The mechanical design was derived from previous passive haptic display designs. The design goals were to maintain all the functional aspects of PTER while simplifying and reducing the size of the device. Two forms of velocity control were devised in simulation with the aim of minimizing position error. Once construction of the device was complete, the effectiveness of these controllers was evaluated in a preliminary series of tests with human operators.

1.3 Organization

The development and testing of the robot is discussed thoroughly in the remaining chapters. Chapter 2 presents an overview of controllable fluids and passive haptic display designs and control techniques. Chapter 3 discusses the selection of the actuator and the testing procedure that was used to develop the brake model. Some simple SDOF control experiments are shown that demonstrate the effectiveness of open loop control. Chapter 4 presents the selection of a two-configuration robot design from four design concepts. It also discusses the process by which the arm lengths were chosen as well as other design considerations. Chapter 5 describes the modeling and simulation of the robot and compares the results to experimental data. In Chapter 6, an overall framework

for path following velocity control is presented along with two specific velocity control techniques. Preliminary results with human operators are used to quantitatively compare the accuracy, workload, and smoothness of the controllers and configurations using a set of proven performance metrics. Finally, the contributions of this work and recommendations for future work are discussed in Chapter 7.

CHAPTER 2

BACKGROUND

The background information in this chapter is divided into two main sections. The first discusses and compares the properties of ER and MR fluids and gives an overview of MR fluid modeling. The second section describes existing passive haptic displays and associated control techniques.

2.1 Controllable Fluids

Vallabh developed an ER fluid brake in order to evaluate its potential as an actuator in a passive haptic display [26]. The brake fell short of the desired maximum braking torque of 5 Nm. It also had a much larger response time than those reported in literature. However, the smoothness in operation warranted further investigation into controllable fluids. This section presents an overall comparison of the properties of ER and MR fluids. Then some common techniques for the modeling of MR fluids are presented.

2.1.1 Fluid Comparison

Table 2.1 shows a comparison of some key properties of ER and MR fluids [12]. Most notably, MR fluids are capable of much higher yield stresses than ER fluids. This means a much smaller MR fluid actuator is needed for any given application. MR fluids also have a larger operable temperature range and a better tolerance for impurities. A search of U.S. manufacturers of controllable fluids identified Lord Corporation as the only

source. Lord Corporation specializes in the development of MR fluids and MR fluid devices. All of these factors make MR fluids the obvious choice among the controllable fluids.

Table 2.1. ER and MR Fluid Comparison

Property	ER	MR
Yield Stress	2 - 5 kPa	50 - 100 kPa
Power Requirement	2 - 5 kV at 1 - 2 mA	2 - 25 V at 1 - 2 A
Response Time	several milliseconds	several milliseconds
Availability	0 known suppliers	1 known supplier
Intolerance for Impurities	Poor	Good
Operable Temperature Range	10 - 90° C	-40 - 150° C

When working with MR fluids, it is important to be aware of their limitations. For instance, if left unused for a long period of time, particle settling may result. Also, in-use thickening may occur if MR fluids are subjected to high stress and shear rates for a long period of time [13]. Both of these phenomena may lead to a decline in performance. Additionally, yield stress has been shown to decrease with increases in temperature [10].

2.1.2 MR Fluid Modeling

Selection of a model for an actuator depends on how that actuator will be used. Therefore, several researchers develop empirical models by fitting equations to experimental data under a select range of operating conditions. For example, Madhavan, Kamath, and Wereley have developed two phenomenological models that characterize the behavior of MR fluids in helicopter rotor dampers [14].

Other researchers take a more analytical approach to MR fluid modeling. Many base their models on the Bingham plastic equation [8],

$$\tau = \eta\dot{\gamma} + \tau_y(H)\text{sign}(\dot{\gamma}), \quad (2.1)$$

where τ is the shear stress, η is the dynamic viscosity, $\dot{\gamma}$ is the shear rate, τ_y is the yield stress, and H is the magnetic field strength. This model consists of a constant viscous component along with a yield stress component that depends on magnetic field strength. The yield stress is commonly determined by Rosensweig's laminae model,

$$\tau_y = \frac{\mu_0 H^2}{4} \left[\frac{\phi(1-\phi)\chi_m^2}{1+(1-\phi)\chi_m} \right], \quad (2.2)$$

where μ_0 is the vacuum permeability, ϕ is the volume fraction of iron particles, and χ_m is the susceptibility of a magnetic material laminae. The bracketed expression in Equation 2.2 is a constant for the actuator. Therefore the laminae model predicts that yield stress is proportional to the square of magnetic field strength. Since magnetic field intensity is proportional to the current through a coil, the yield stress is also proportional to the square of current.

2.2 Passive Haptic Displays

This section first provides an overview of three existing passive haptic displays and their control strategies. Next, a complete history of control techniques used with PTER are presented. Particular emphasis is placed on PTER due to the availability of information and similarity to this project.

2.2.1 Existing Designs

Figure 2.1 shows an example of a 3-DOF steerable passive haptic display. Dubbed Scooter, this device belongs to a group of cobots (collaborative robots) developed by Moore, Peshkin, and Colgate at Northwestern University [16]. It is operated by grasping the handle at the center of the device and rolling it along the surface upon which it rests. It is a nonholonomic device that constrains the user to a single kinematic degree of freedom using three motorized castors.

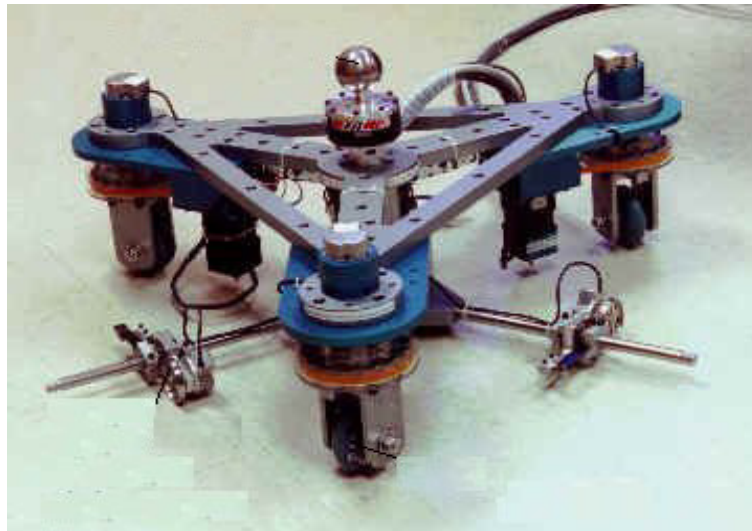


Figure 2.1. Scooter Cobot

PADyC (Passive Arm with Dynamic Constraints) is a concept being developed by a team at TIMC Laboratory in Grenoble, France for a 6-DOF robotic arm designed for cardiac puncturing [19]. It features a pair of motorized overrunning clutches for each joint. Each pair of clutches is driven in opposite directions in order to place velocity limits on each joint. PADyC has four principal modes of operation. Free mode allows unconstrained motion of the tip. Position mode helps the user move the tool to the

desired position and orientation. Trajectory mode constrains the user along a predefined path. Region mode restricts motion to a specified region in the workspace. These control techniques have been implemented and tested on a 3-DOF prototype, shown in Figure 2.2.

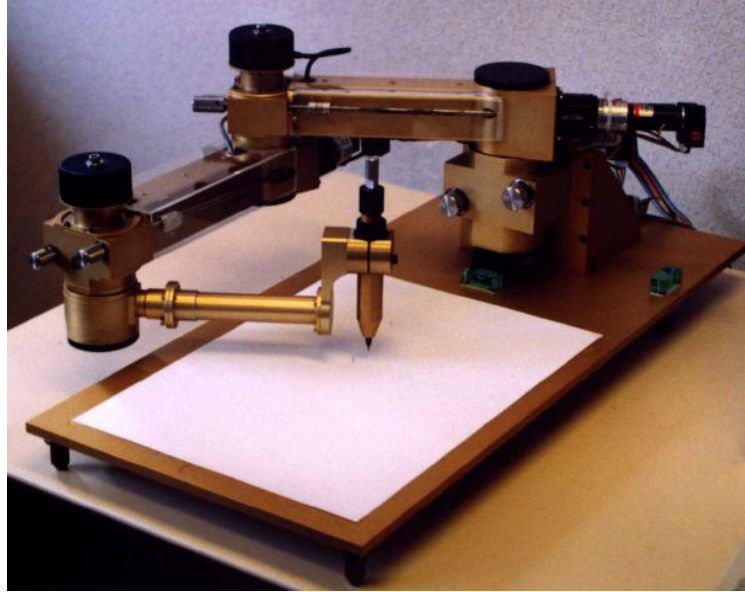


Figure 2.2. 3-DOF PADyC Prototype

Figure 2.3 shows a dissipative passive haptic display developed by Sakaguchi, Furusho, and Takesue at Osaka University in Japan [18]. It is a parallel five-bar linkage that is actuated by two ER fluid brakes. They are connected by a belt and pulley mechanism to separate links on the robot. The user interfaces with the robot using the handle located at the bottom of the figure. This device has been used to simulate virtual walls and collisions with virtual objects. In both cases, the device simply locks both actuators when the tip reaches the appropriate position. It has also been used in an

experiment where the user traces over a virtual wall. In this case, the robot alternately actuates each brake when the tip enters a predefined track at the edge of the wall.



Figure 2.3. Dissipative Passive Haptic Display with ER Fluid Brakes

2.2.2 PTER Control History

PTER, shown in Figure 2.4, was introduced in Chapter 1. Extensive work has been done with controller development for PTER. Most of the initial work focused on the adaptation of an active impedance control law. Impedance control determines the desired force to be applied to the handle from the position and velocity of the tip relative to the desired path.

Charles designed an impedance controller with a virtual parallel spring and damper resisting motion perpendicular to the path and a virtual damper resisting motion parallel to the path [2]. Since PTER is passive, it is limited in that it may only apply forces that

oppose velocity. For instance, the spring force can only be modeled as the tip moves away from path. Also, in some instances the controller is unable to compose the desired force vector out of the available forces from each clutch. The difficulty then lies in choosing which clutches to actuate in these circumstances. Charles solved this problem by establishing a set of upper and lower bounds for the torque generated by each clutch in terms of the desired torque. If a set of joint torques lie within the bounded regions of all clutches, a valid solution exists, and a set of joint torques near the center of the bounded region is selected. If a valid solution does not exist, the controller selects a set of joint torques that lie close to the valid region. Charles implemented this controller in circular path following exercises in simulation only.

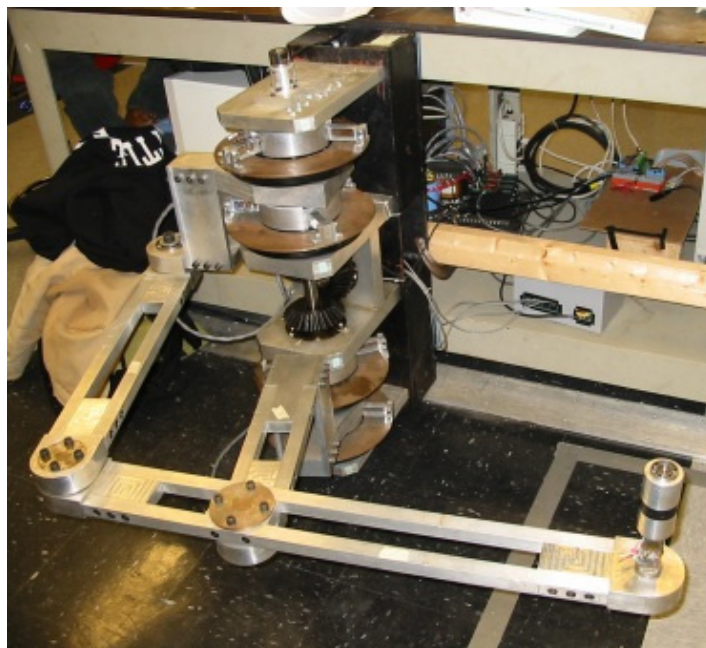


Figure 2.4. PTER (Passive Trajectory Enhancing Robot)

Davis simplified the torque selection process with the torque translator [4]. The torque translator graphically analyzes the effect of each torque on the relative angular velocities of the base joints. This method showed that if a valid solution exists, the desired force direction can be generated by at most two clutches. If a valid set of joint torques cannot be found, the controller tries to generate only the perpendicular or parallel desired force component. The updated impedance controller was implemented for circular path following exercises both in simulation and on the testbed.

Gomes made several changes to the impedance controller in an effort to reduce the “jerky feel” of the previous method [6]. First, the impedance was modeled simply as a virtual spring aligned perpendicular to the path. The torque translation algorithm was also modified such that the system was analyzed in tip space rather than joint space. Furthermore, a blending algorithm was added to the controller in order to ease the transition between clutches and lessen the vibration felt at the tip. These changes had minimal impact on performance. Gomes also introduced a basic form of velocity control with limited success.

Swanson developed a detailed simulation for PTER, including accurate models of the actuator dynamics [22]. The new simulation was used to test the impedance controller and torque translator algorithm with torque feedback control of the clutches. Also tested was a form of velocity control. Desired velocity was determined as a function of distance from the desired path. The controller then selects the clutch with the force component pointing in the direction closest to that of the desired velocity. The performance of each of these controllers was evaluated in simulation for a simple line following task. The

feedback control improved the accuracy of the impedance controller, yet even better results were obtained with the velocity controller.

Swanson and Book implemented two types of obstacle control on PTER [21]. By locking an actuator, PTER constrains the tip to move in a SDOF path. The SDOF controller operates by enclosing the obstacle with a set of these SDOF paths. When the tip position crosses the obstacle boundary, the controller simply actuates the corresponding clutch and the user is guided around the obstacle. If the controller then detects that the user is applying force away from the obstacle, the clutch will be released and free motion will resume. A form of velocity control was also tested for obstacle avoidance tasks on PTER. When the tip penetrates the obstacle boundary, the controller commands a force that will act to drive the velocity to the direction of the tangent to the obstacle surface. The desired force lies perpendicular to the actual velocity. A clutch or set of clutches is actuated such that the generated force direction is closest to that of the desired force. In the event that no set of clutches can generate a force with a component perpendicular to actual velocity, the system is immobilized by commanding high torque from two clutches. When force is detected in a direction pointing away from the obstacle, the controller will release the clutches and allow free motion.

In a later work, Swanson developed two new control techniques [23]. Each controller determines the desired velocity direction using a velocity field that linearly blends velocity toward the desired path. In velocity ratio control, the desired velocity is translated into a set of link velocities. The ratio of desired to actual velocity for each link is computed and normalized by the highest positive term. The links with ratios less than 1 are actuated in order drive their ratio toward 1 by slowing them down. If coupling

actuators are used, the velocity ratio controller first checks to see if any coupling actuators produce the desired effect on the link velocities. This is accomplished by comparing a vector of influence coefficients relating the signs of acceleration generated by the clutches to the signs of acceleration needed by the links to reach the desired velocity ratio. Swanson also introduced a form of optimal control for dissipative passive haptic displays. The optimal controller seeks to minimize a cost function based on the angle between desired and actual velocity and the change in kinetic energy. Inclusion of the second term ensures that greater priority is placed on the selection of coupling actuators.

Human subject testing was used to evaluate the velocity ratio and optimal controllers in terms of accuracy, speed, and user fatigue. A variety of paths consisting of line segments and arcs were tested. The highest level of accuracy was achieved with the velocity ratio controller, yet it resulted in slow completion times and high levels of input force at high gains. The subjects of these experiments were asked to complete a survey regarding the level of workload and smoothness of each task. The results were statistically analyzed in order to identify relationships with the experimental data. The result was a set of performance metrics that can be used to evaluate the performance of a haptic display. Most importantly, Swanson found strong correlations between average input force and total workload, and the frequency content of acceleration and smoothness.

For a more comprehensive survey of designs and applications for passive haptic displays, the reader should refer to [23].

CHAPTER 3

BRAKE MODELING

A complete understanding of low-speed MR fluid brake behavior is needed in order to effectively predict the behavior of the robot and test control methods. This chapter discusses the development of an empirical model relating torque output to applied current and shaft position and velocity. The model results are then compared to experimental data. Finally, the results of simple SDOF torque control experiments are presented which demonstrate the effectiveness of this actuator for the desired application.

3.1 Brake Selection

A thorough investigation identified Lord Corporation as the only U.S. manufacturer of controllable fluids. Lord Corporation specializes in the production of MR fluids and MR fluid devices. An MR fluid brake (Lord MRB-2107-3), shown in Figure 3.1, was selected because its characteristics closely match those required by the robot. It is approximately 9.2 cm in diameter, features a through shaft of length 14 cm, and has a mass of 1.41 kg. The rated torque output is 5.6 Nm at 1 A. One peculiar aspect of the brake is that it features backlash “by design” [11]. The backlash is simply a deadband through which the shaft must travel when the direction of motion changes where the torque output drops to its off-state (zero current) value.

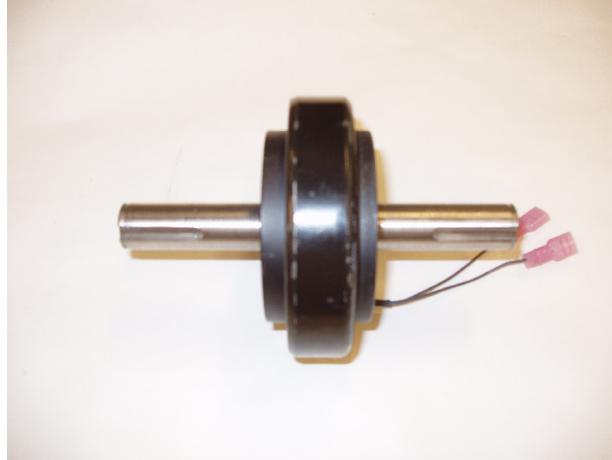


Figure 3.1. Photograph of MR Fluid Brake

3.2 Experimental Setup

Four MR fluid brakes were tested on a converted apparatus that was originally used to test an ER fluid brake. The equipment and mounted brake are shown in Figures 3.2a and 3.2b, respectively. Each brake is powered by an Advanced Motion Controls 12A8 PWM amplifier and accompanying PS4X300W power supply. The amplifiers feature a current feedback loop and are adjusted to 1 A continuous output. The brake housing is mounted to a Himmelstein & Co. 2020(24-1) torquemeter that interfaces with an Analog Devices 3B18 signal conditioning system. The brake shaft is driven by a Pacific Scientific BL2416-20-1-X-004 brushless DC motor that is operated by an SC402-001 motor controller set to torque control mode. A harmonic drive is used to provide a 100 to 1 reduction in motor speed. Motor shaft position is detected by a Lucas Ludex S-9974-1024 quadrature optical encoder with 1024 counts per revolution. A dSPACE DS1102 floating point controller board was used to monitor and control the hardware. The controller board was interfaced using dSPACE ControlDesk software. Models were

generated in the Simulink environment of MATLAB and downloaded to the board using Real Time Workshop.

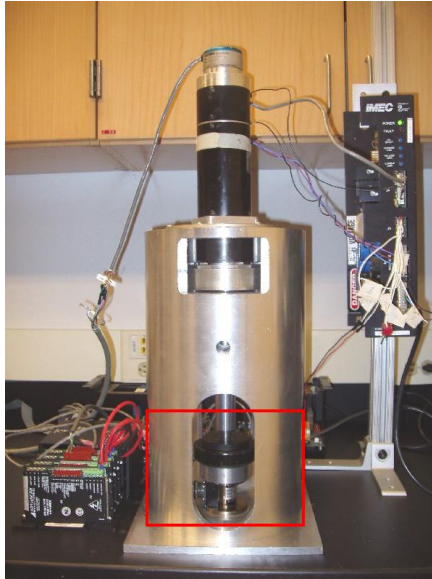


Figure 3.2a. Brake Testing Apparatus

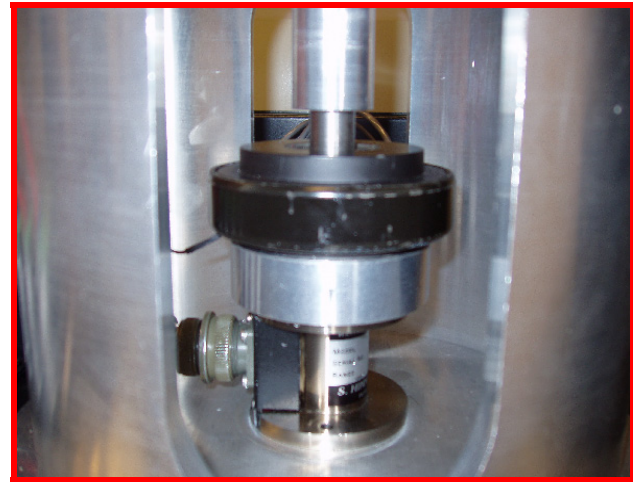


Figure 3.2b. Close-up of Mounted Brake

3.3 Initial Testing

Three tests were performed on each brake to analyze the torque output under typical operating conditions.

3.3.1 Current Step

A step in current was performed in order to observe the time response and steady state torque of the brake. The motor was controlled to maintain constant speed. Haptic devices typically move relatively slowly, with joint speeds in the range of 0 to 60 rpm. Several experiments were conducted in this speed range and in the range of 0.2 to 1 A

supplied to the brake. Figure 3.3 shows the typical response, with a step from 0 to 0.8 A at 4 rpm.

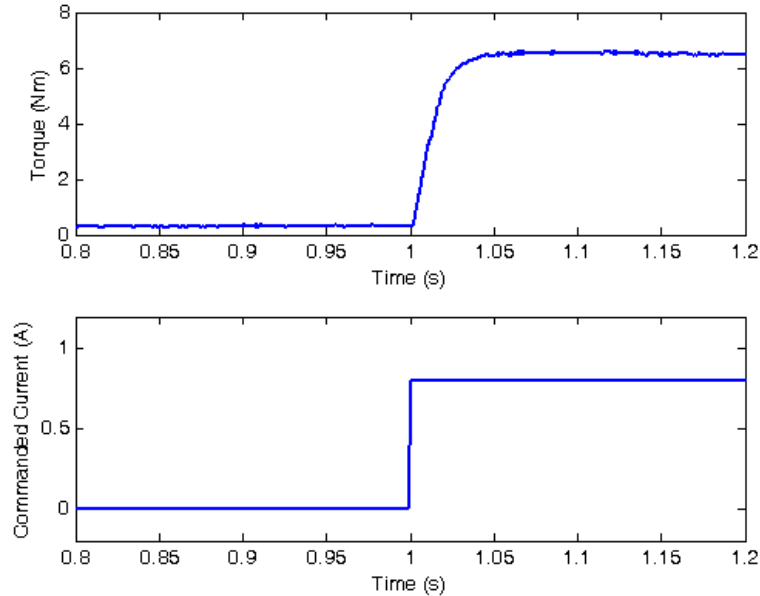


Figure 3.3. Torque Response to Current Step of 0.8 A at 4 RPM

Figure 3.3 shows that the torque output exhibits a typical first order response. In fact, the brake is essentially an RL circuit, which can be described by the following transfer function:

$$\frac{I(s)}{V(s)} = \frac{1/R}{(L/R)s + 1}, \quad (3.1)$$

where I is current, V is voltage, R is resistance, and L is inductance. With an inductance of .150 H and a resistance of 8 Ω , a time constant of 19 ms is predicted for a step in voltage [11]. If an amplifier with current feedback is used (such as the one used in these experiments), a much smaller time constant can be achieved. Preliminary experiments

revealed that larger time constants are observed at very low speeds. This issue will be discussed in greater detail in the Section 3.4.2.

3.3.2 Speed Ramp

A ramp of speed was applied to the brakes in order to test for any speed dependency in the torque output. The motor was controlled to ramp from 0 to 60 rpm while current was maintained at a constant value ranging from 0 to 1 A. Figure 3.4 shows the ramp response of one brake at .8 A and is characteristic of all cases. If a least squares linear fit is applied to the steady state region of Figure 3.4, viscous damping of .0082 Nm/rpm results. In the speed range in which the robot will normally operate this would translate to at most a few tenths of 1 Nm. Therefore speed dependence on torque output is negligible and will not be considered in the model.

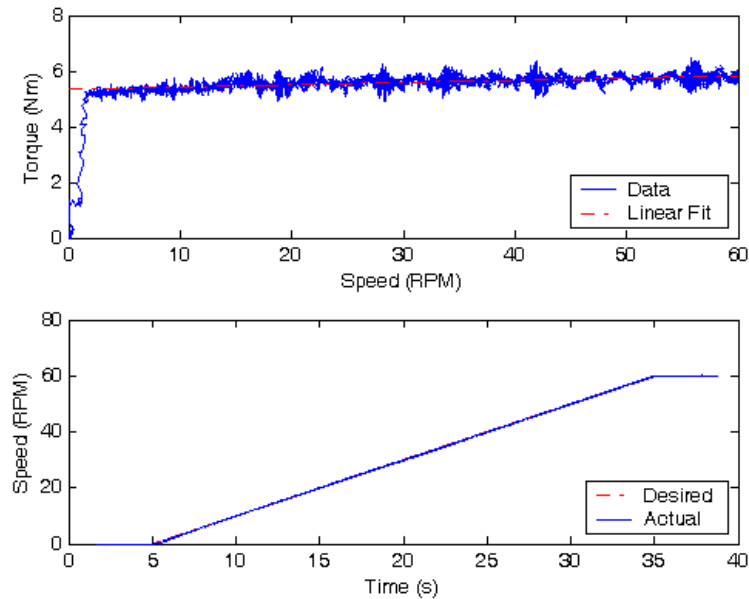


Figure 3.4. Torque Response to Ramp in Speed at 0.8 A

3.3.3 Sinusoidal Motion

Sinusoids of speed were applied to the brakes in order to observe the effects of backlash when velocity changes direction. Four experiments were conducted for each brake with frequencies of 0.25 and 1 Hz and brake currents of 0.5 and 1 A. A speed amplitude of 10 rpm was used throughout. Figure 3.5 shows the characteristic response. As velocity switches sign, the torque temporarily stalls at its off-state value before resuming normal output. The backlash can be most easily viewed in the third graph of Figure 3.5 where torque is shown vs. position. In this case it measures 1.9° . As expected, the backlash width of each brake does not vary with frequency or applied current; the only variation is due to encoder quantization error. The backlash width of each brake was determined by inspection of the torque vs. position relationship and averaged over all four trials. The results are shown in Table 3.1. The letter designates the joint in which the brake will reside in the robot, as described in the next chapter. Interestingly, brake A has no detectable backlash.

Table 3.1. Backlash Width for Each Brake

Brake	Backlash Width ($^\circ$)
A	0.0
E	1.7
B	1.5
C	1.8

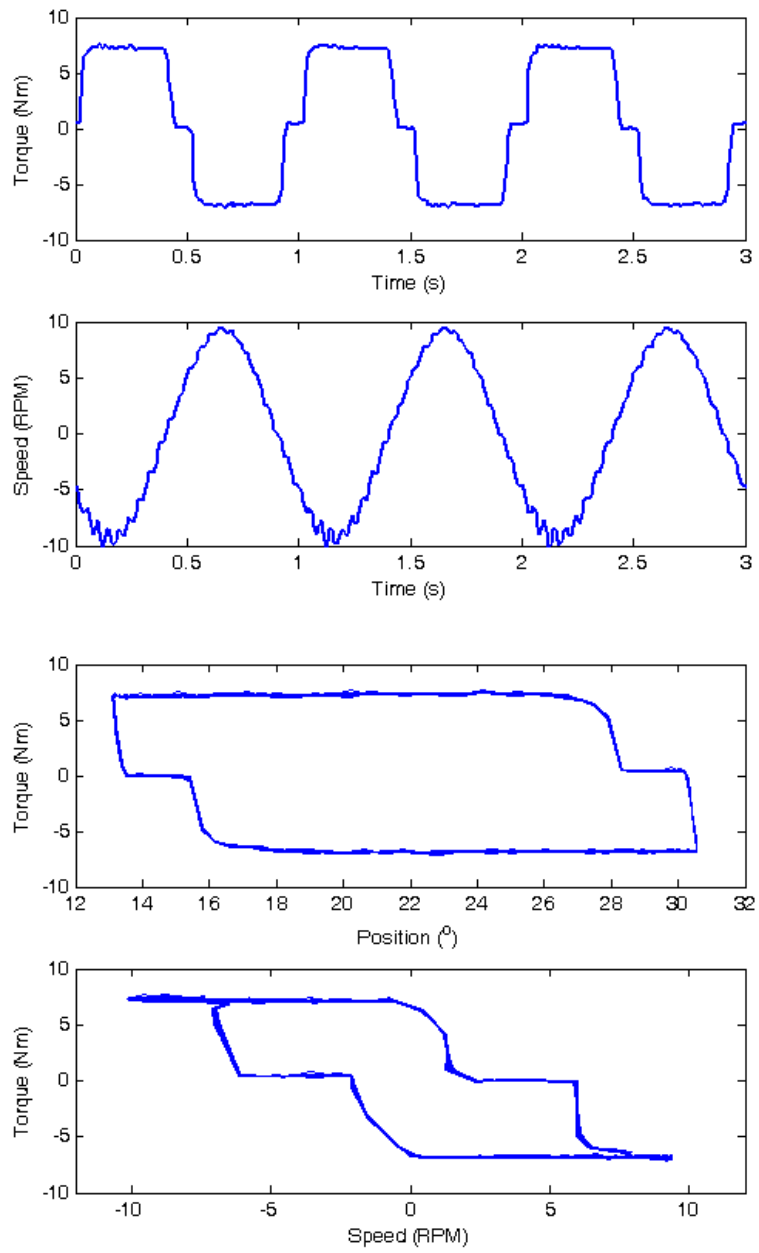


Figure 3.5. Torque Response to Sinusoidal Velocity at 1 Hz. and 1.0 A

3.4 Model Development

It is assumed that the amplifiers have a much faster response time than the MR fluid brakes. Therefore each brake and amplifier pair is modeled as a single system. Based upon the previous analysis, the following first order system model for the MR fluid brake is proposed:

$$\tau(s) = K(I, \theta, \tau_{i-1}) \frac{1}{a(I, \omega)s + 1}, \quad (3.2)$$

where

τ = torque (Nm)

I = current (A)

θ = position ($^{\circ}$)

τ = torque at last time step

K = torque gain (Nm)

a = time constant (s)

ω = velocity (rpm)

s = differential operator

Equation 3.2 is not a valid transfer function, but it can be implemented as such in numerical simulation. The terms in appearing in parentheses in the right side of the equation are the inputs to the model and are used to compute the torque gain and time constant at each time step. The torque gain is a function of the current (as discussed in Section 3.4.1) and the position and last torque value (Section 3.4.3). The time constant changes with current and velocity (Section 3.4.2).

The model parameters, K and a , were determined using current steps to the brake with speed maintained constant by the motor (same procedure as Section 3.2.1). Data was collected for a matrix of current and speed values spanning 0, 0.2, 0.4, 0.6, 0.8, and 1.0 A and 0.5, 1, 2, 4, 8, 16, 32, and 64 rpm, respectively. A logarithmic sequence was selected

for speed because the time constant was initially found to vary only at very low speeds. The sequence starts at .5 rpm because that is the lowest speed that the motor could maintain. Data was collected for three consecutive steps for each pair of current and speed values.

A block diagram of the simulation is shown in Figure 3.6. The torque gain, time constant, and backlash blocks are described in detail below.

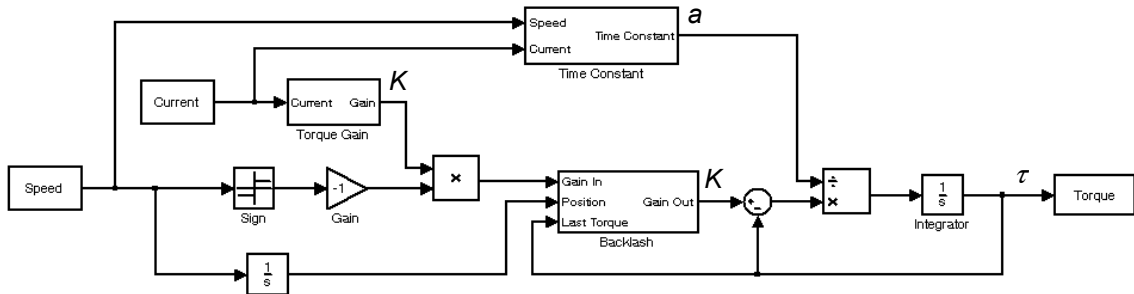


Figure 3.6. Block Diagram of First Order Brake Model

3.4.1 Torque Gain

The torque gain was determined as the mean value of the steady state torque for each set of three current steps. Figure 3.7 shows a surface plot relating steady state torque to current and speed. As expected, speed has no detectable influence on torque output. On the other hand, there appears to be a quadratic relationship between current and torque in the range .2 to 1.0 A. Therefore a piecewise function of the following form is proposed for the torque gain:

$$K = \begin{cases} k_1 I + k_2, & I < .2 \text{ A} \\ k_3 I^2 + k_4 I + k_5, & I \geq .2 \text{ A} \end{cases} \quad (3.3)$$

The torque gain coefficients, k_i , were determined by a least squares fit of average steady state torque values at each current. The resulting coefficients for each brake, along with R^2 values, are shown in Table 3.2. The torque coefficient k_2 is equivalent to the off-state torque, which is the minimum torque that each brake will output when in motion.

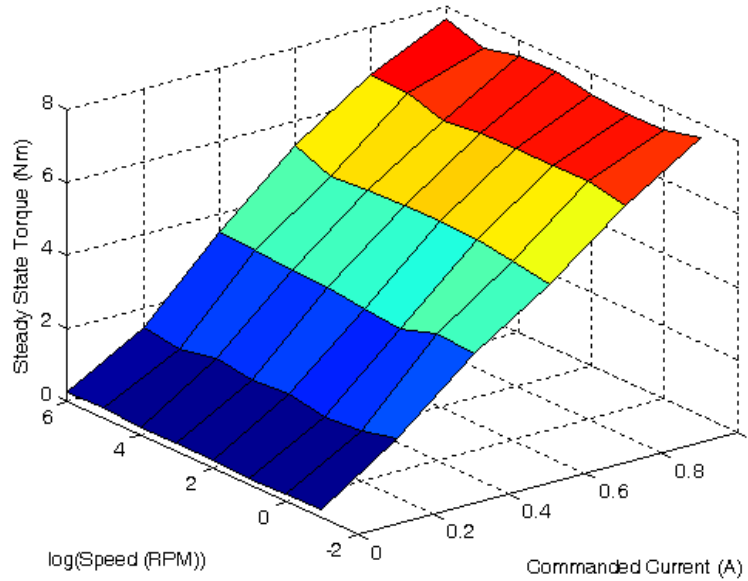


Figure 3.7. Torque Gain vs. Current and Speed

Table 3.2. Torque Gain Curve Fit Data

Brake	k_1 (Nm/A)	k_2 (Nm)	k_3 (Nm/A ²)	k_4 (Nm/A)	k_5 (Nm)	R^2
A	6.09	0.22	-3.68	12.05	-0.84	0.9977
E	4.32	0.21	-2.72	9.37	-0.71	0.9901
B	4.72	0.24	-2.14	8.76	-0.49	0.9880
C	4.74	0.27	-2.21	8.48	-0.39	0.9802

The torque gain fit equation is shown alongside the average torque data in Figure 3.8. It is evident from this figure that there is some variation in torque that is not dependent on

current or speed. In order to quantify this variation, the standard deviation of each steady state torque measurement was computed for each current. The results are summarized in Figure 3.9. At each point the standard deviation is computed from the average steady state torque for 24 trials. The standard deviation in steady state torque measurements generally increases with increasing current, with a maximum of about .4 Nm. The variance in torque output can be attributed to a number of factors including fluid temperature [10] and particle settling [13].

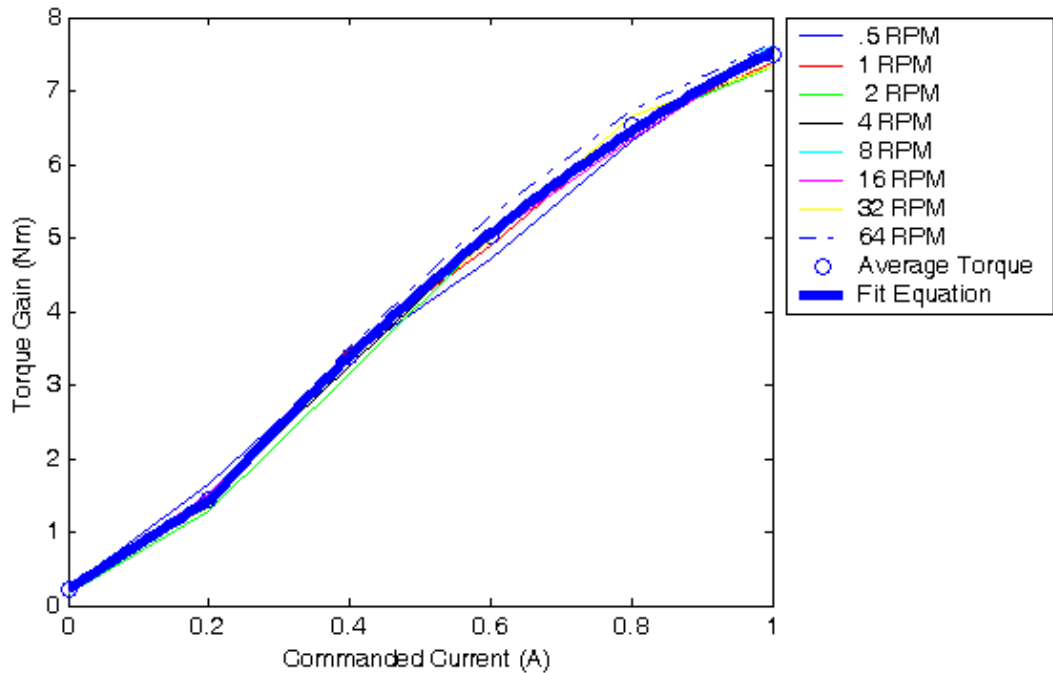


Figure 3.8. Torque Gain Fit Applied to Data

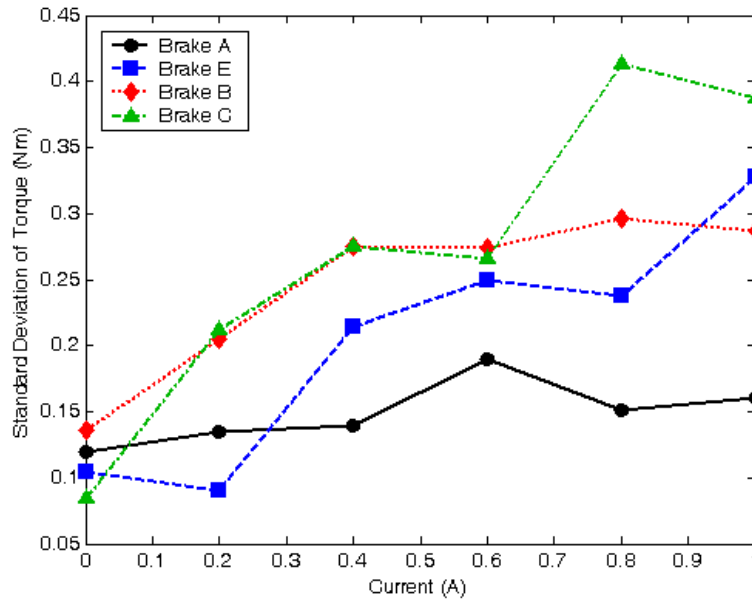


Figure 3.9. Standard Deviation of Torque vs. Current

3.4.2 Time Constant

The time constant was determined from the inverse slope of the following equation using the transient region of the step response data:

$$\frac{t}{a} = -\ln\left(\frac{\tau - \tau_1}{\tau_2 - \tau_1}\right). \quad (3.4)$$

This equation is derived from the standard first order formulation, with τ_1 as the initial torque, τ_2 as the final torque, and t as time. Again the average of three identical current steps was used to compute each value. The resulting data for rising and falling time constants are shown as surface plots vs. current and speed in Figures 3.10 and 3.11, respectively. The falling time constant is generally smaller because the amplifier can switch to negative voltage to drive the current down faster.

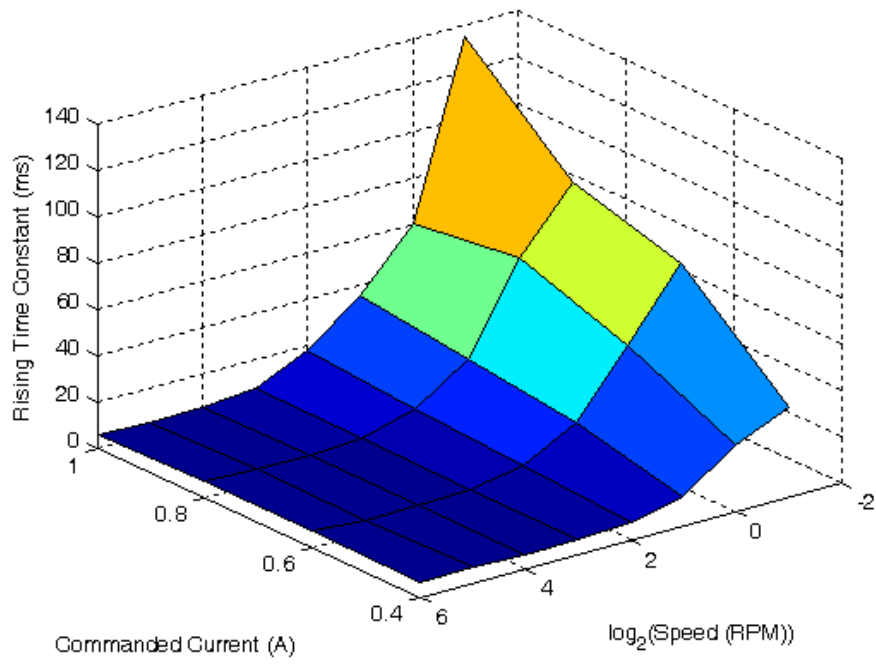


Figure 3.10. Rising Time Constant vs. Current and Speed

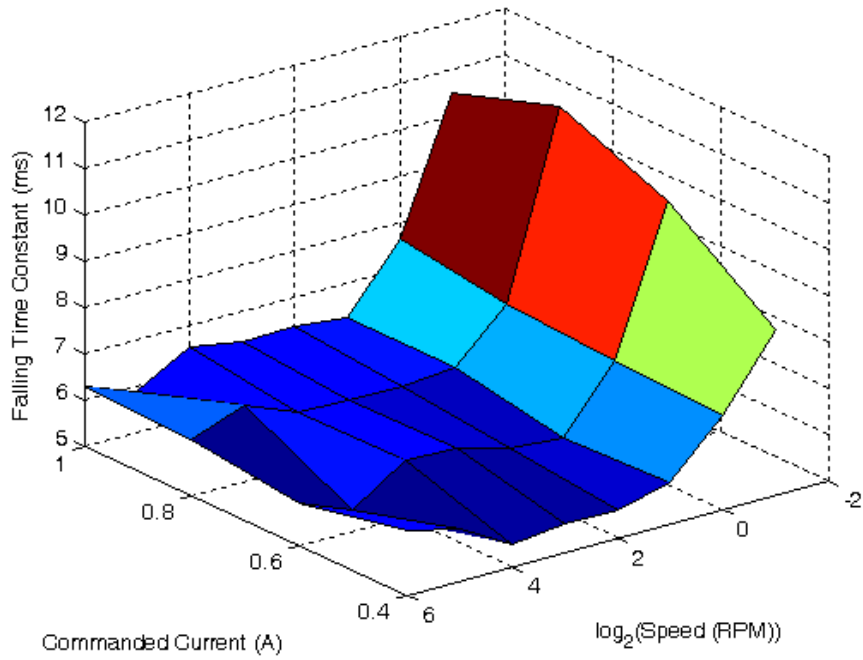


Figure 3.11. Falling Time Constant vs. Current and Speed

Examination of Figures 3.10 and 3.11 reveals that the time constant remains relatively constant above a certain speed. Below this threshold the time constant increases with decreasing speed. This effect can likely be attributed to a certain amount of agitation that must take place in order to initiate the formation and breakdown of particle chains within the fluid in the rising and falling cases, respectively. The time constant appears to be a linear function of current and a quadratic function of $\log_2(\omega)$ in the low-speed region. Therefore the following equations are proposed to model the rising and falling time constants:

$$a_{\text{rising}} = \begin{cases} a_{r,\text{avg}}, & \omega \geq 4 \text{ rpm} \\ a_{r1}I + a_{r2}\omega_L + a_{r3}I\omega_L + a_{r4}\omega_L^2 + a_{r5}I\omega_L^2 + a_{r6}, & \omega < 4 \text{ rpm} \end{cases} \quad (3.5)$$

$$a_{\text{falling}} = \begin{cases} a_{f,\text{avg}}, & \omega \geq 2 \text{ rpm} \\ a_{f1}I + a_{f2}\omega_L + a_{f3}I\omega_L + a_{f4}\omega_L^2 + a_{f5}I\omega_L^2 + a_{f6}, & \omega < 2 \text{ rpm} \end{cases}, \quad (3.6)$$

where

$$\omega_L = \log_2 \omega. \quad (3.7)$$

The time constant coefficients, a_{ri} and a_{fi} , are determined by a least squares fit of the relevant data. The resulting values are shown in Table 3.3 along with the R^2 values (units are omitted to save space). The surfaces generated by these equations are shown in Figures 3.12 and 3.13. In the simulation, the time constant is extrapolated using Equations 3.5 and 3.6 if the speed is outside the tested range.

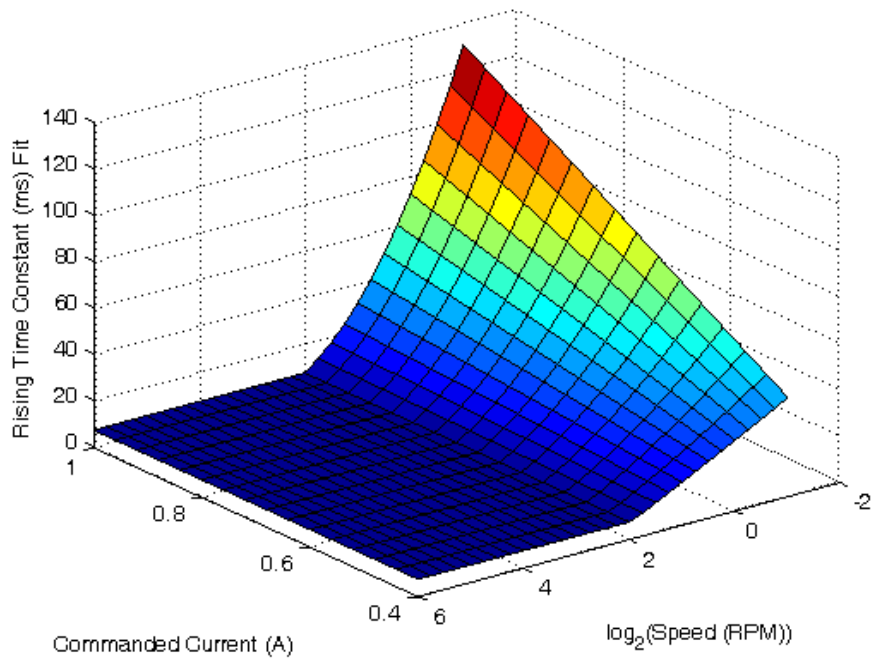


Figure 3.12. Rising Time Constant Surface Fit

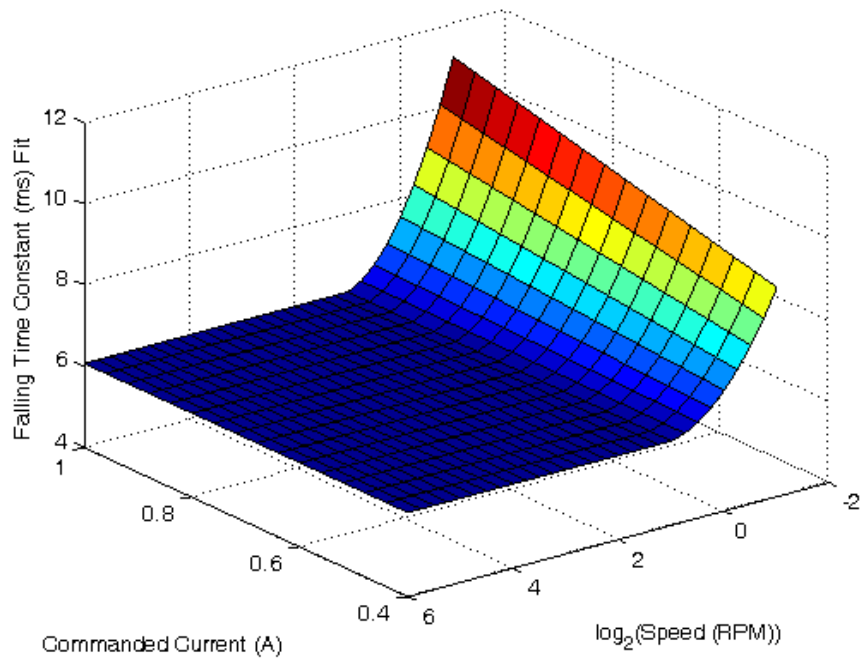


Figure 3.13. Falling Time Constant Surface Fit

Table 3.3. Time Constant Surface Fit Data

	Brake	a_{avg}	a_1	a_2	a_3	a_4	a_5	a_6	R^2
Rising	A	0.0075	0.0697	0.0129	-0.0623	-0.0055	0.0141	0.0025	0.9782
	E	0.0070	0.0317	0.0063	-0.0344	-0.0017	0.0094	0.0012	0.9839
	B	0.0075	0.0260	0.0046	-0.0278	-0.0019	0.0076	0.0055	0.9807
	C	0.0064	0.0451	-0.0088	-0.0185	0.0055	-0.0020	0.0019	0.9698
Falling	A	0.0061	0.0010	-0.0009	-0.0017	0.0004	0.0007	0.0066	0.9388
	E	0.0054	0.0017	-0.0002	-0.0017	0.0006	0.0000	0.0050	0.8473
	B	0.0057	0.0018	-0.0007	-0.0015	0.0011	-0.0003	0.0052	0.8548
	C	0.0052	0.0045	-0.0003	-0.0017	0.0032	-0.0028	0.0023	0.9267

3.4.3 Backlash Modeling

As shown in Figure 3.5, the backlash has a significant effect on torque output and must be incorporated into the model. The effect of backlash can be demonstrated by the linear mechanical diagram shown in Figure 3.14. F_b and F_0 are Coulomb friction elements representing breakaway force and off-state force, respectively. The backlash boundaries are represented by x_1 and x_2 . When x lies within these boundaries the breakaway torque is F_0 ; outside the boundaries the breakaway torque is F_b .

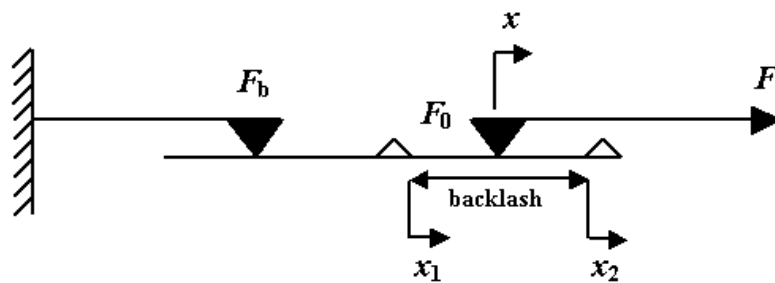


Figure 3.14. Backlash Schematic

The same analysis can be applied to the brakes by converting force (F) to torque (τ) and linear position (x) to rotational position (θ). The following method is then used to implement backlash in the simulation. When torque crosses zero, indicating a change in the sign of speed, the backlash boundaries are held constant and the torque gain is set to the product of off-state torque and the negative sign of speed. If the shaft position crosses either boundary, torque gain is set to its normal value and θ_1 and θ_2 are set to change at the same rate as θ . Normal operation continues until a change another change in the sign of torque is detected.

3.5 Model Verification

The validity of the brake model was evaluated by comparing the model output to physical data for a variety of current and speed inputs. Figure 3.15 compares the brake model to the current step data described in Section 3.3.1. It is not surprising that the model closely matches the data because this data was the basis by which the model was derived. Figure 3.16 shows a comparison of the model output to one of the sinusoidal motion experiments. Here the steady state torque is underestimated by just over 1 Nm. This is within a 95% confidence interval of the expected torque output based upon the standard deviation of torque shown in Figure 3.9. However, it was observed that torque output was generally higher than the expected value after a change in the sign of speed. The shift of the torque vs. position curve in Figure 3.16 can be attributed to the inability of the motor to maintain the desired speed, and not error in the model. Figure 3.17 indicates that the brakes exhibit hysteresis in the torque vs. current relationship. This phenomenon

was not considered in the brake modeling. However, as shown in the figure, the model does capture the general effect.

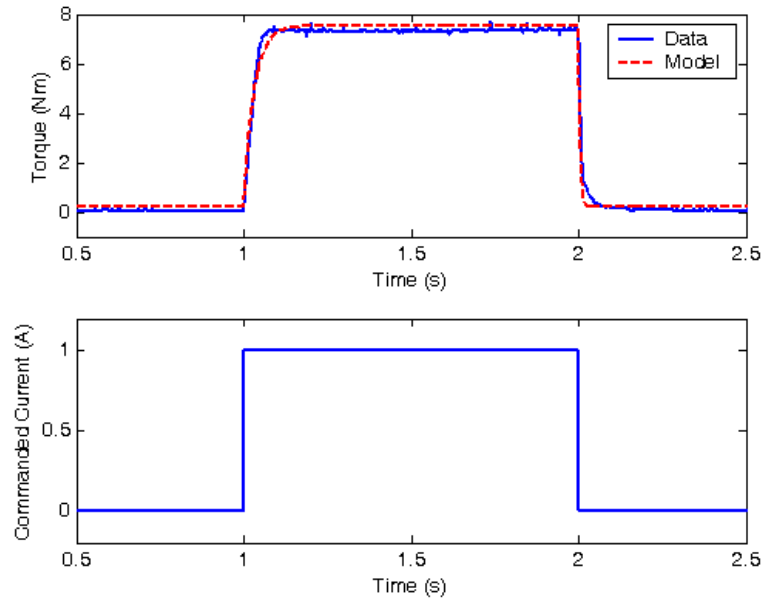


Figure 3.15. Comparison of Model to Current Step Response

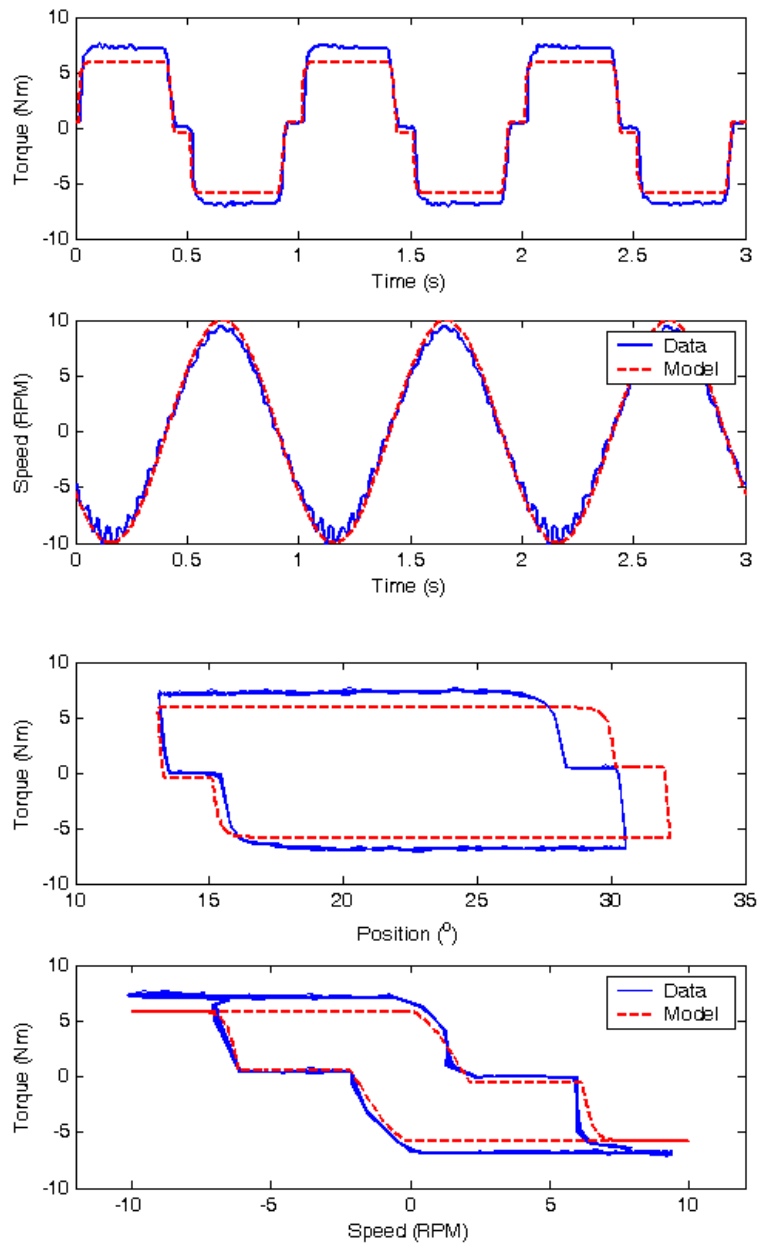


Figure 3.16. Comparison of Model to Sinusoidal Data

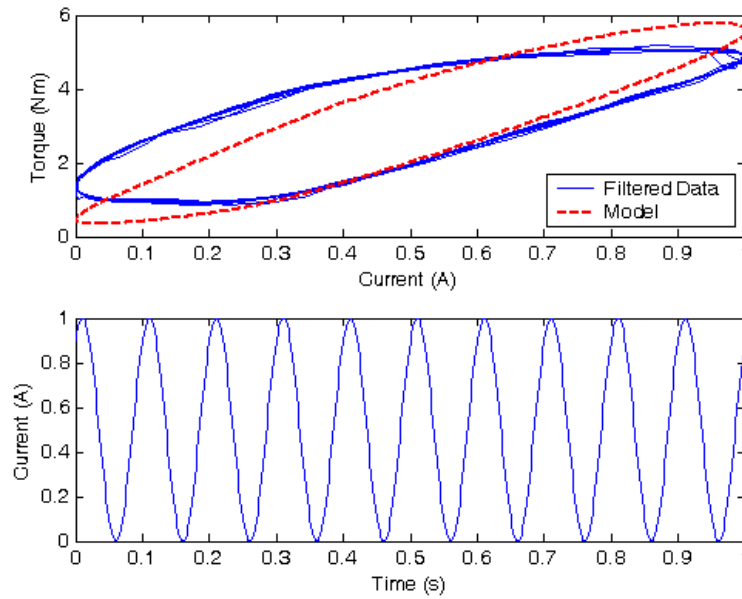


Figure 3.17. Comparison of Model to Sinusoidal Current Data

3.6 SDOF Control Experiments

It is desired that the robot be able to operate without torque feedback control. Therefore two experiments were designed to test the ability to accurately control braking torque. As shown in Figure 3.18, the testbed was modified from the previous configuration by attaching a lever in place of the electric motor. This allowed tests to be performed by a human operator in order to more closely mimic the operating conditions of the robot.

The two control experiments consisted of a virtual spring and a virtual wall. In the virtual spring experiment, the desired torque increases linearly with position as the spring is compressed. However, the brake cannot simulate spring expansion because of its passive limitations. Therefore the brake is set to zero current when torque is detected in the direction moving out of the spring. A spring constant of $.05 \text{ Nm/}^\circ$ was implemented

on the apparatus. A virtual wall is simply a virtual spring with a very high spring constant. Here a spring constant of 500 Nm/° was used.

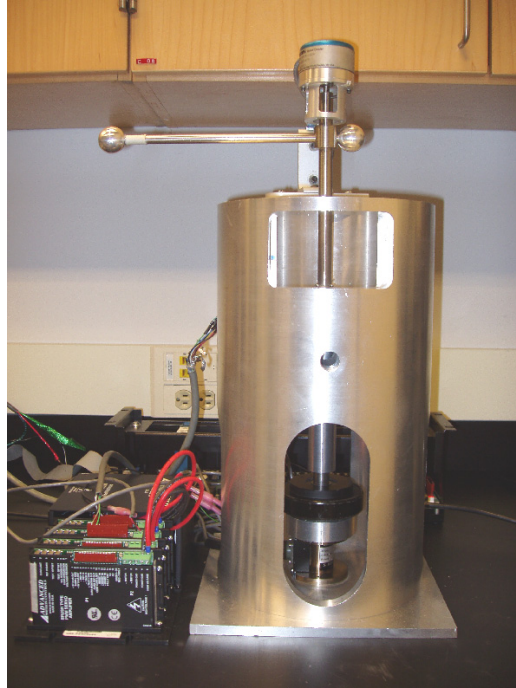


Figure 3.18. Control Experiment Apparatus

Two controllers were tested in the virtual spring and wall experiments. Open loop control, as shown in Figure 3.19, determines the desired torque based on position using a look-up table. The desired torque is used to compute the desired brake current that will be controlled by the amplifier using the current gain block. This block simply performs the inverse of the torque gain function (Equation 3.3). Also tested was a closed loop controller, shown in Figure 3.20, that features a proportional feedback term in addition to the look-up table and inverse torque gain blocks.

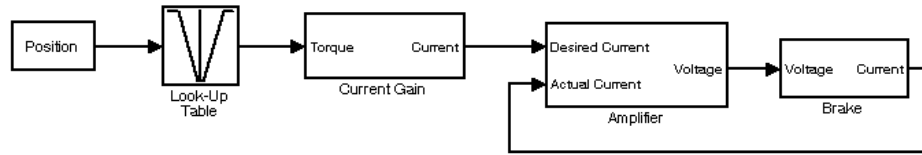


Figure 3.19. Open Loop Controller

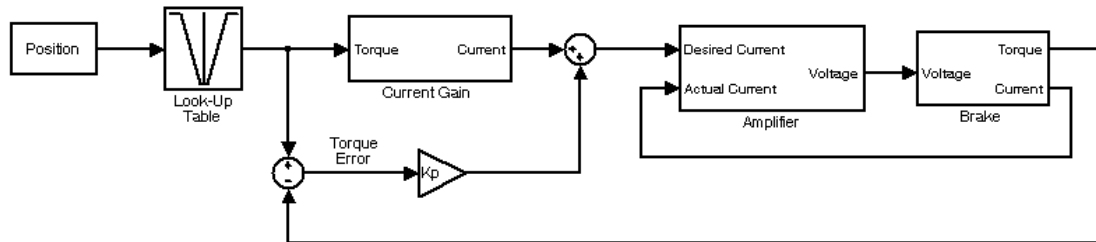


Figure 3.20. Closed Loop Controller

For each experiment the user tried to maintained a constant speed of 10 rpm. The results of the virtual spring and virtual wall are shown in Figures 3.21 and 3.22, respectively. For the closed loop controller, the highest gain was chosen such that no detectable vibration was induced. In the virtual wall case, it should be noted that feedback control reduces error in the steady state region, yet has no effect on response time. In general, the error resulting from open loop control is in the acceptable range and likely would not be detectable by a human. However, if very precise braking torque is needed, the robot would have to be outfitted with torque sensors.

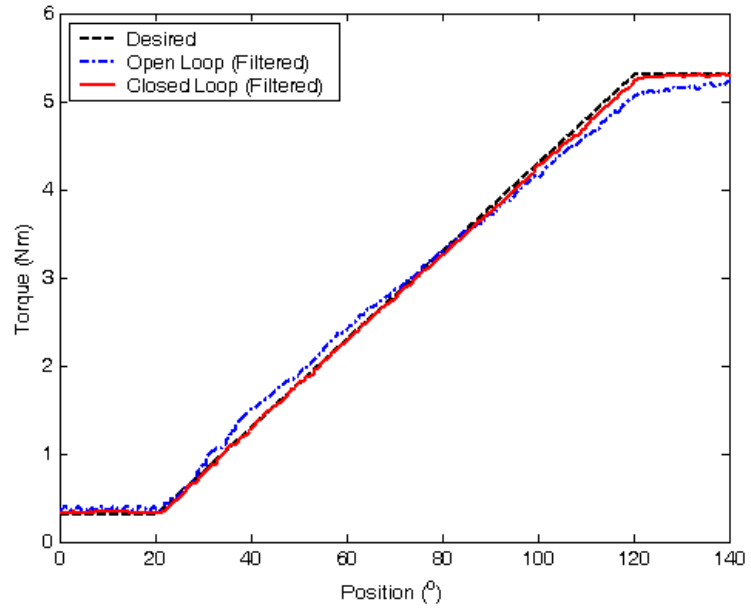


Figure 3.21. Virtual Spring Control Experiment

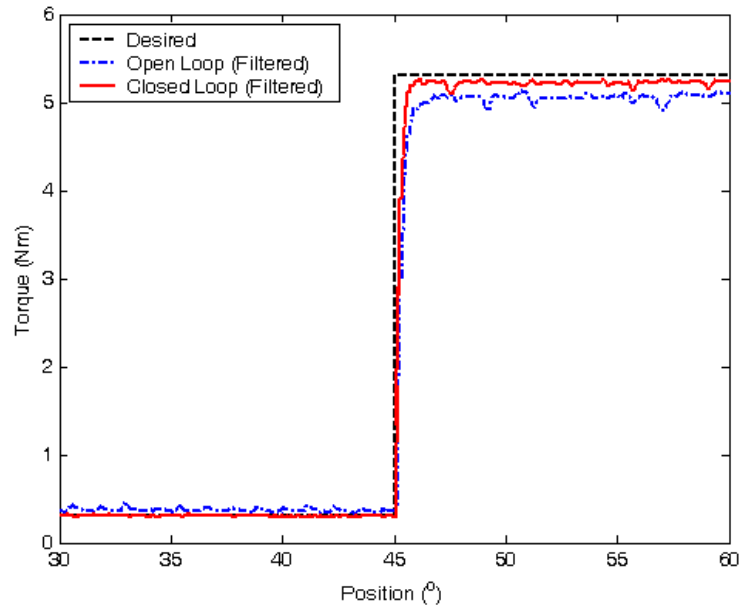


Figure 3.22. Virtual Wall Control Experiment

CHAPTER 4

ROBOT DESIGN

This chapter discusses the selection of a robot design from several design concepts. It then outlines the method by which the robot geometry was chosen. Finally, the detailed mechanical design is presented and concerns regarding singularities are addressed.

4.1 Selection Criteria

The goals of the robot design are to maintain the functionality of PTER while improving upon some of its limitations. The following criteria were considered in the development of design concepts and selection of the final design:

- Small, tabletop size
- Simple, rigid mechanical design
- Ease of use
- Low inertia
- Low friction
- 2-DOF planar motion
- Unconstrained free motion
- Large, evenly-shaped workspace
- Utilization of coupling actuators (more actuators than degrees of freedom)
- Actuated by MR fluid brakes (MRB-2107-3)

- Capability of converting to 3-DOF system

4.2 Design Concepts

Four concepts are presented that were considered as designs for a new dissipative passive haptic display.

4.2.1 X-Y Table

The X-Y table shown in Figure 4.1 uses four brakes that can constrain the user to one of four local SDOF paths when locked. The design is a simplification of the X-Y table presented by Charles [2]. Brakes 1 and 2 connect to the crossbars by means of a belt and pulley system that brake in the y- and x-direction, respectively. Brake 3 provides direct coupling of the x- and y-directions using a set of bevel gears. The brake shaft attaches to one of the x-direction pulleys. One bevel gear attaches to the brake shaft; a second connects to one of the y-direction pulleys. In a similar fashion, brake 4 provides inverse coupling of the x- and y-directions when locked.

This design is advantageous because the tip motion is less affected by backlash than in the designs discussed in the following sections. Ultimately, this design was not chosen because it is awkward to use. The user must lean over the device and risks getting their hair or an article of clothing caught in the moving parts. Also, it has no ability to be converted into a 3-DOF system in the future. Furthermore, the designs that follow are much simpler because they feature fewer moving parts.

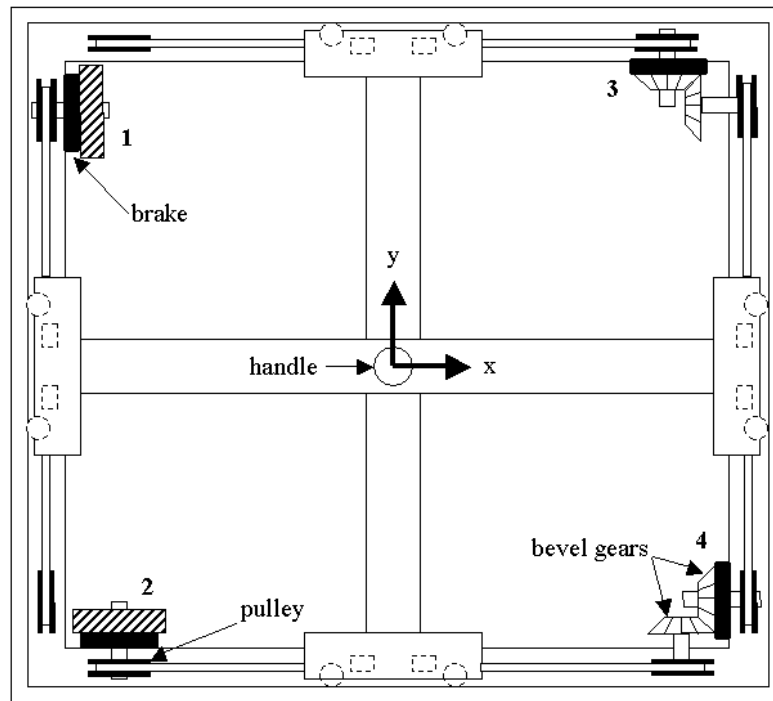


Figure 4.1. X-Y Table Design Concept

4.2.2 Scaled PTER

PTER, shown in Figure 4.2, was discussed in detail in Chapters 1 and 2. This design concept calls for a scaled version of PTER to be constructed with MR fluid brakes used in place of the friction clutches. At one time it was considered to mount the MR fluid brakes directly on PTER. This was ruled out because the force transmitted to the tip of the robot in its current configuration would be too small.

A scaled version of PTER is advantageous because it allows for direct comparison of the performance of the MR fluid brakes to that of the existing clutches. However, this option was not chosen for the following reasons. First, the column of actuators and gearing at the central axis would require the device to be nearly 1 m tall. Also, there is a desire to evaluate the performance of new robot designs in addition to the new actuators.

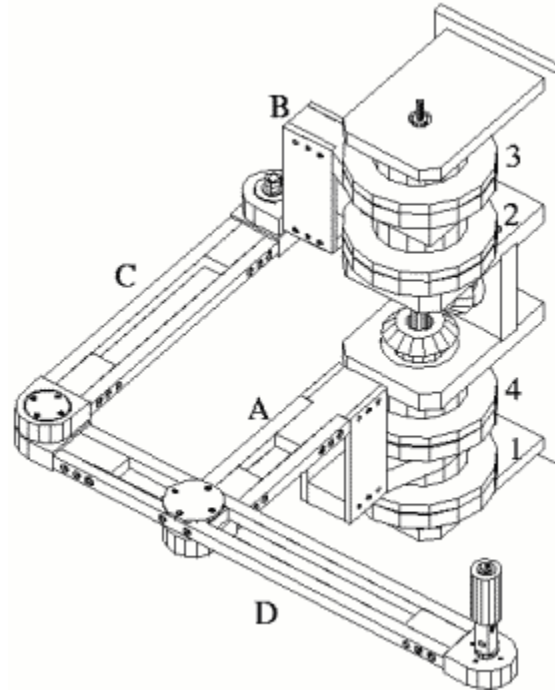


Figure 4.2. PTER (Passive Trajectory Enhancing Robot)

4.2.3 Three-Brake Five-Bar Linkage

The five-bar linkage shown in Figure 4.3 uses three MR fluid brakes that are capable of constraining tip motion to one of three local SDOF paths when locked. It features equal length arms arranged in the shape of a rhombus. There are two MR fluid brakes at the base. One acts to lock link AE and the other acts to lock link BC. A third brake, placed at joint E, acts as a coupling actuator that acts to lock the frame such that the tip (point D) rotates about the base.

Placing an actuator on a moving joint makes link coupling possible without adding significantly to the size or complexity of the device. The particular configuration presented here extends outward from the base, making it very simple to use. Like PTER, the kinematics are relatively simple. On the downside, placing an actuator on a moving joint increases the inertia felt at the handle. However, due to the small mass of the brake,

its inertial contribution should not be very noticeable. It was decided to implement this design in conjunction with the 4-brake five-bar linkage, which is presented in the next section.

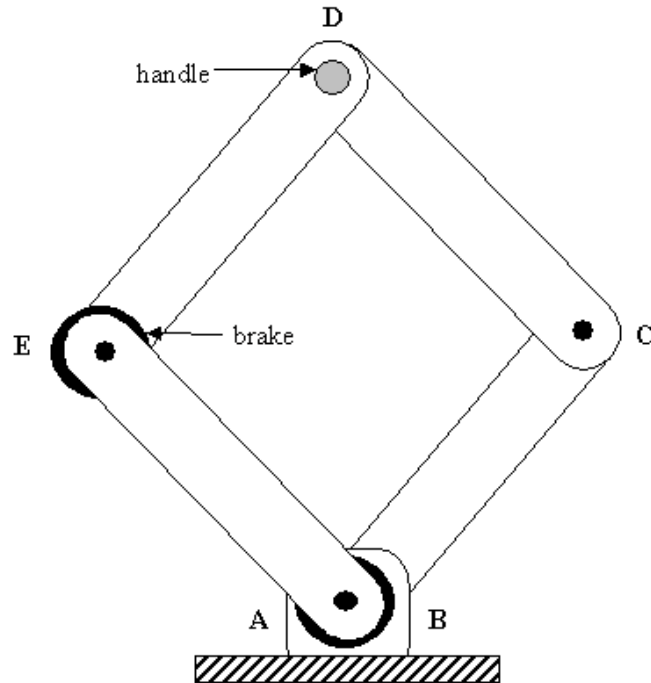


Figure 4.3. 3-Brake Five-Bar Linkage

4.2.4 Four-Brake Five-Bar Linkage

PTER is capable of constraining tip motion to any one of four local SDOF paths by locking a clutch. The 3-brake five-bar linkage is limited by design to only three local SDOF paths. Adding another brake to joint C or D in this design is redundant. However, if the base joints, A and B, are separated, a fourth local SDOF path can be realized by placing an actuator on joint C. This concept is dubbed the 4-brake five-bar linkage and is shown in Figure 4.4.

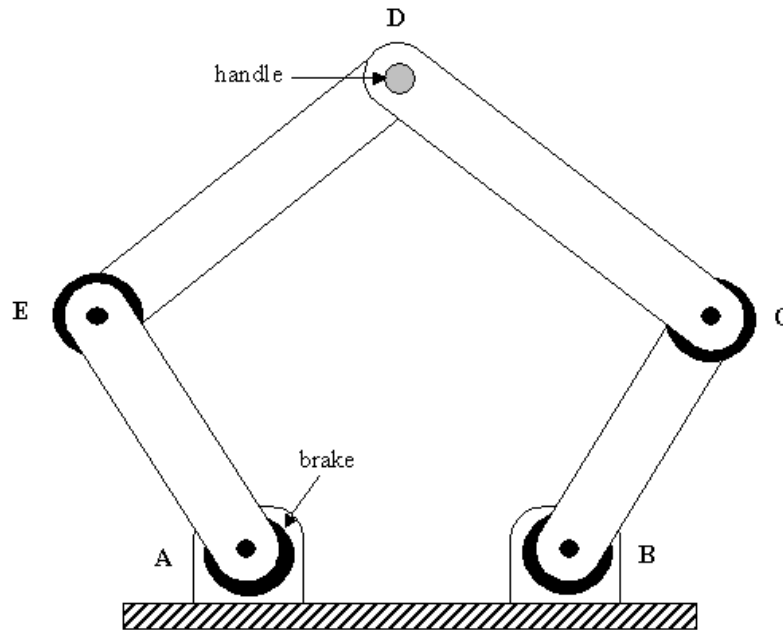


Figure 4.4. 4-Brake Five-Bar Linkage

Due to the similar construction of the 3-brake and 4-brake configurations, the device was designed such that both forms could be evaluated. This will allow for direction comparison between the two designs and evaluation of the benefits of a fourth actuator.

4.3 Selection of Robot Geometry

The geometry of the robot is shown in Figure 4.5. The same figure is used for both forms, with L_{AB} set to zero for the 3-brake case. The relative lengths of the 3-brake form have already been determined on the basis of simplifying the kinematics and more closely resembling the geometry of PTER. On the other hand, the complexity of the kinematics of the 4-brake form is not affected by relative arm lengths. Therefore the arm lengths must be chosen such that performance is maximized.

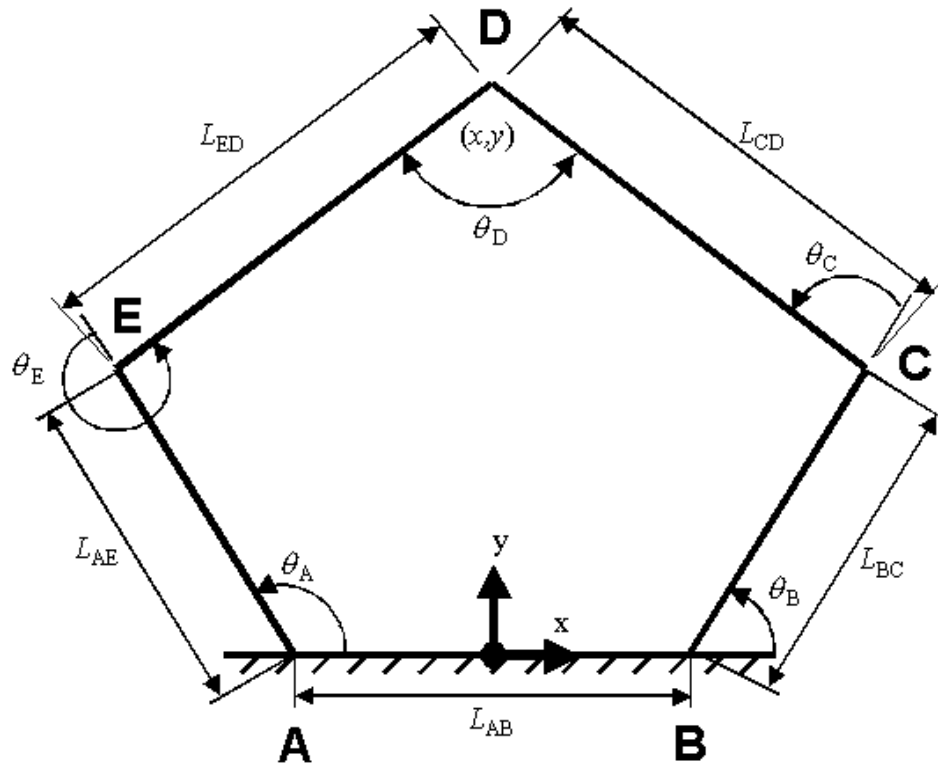


Figure 4.5. Robot Geometry

A 2-DOF device with two active actuators can generally apply tip force in any direction in the x - y plane. A passive device is limited in that it may only apply force in a direction that opposes velocity. In order to reduce the effects of this limitation, it is desirable to have additional actuators that can apply force in additional directions and that the force vectors are as evenly spread apart as possible. This is illustrated by the example shown in Figures 4.6a and 4.6b.

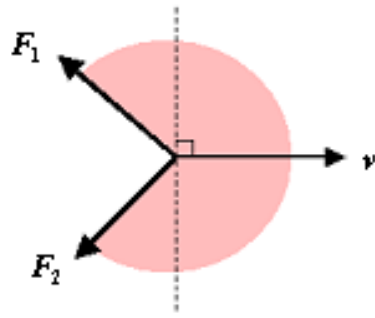


Figure 4.6a. Illustration of Unachievable Forces with Two Brakes

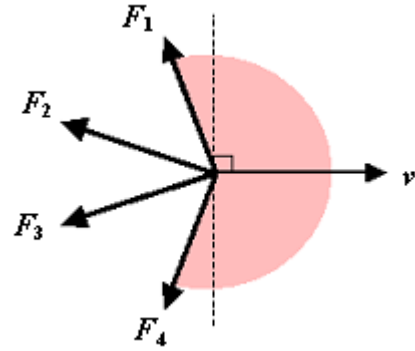


Figure 4.6b. Illustration of Unachievable Forces with Four Brakes

In Figures 4.6a and 4.6b, the velocity is given by v . All valid forces point to the left of the dashed line, which lies perpendicular to velocity. In Figure 4.6a, two actuators are used that can generate two tip forces, F_1 and F_2 . The shaded region represents the directions of forces that cannot be achieved from a combination of F_1 and F_2 . Figure 4.6b presents the same illustration where four actuators are used that can generate four force vectors. If these additional vectors are spaced properly, the region of unachievable forces is reduced.

A similar argument can be made by looking at local SDOF paths. The set of local SDOF paths at each point lie perpendicular to the available force vectors. If the controller operates by locking the tip into a local SDOF path, it is desirable to have those path directions spread apart as evenly as possible. The maximum angle between adjacent local SDOF paths was chosen to evaluate how evenly spaced the directions of local SDOF paths (or force vectors) are in the workspace. This measure was selected because it identifies the worst-case scenario in availability of local SDOF path directions. In fact, invalid solutions to the controllers presented in Chapter 6 exist when this angle exceeds

90°. Therefore it is desirable to minimize this angle. In the case of the four-brake robot, the maximum angle can vary between 45 and 180°.

An optimization was carried out in order to select the final dimensions. The following were goals of the optimization:

- Maximize workspace area
- Have a well-shaped workspace area
- Maximize area of well-spaced local SDOF paths

The following procedure was used to select the geometry. For symmetry, L_{BC} and L_{AE} are set equal and L_{CD} and L_{ED} are set equal. L_{ED} is set to a dimensionless value of 1. The lengths L_{AE} and L_{AB} were selected as percentages of L_{ED} . Lengths ranging from 0.1 to 2.0 were investigated for L_{AE} , while the range of 0 to 2.0 was used for L_{AB} . For each set of arm lengths, the entire workspace of the robot was discretely traversed in Cartesian coordinates. At each point, the angle of each local SDOF path was computed and the maximum angle was found. This operation is shown in Figure 4.7, with L_{ED} and L_{AB} set to 0.9. When the step size is reduced to a very small value, this information can be shown as a contour plot of the maximum angle between SDOF lines. Contour plots for each set of arm lengths were plotted and the set that best accomplishes the optimization goals was selected by inspection.

It was found that arm lengths L_{ED} and L_{AB} of about 90% yield the best workspace properties. A length of 30.5 cm (12.0 in) was selected for length L_{ED} . This length virtually eliminates the perception of joint friction due to off-state torque and results in a manageable workspace area. The remaining arm lengths, shown in Table 4.1, were changed slightly to simplify the design process. The contour plots that were used in the

optimization process are shown in Figures 4.8 and 4.9 for the final dimensions. Additionally, Figures 4.10 and 4.11 show a map of the SDOF paths for both configurations.

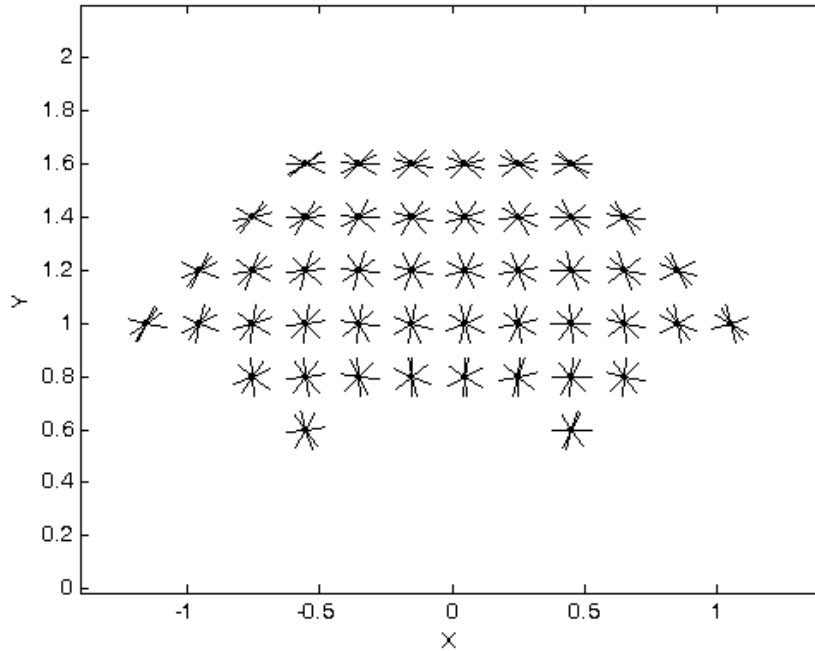


Figure 4.7. Local SDOF Paths for $L_{ED} = L_{AB} = .9$

Table 4.1. Robot Dimensions

Dimension	3-Brake	4-Brake
L_{AE} (cm)	30.5	26.4
L_{BC} (cm)	30.5	26.4
L_{ED} (cm)	30.5	30.5
L_{CD} (cm)	30.5	30.5
L_{AB} (cm)	0	26.7

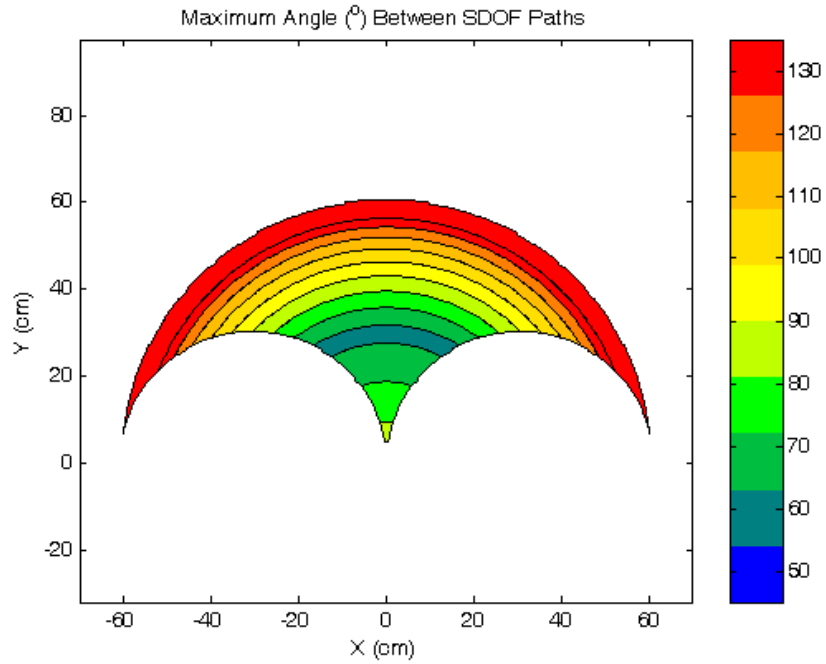


Figure 4.8. Contour Plot of Maximum Angle Between Local SDOF Paths for 3-Brake Configuration

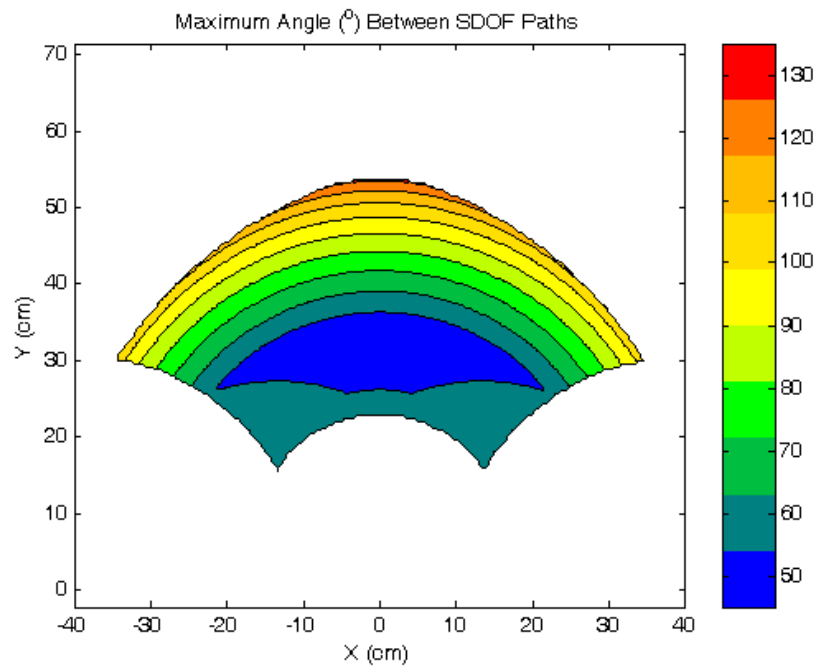


Figure 4.9. Contour Plot of Maximum Angle Between Local SDOF Paths for 4-Brake Configuration

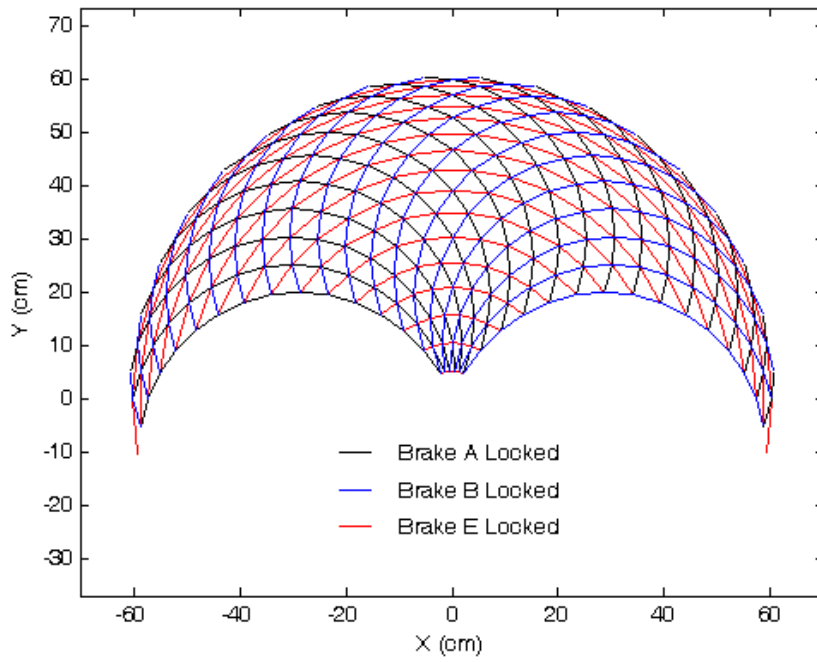


Figure 4.10. SDOF Paths for 3-Brake Configuration

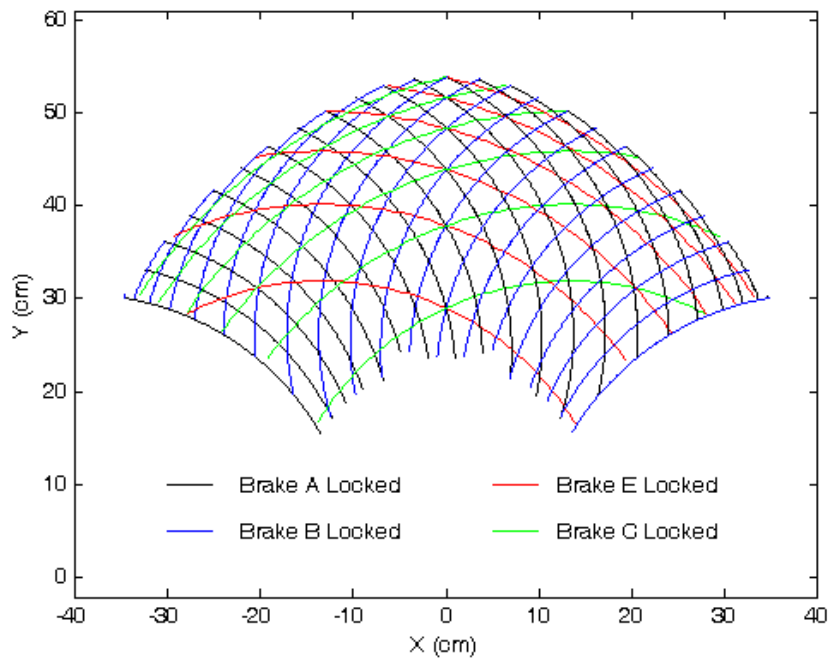


Figure 4.11. SDOF Paths for 4-Brake Configuration

4.4 Mechanical Design

The final designs for the three-brake and four-brake configurations are shown as CAD drawings in Figures 4.12 and 4.13, respectively. Photographs are shown in Figures 4.14 and 4.15. The base is constructed out of 2.54 cm (1.00 in) aluminum plate. The arms are made from 2.54 cm (1.00 in) aluminum bar. Arms AE and BC are designed such that the brakes at joints E and C can mount in two locations. This allows the same arms to be used for both configurations. Each MR fluid brake contains 2 internal bearings that were used for joint alignment. The arms were coupled to the brake shafts by means of a steel collar and gib-head key. The joints that without brakes are formed by passing a shaft through an angular contact ball bearing. Also shown in Figures 4.12 and 4.13 are the force sensor handle located at the tip and optical encoders located at the base joints.

The overall mechanical design of this robot is much simpler than the other design concepts that were considered. By placing actuators on moving joints, the need for bevel gear systems is eliminated. Additionally, each arm is constructed out of aluminum as a simple one-piece design, which ensures rigidity of the device as well as low inertia. The design also allows for additional reductions in inertia to be made by removing material from the center section of each arm.

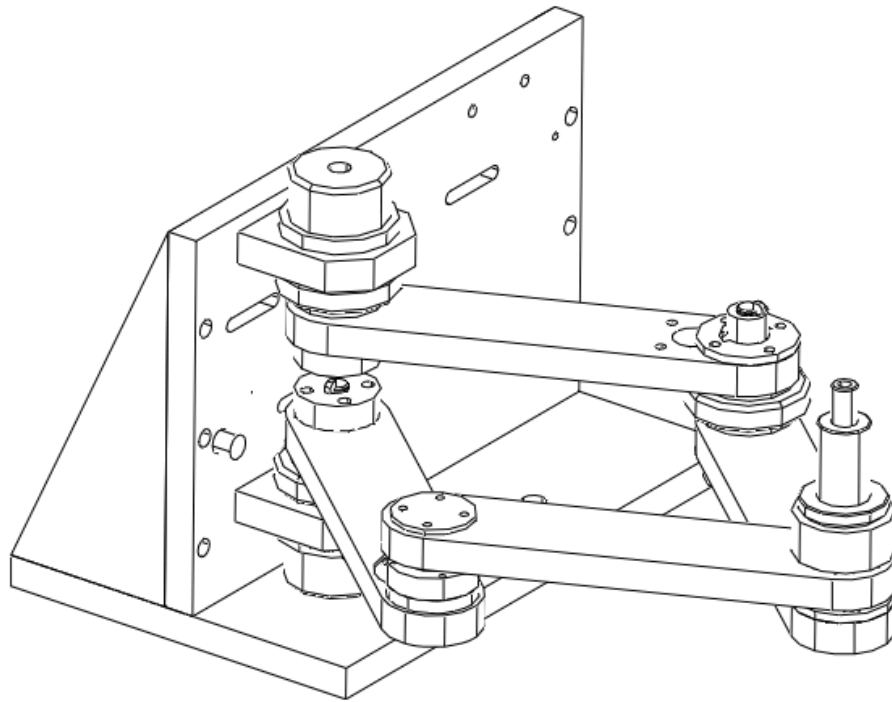


Figure 4.12. 3-Brake Assembly Drawing

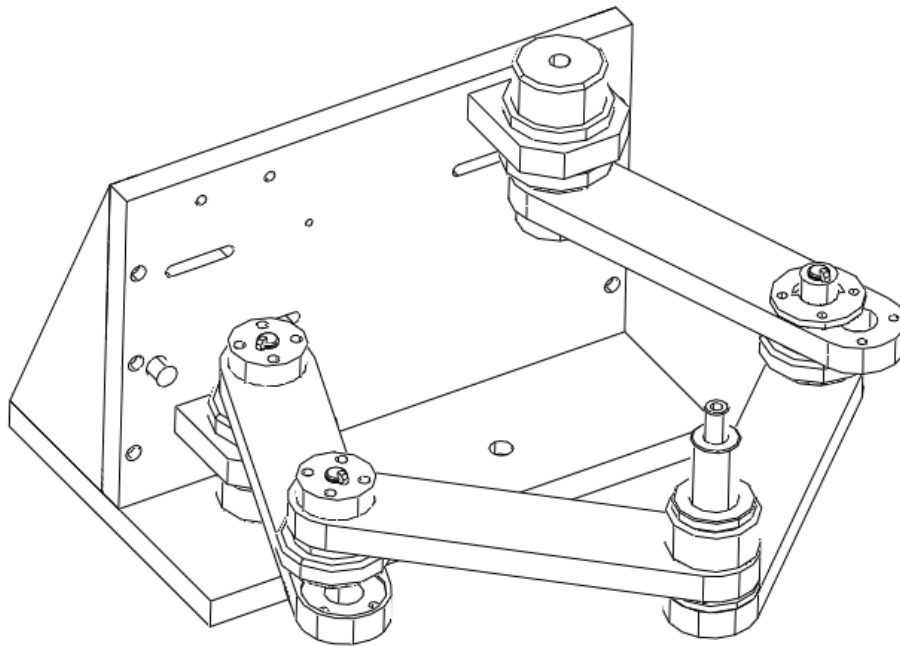


Figure 4.13. 4-Brake Assembly Drawing

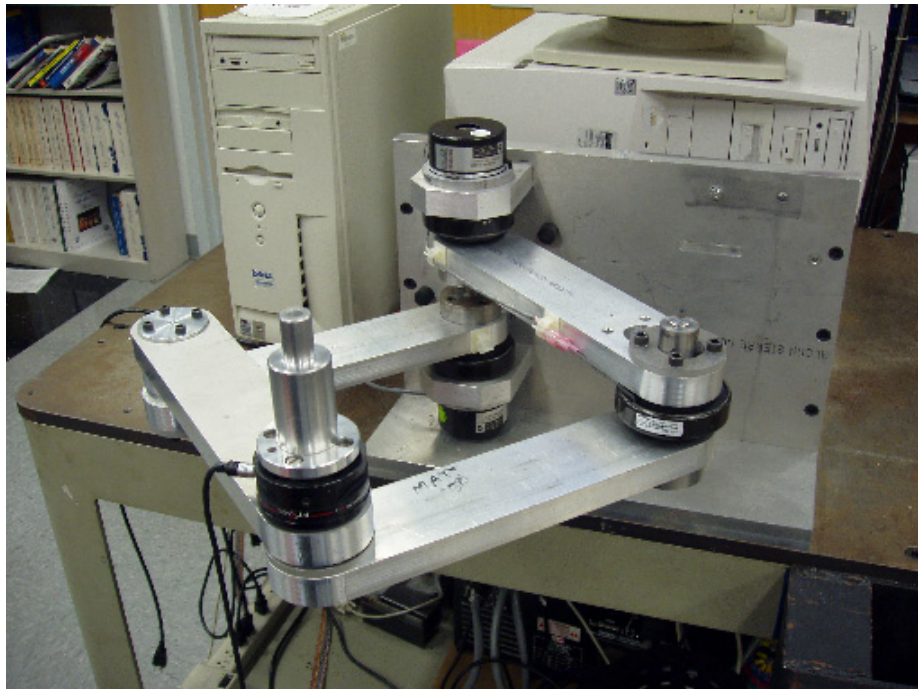


Figure 4.14. Photograph of 3-Brake Robot



Figure 4.15. Photograph of 4-Brake Robot

4.5 Singularity Analysis and Joint Constraints

It is necessary to prevent the robot from reaching a singular position such that conditions do not arise where there can be multiple solutions to the forward or inverse kinematics. Based on the fact that this is geometrical consideration and tip position will be computed using only the base joint angles, θ_A and θ_B , a 2×2 Jacobian is used. While useful for this exercise, a Jacobian of this form is not a true Jacobian for the system because it cannot relate joint torques to tip forces since there are more than two actuators.

The Jacobian, \mathbf{J} , for a parallel manipulator relates the tip velocity, $\dot{\mathbf{x}}$, to the joint velocities, $\dot{\boldsymbol{\theta}}$, by the following equation:

$$\dot{\boldsymbol{\theta}} = \mathbf{J}\dot{\mathbf{x}}. \quad (4.1)$$

In the velocity vector-loop formulation presented by Tsai [25], Equation 4.1 can be expressed as follows:

$$\mathbf{J}_x \dot{\mathbf{x}} = \mathbf{J}_\theta \dot{\boldsymbol{\theta}}. \quad (4.2)$$

In this form, forward kinematic singularities exist when the determinant of \mathbf{J}_x is zero. Here a nonzero $\dot{\mathbf{x}}$ vector can result in a zero $\dot{\boldsymbol{\theta}}$ vector. Likewise, inverse kinematic singularities exist when the determinant of \mathbf{J}_θ is zero. In this case, a nonzero $\dot{\boldsymbol{\theta}}$ vector can result in a zero $\dot{\mathbf{x}}$ vector.

For both robot configurations, \mathbf{x} is comprised of the tip coordinates, x and y , and $\boldsymbol{\theta}$ is comprised of the base joint angles θ_A and θ_B , as shown below.

$$\mathbf{x} = \begin{bmatrix} x \\ y \end{bmatrix}$$

$$\boldsymbol{\theta} = \begin{bmatrix} \theta_A \\ \theta_B \end{bmatrix}$$

The following matrices are determined for \mathbf{J}_x and \mathbf{J}_θ based upon the robot geometry shown in Figure 4.5:

$$\mathbf{J}_x = \begin{bmatrix} ED_x & ED_y \\ CD_x & CD_y \end{bmatrix} \quad (4.3)$$

$$\mathbf{J}_\theta = \begin{bmatrix} \frac{ED_x}{AE_x ED_y - ED_x AE_y} & \frac{ED_y}{AE_x ED_y - ED_x AE_y} \\ \frac{CD_x}{BC_x CD_y - CD_x BC_y} & \frac{CD_y}{BC_x CD_y - CD_x BC_y} \end{bmatrix}, \quad (4.4)$$

where

$$\begin{aligned} AE_x &= L_{AE} \cos(\theta_A) \\ AE_y &= L_{AE} \sin(\theta_A) \\ BC_x &= L_{BC} \cos(\theta_B) \\ BC_y &= L_{BC} \sin(\theta_B) \\ CD_x &= L_{CD} \cos(\theta_B + \theta_C) \\ CD_y &= L_{CD} \sin(\theta_B + \theta_C) \\ ED_x &= L_{ED} \cos(\theta_A + \theta_E) \\ ED_y &= L_{ED} \sin(\theta_A + \theta_E) \end{aligned}$$

Solving Equations 4.3 and 4.4 for zero determinant results in three singularities. A direct kinematic singularity results when arms ED and CD are parallel. Inverse kinematic singularities exist when arms AE and ED are parallel and also when arms BC and CD are parallel. Using more than two actuators can reduce the number of robot singularities. Therefore these conditions represent a subset of the actual robot singularities.

Constraints were implemented in the hardware such that the above singularities could never be reached. A positioning ring was placed on the shafts of the brakes located at joints C and E. A small socket head cap screw was inserted into the side of the positioning in order to interface with the positioning plate, as shown in Figures 4.16a and

4.16b. The positioning ring and plate constrain the operating range of θ_C and θ_D to 10 to 170°, and the range of θ_E to 190 to 350°. Also, rubber bumpers are used to prevent θ_A from exceeding 180° and θ_B from dropping below 0°. The full range of each joint angle is shown in Table 4.2. The joint angle ranges in the 4-brake configuration are further limited by its geometry. Figure 4.17 shows the overlapping workspaces of both configurations and the joint angles that form the boundaries.

Table 4.2. Joint Angle Ranges

Angle (°)	3-Brake		4-Brake	
	Minimum	Maximum	Minimum	Maximum
θ_A	10	180	37	180
θ_B	0	170	0	143
θ_C	10	170	10	150
θ_D	10	170	51	170
θ_E	190	350	210	350

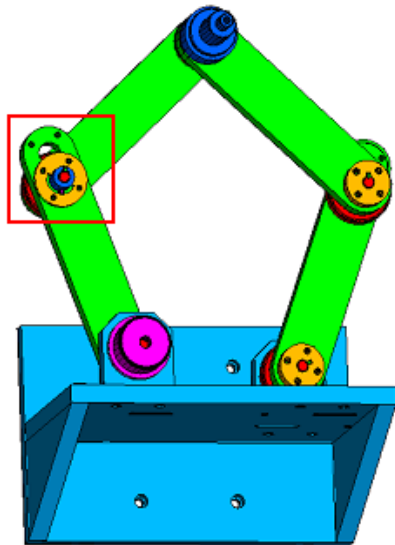


Figure 4.16a. Positioning Ring and Plate Assembly

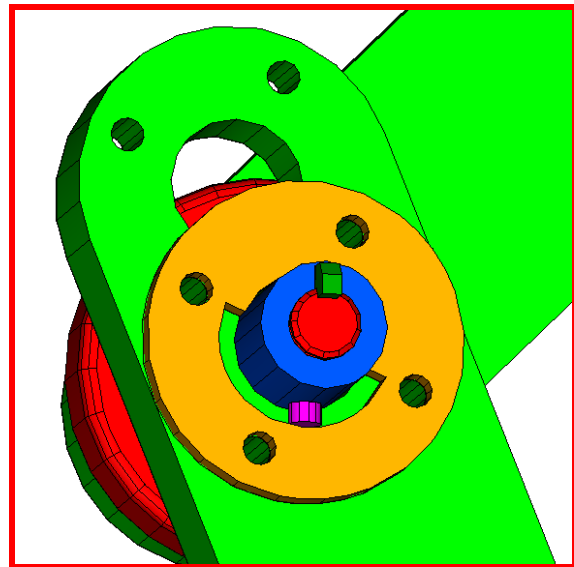


Figure 4.16b. Close-up of Positioning Ring and Plate Assembly

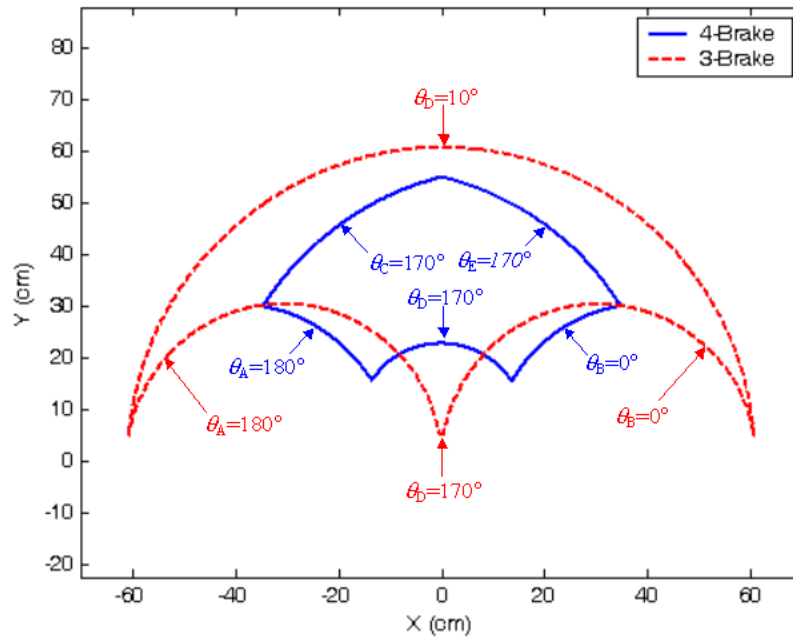


Figure 4.17. Workspace Boundaries

4.6 Equipment Selection

The MR fluid brakes are powered by four Advanced Motion Controls 12A8 PWM amplifiers that share a common PS4X300W power supply. The amplifiers are set to 1 A continuous output. The angular position of joints A and B are measured by Dynamics Research Corporation HS30C176B15N5000 quadrature optical encoders with 100,000 counts per revolution. Force at the handle is measured by a 6-axis Assurance Technologies FT 15/50 force and torque sensor and controller with analog output. Only the x- and y-channels of force are measured.

CHAPTER 5

ROBOT MODELING AND SIMULATION

This chapter presents the kinematics and equations of motion for the robot. The equations in this chapter are valid for any set of arm lengths except where indicated. A simulation procedure is also discussed and results from the robot simulation are compared to experimental data.

5.1 Kinematics

This section presents the forward and inverse kinematics for the robot. Also, a form of the Jacobian is derived that relates the actuated joint torques to the tip force.

5.1.1 Forward Kinematics

The forward kinematics are used to convert the base joint angles, θ_A and θ_B , into tip coordinates, x and y . There currently exists no simple equation that computes the forward kinematics of an arbitrary five-bar linkage. The difficulty arises because the joint angles θ_C and θ_E are not measured. This prevents the use of a 2 x 2 Jacobian of the form shown in Equations 4.1 through 4.4 to be used to compute endpoint position. Therefore a procedure was developed that uses several geometric relationships among the variables shown in Figure 5.1. The interior lengths, L_{BE} and L_{CE} , are computed from the law of cosines. The interior joint angles, ϕ_i , are all determined using the law of cosines or simple geometric relationships. The joint angles, θ_E and θ_C are then computed using the

interior joint angles. Finally, the tip position is determined by summing the vectors from the origin to the tip on the left hand side. The forward kinematics are implemented with the following algorithm:

$$L_{BE} = \sqrt{L_{AE}^2 + L_{AB}^2 - 2L_{AE}L_{AB} \cos \theta_A} \quad (5.1)$$

If $L_{AB} = 0$:

$$\phi_1 = 180^\circ - \theta_A \quad (5.2)$$

Otherwise:

$$\phi_1 = \cos^{-1} \left(\frac{L_{AB}^2 + L_{BE}^2 - L_{AE}^2}{2L_{AB}L_{BE}} \right) \quad (5.3)$$

$$\phi_2 = \cos^{-1} \left(\frac{L_{AE}^2 + L_{BE}^2 - L_{AB}^2}{2L_{AE}L_{BE}} \right) \quad (5.4)$$

$$\phi_3 = 180^\circ - \theta_B - \phi_1 \quad (5.5)$$

$$L_{CE} = \sqrt{L_{BC}^2 + L_{BE}^2 - 2L_{BC}L_{BE} \cos \phi_3} \quad (5.6)$$

$$\phi_4 = \cos^{-1} \left(\frac{L_{BE}^2 + L_{CE}^2 - L_{BC}^2}{2L_{BE}L_{CE}} \right) \quad (5.7)$$

$$\phi_5 = \cos^{-1} \left(\frac{L_{BC}^2 + L_{CE}^2 - L_{BE}^2}{2L_{BC}L_{CE}} \right) \quad (5.8)$$

$$\phi_6 = \cos^{-1} \left(\frac{L_{CD}^2 + L_{CE}^2 - L_{ED}^2}{2L_{CD}L_{CE}} \right) \quad (5.9)$$

$$\phi_7 = \cos^{-1} \left(\frac{L_{ED}^2 + L_{CE}^2 - L_{CD}^2}{2L_{ED}L_{CE}} \right) \quad (5.10)$$

$$\phi_8 = 180^\circ - \phi_6 - \phi_7 \quad (5.11)$$

$$\theta_E = 180^\circ + \phi_2 + \phi_4 + \phi_7 \quad (5.12)$$

$$\theta_c = 180^\circ - \phi_5 - \phi_6 \quad (5.13)$$

$$x = L_{AE} \cos \theta_A + L_{ED} \cos(\theta_A + \theta_E) - \frac{L_{AB}}{2} \quad (5.14)$$

$$y = L_{AE} \sin \theta_A + L_{ED} \sin(\theta_A + \theta_E) \quad (5.15)$$

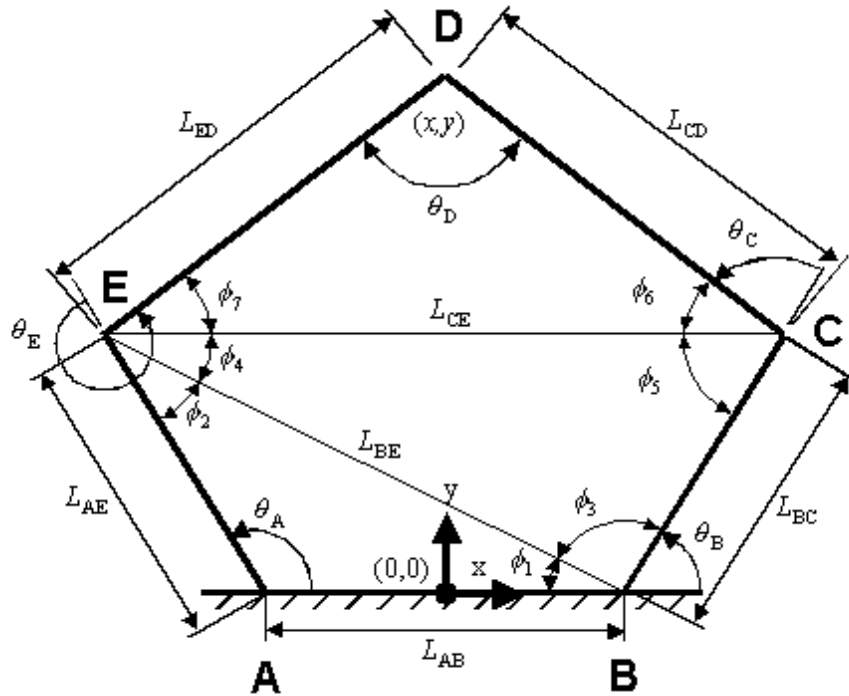


Figure 5.1. Key Dimensions for Forward Kinematics

If the shape enclosed by the robot links is a parallelogram (such as in the 3-brake configuration), the forward kinematics can be greatly simplified. The forward kinematics can then be computed by the following equations:

$$x = L_{BC} \cos \theta_B + L_{CD} \cos \theta_A \quad (5.16)$$

$$y = L_{BC} \sin \theta_B + L_{CD} \sin \theta_A \quad (5.17)$$

5.1.2 Inverse Kinematics

A similar procedure to the forward kinematics was used to solve for the inverse kinematics. In this case a separate procedure must be used to handle the case where L_{AB} equals zero. The key variables for the inverse kinematics formulation for nonzero L_{AB} are shown in Figure 5.2. The internal lengths L_{OD} , L_{AD} , and L_{ED} are computed as the distance from the tip to the corresponding points on the base. The internal angles, λ_i , are determined from the law of cosines. Finally, the base joint angles are computed using the internal angles. The algorithm is listed below.

$$L_{OD} = \sqrt{x^2 + y^2} \quad (5.18)$$

$$L_{BD} = \sqrt{\left(x - \frac{L_{AB}}{2}\right)^2 + y^2} \quad (5.19)$$

$$L_{AD} = \sqrt{\left(x + \frac{L_{AB}}{2}\right)^2 + y^2} \quad (5.20)$$

$$\lambda_1 = \cos^{-1} \left(\frac{\left(\frac{L_{AB}}{2}\right)^2 + L_{BD}^2 - L_{OD}^2}{L_{AB} L_{BD}} \right) \quad (5.21)$$

$$\lambda_2 = \cos^{-1} \left(\frac{L_{BC}^2 + L_{BD}^2 - L_{CD}^2}{L_{BC} L_{BD}} \right) \quad (5.22)$$

$$\lambda_3 = \cos^{-1} \left(\frac{\left(\frac{L_{AB}}{2}\right)^2 + L_{AD}^2 - L_{OD}^2}{L_{AB} L_{AD}} \right) \quad (5.23)$$

$$\lambda_4 = \cos^{-1} \left(\frac{L_{AE}^2 + L_{AD}^2 - L_{ED}^2}{L_{AE} L_{AD}} \right) \quad (5.24)$$

$$\theta_A = \lambda_3 + \lambda_4 \quad (5.25)$$

$$\theta_B = 180^\circ - \lambda_1 - \lambda_2 \quad (5.26)$$

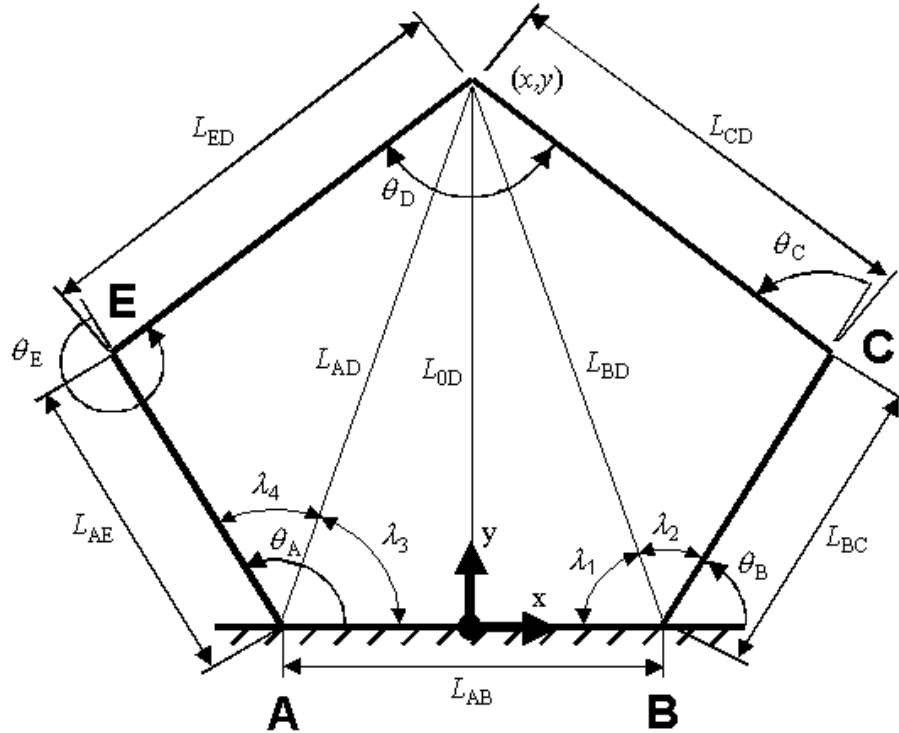


Figure 5.2. Key Dimensions for Inverse Kinematics ($L_{AB} \neq 0$)

If the robot is configured such the base joint axes are collinear, the key dimensions shown in Figure 5.3 are used. A similar method to the previous one is used, except the angle ψ_1 must be computed in addition to the internal angles, ψ_2 and ψ_3 . The inverse kinematics are then given by the following algorithm:

$$L_{0D} = \sqrt{x^2 + y^2} \quad (5.27)$$

$$\psi_1 = 90^\circ - \tan^{-1}\left(\frac{x}{y}\right) \quad (5.28)$$

$$\psi_2 = \cos^{-1} \left(\frac{L_{BC}^2 + L_{0D}^2 - L_{CD}^2}{2L_{BC}L_{0D}} \right) \quad (5.29)$$

$$\psi_3 = \cos^{-1} \left(\frac{L_{AE}^2 + L_{0D}^2 - L_{ED}^2}{2L_{AE}L_{0D}} \right) \quad (5.30)$$

$$\theta_A = \psi_1 + \psi_3 \quad (5.31)$$

$$\theta_B = \psi_1 - \psi_2 \quad (5.32)$$

The validity of the forward and inverse kinematics was confirmed by the following method. The tip position was computed from the base joint angles using the forward kinematics. The inverse kinematics were then used to translate this tip position into base joint angles, which were compared to the original angles. This was repeated for several base joint angles and arm lengths.

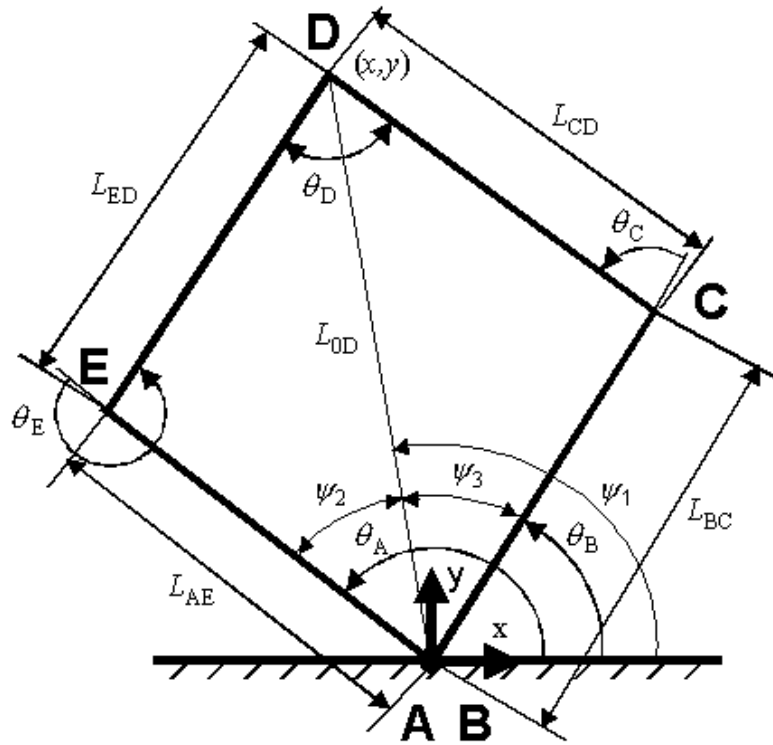


Figure 5.3. Key Dimensions for Inverse Kinematics ($L_{AB} = 0$)

5.1.3 Jacobian

A form of the Jacobian is needed such that joint torques can be related to tip forces. Since the robot is actuated by four brakes, a 2 x 2 Jacobian will not suffice. Instead, a 4 x 2 Jacobian of the form shown below is used, where F is force and τ is torque.

$$\begin{bmatrix} F_x \\ F_y \end{bmatrix} = \mathbf{J}^T \begin{bmatrix} \tau_A \\ \tau_E \\ \tau_B \\ \tau_C \end{bmatrix} \quad (5.33)$$

The Jacobian, \mathbf{J} , is computed by starting with a simpler form of the forward kinematics:

$$\begin{aligned} \begin{bmatrix} x \\ y \end{bmatrix} &= \begin{bmatrix} L_{AE} \cos(\theta_A) + L_{ED} \cos(\theta_A + \theta_E) - \frac{L_{AB}}{2} \\ L_{AE} \sin(\theta_A) + L_{ED} \sin(\theta_A + \theta_E) \end{bmatrix} \\ &= \begin{bmatrix} L_{BC} \cos(\theta_B) + L_{CD} \cos(\theta_B + \theta_C) + \frac{L_{AB}}{2} \\ L_{BC} \sin(\theta_B) + L_{CD} \sin(\theta_B + \theta_C) \end{bmatrix} \end{aligned} \quad (5.34)$$

Here it is assumed that the joint angles θ_C and θ_E are known. Thus it is necessary to solve for these angles using the forward kinematics procedure in Equations 5.1 through 5.13.

Differentiation of Equation 5.34 yields

$$\begin{bmatrix} \dot{x} \\ \dot{y} \end{bmatrix} = \mathbf{J}_1 \begin{bmatrix} \dot{\theta}_A \\ \dot{\theta}_E \end{bmatrix} = \mathbf{J}_2 \begin{bmatrix} \dot{\theta}_B \\ \dot{\theta}_C \end{bmatrix}, \quad (5.35)$$

where

$$\mathbf{J}_1 = \begin{bmatrix} -L_{AE} \sin \theta_A - L_{ED} \sin(\theta_A + \theta_E) & -L_{ED} \sin(\theta_A + \theta_E) \\ L_{AE} \cos \theta_A + L_{ED} \cos(\theta_A + \theta_E) & L_{ED} \cos(\theta_A + \theta_E) \end{bmatrix} \quad (5.36)$$

$$\mathbf{J}_2 = \begin{bmatrix} -L_{BC} \sin \theta_B - L_{CD} \sin(\theta_B + \theta_C) & -L_{CD} \sin(\theta_B + \theta_C) \\ L_{BC} \cos \theta_B + L_{CD} \cos(\theta_B + \theta_C) & L_{CD} \cos(\theta_B + \theta_C) \end{bmatrix}. \quad (5.37)$$

Using a power balance of the form,

$$\boldsymbol{\tau}\dot{\boldsymbol{\theta}} = \mathbf{F}\dot{\mathbf{x}}, \quad (5.38)$$

the preceding equations can be manipulated to yield the following relationship:

$$\mathbf{J}^T = \left[(\mathbf{J}_1^{-1})^T \quad (\mathbf{J}_2^{-1})^T \right]. \quad (5.39)$$

It should be noted that it is impossible to compute a unique set of joint torques from the tip forces since \mathbf{J}^T is noninvertible. This is a direct result of the system being a parallel manipulator with more actuators than degrees of freedom. Also, since the solution shown in Equation 5.39 is computationally intensive, the Jacobian is calculated numerically based on current position when needed.

5.2 Equations of Motion

A dynamic model is necessary in order to fully understand the behavior of the robot and to develop a simulation where new control concepts can be debugged and evaluated offline. A general form of the equations of motion is given by

$$\mathbf{Q} = \mathbf{M}(\mathbf{q})\ddot{\mathbf{q}} + \mathbf{V}(\mathbf{q}, \dot{\mathbf{q}}) + \mathbf{G}(\mathbf{q}), \quad (5.40)$$

where

\mathbf{q} = generalized coordinates

\mathbf{Q} = generalized forces

\mathbf{M} = mass matrix

\mathbf{V} = nonlinear terms

\mathbf{G} = gravity terms

The equations of motion for the robot were computed using Lagrange's equation,

$$Q_j + \sum_{i=1}^k \lambda_j \frac{\partial C_i}{\partial q_j} = \frac{d}{dt} \left(\frac{\partial L}{\partial \dot{q}_j} \right) - \frac{\partial L}{\partial q_j} \quad j = 1 \text{ to } n, \quad (5.41)$$

where

$$\begin{aligned}
L &= T - U \\
T &= \text{kinetic energy} \\
U &= \text{potential energy} \\
\lambda_j &= \text{Lagrangemultipliers} \\
C_i &= \text{constraints} \\
n &= \text{number of generalized coordinates} \\
k &= \text{number of constraints}
\end{aligned}$$

The number of constraints is determined as the difference between the number of generalized coordinates and the number of degrees of freedom of the device [1]. A constraint can be generated by writing a unique expression for a closed loop kinematic chain in terms of the generalized coordinates.

A 2-DOF system with four actuators requires a minimum of 4 generalized coordinates and forces. However, by adding additional generalized coordinates and constraints, the model can be greatly simplified. Due to the use of more actuators than degrees of freedom, a minimum of two constraints must be added to the model such that it can be solved. The endpoint position, x and y , was added to the generalized coordinates because four unique constraints can be written for this point. Furthermore, it allows for a payload attached to the endpoint to easily be added to the model. Four additional generalized coordinates were added at the centers of mass of arms ED (x_{ED} and y_{ED}) and CD (x_{CD} and y_{CD}). Having these variables available simplifies the computation of kinetic energy for links ED and CD and eliminates the need for nonlinear terms, \mathbf{V} . The generalized forces for these points are zero because no force acts on them. The generalized coordinates and forces used in this model are shown below.

$$\mathbf{q} = [x \quad y \quad \theta_A \quad \theta_E \quad x_{ED} \quad y_{ED} \quad \theta_B \quad \theta_C \quad x_{CD} \quad y_{CD}]^T \quad (5.42)$$

$$\mathbf{Q} = [F_x \quad F_y \quad \tau_A \quad \tau_E \quad 0 \quad 0 \quad \tau_B \quad \tau_C \quad 0 \quad 0]^T \quad (5.43)$$

The set of constraints are defined in Equations 5.44 through 5.51.

$$C_1 = L_{AE} \cos \theta_A + L_{ED} \cos(\theta_A + \theta_E) - \frac{L_{AB}}{2} - x = 0 \quad (5.44)$$

$$C_2 = L_{AE} \sin \theta_A + L_{ED} \sin(\theta_A + \theta_E) - y = 0 \quad (5.45)$$

$$C_3 = L_{BC} \cos \theta_B + L_{CD} \cos(\theta_B + \theta_C) + \frac{L_{AB}}{2} - x = 0 \quad (5.46)$$

$$C_4 = L_{BC} \sin \theta_B + L_{CD} \sin(\theta_B + \theta_C) - y = 0 \quad (5.47)$$

$$C_5 = L_{AE} \cos \theta_A + l_{ED} \cos(\theta_A + \theta_E) - \frac{L_{AB}}{2} - x_{ED} = 0 \quad (5.48)$$

$$C_6 = L_{AE} \sin \theta_A + l_{ED} \sin(\theta_A + \theta_E) - y_{ED} = 0 \quad (5.49)$$

$$C_7 = L_{BC} \cos \theta_B + l_{CD} \cos(\theta_B + \theta_C) + \frac{L_{AB}}{2} - x_{CD} = 0 \quad (5.50)$$

$$C_8 = L_{BC} \sin \theta_B + l_{CD} \sin(\theta_B + \theta_C) - y_{CD} = 0 \quad (5.51)$$

Since the robot operates in a horizontal plane, $\mathbf{G}(\mathbf{q})$ is zero. Also, potential energy need not be considered since there are no energy storage elements. Based on these simplifications, the equations of motion can be expressed as

$$\mathbf{M}(\mathbf{q})\ddot{\mathbf{q}} = \mathbf{Q} + \mathbf{A}^T \boldsymbol{\lambda}. \quad (5.52)$$

The mass matrix, \mathbf{M} , is given by

$$\mathbf{M} = \begin{bmatrix} \mathbf{M}_D & 0 & 0 & 0 & 0 \\ 0 & \mathbf{M}_{AE} & 0 & 0 & 0 \\ 0 & 0 & \mathbf{M}_{ED} & 0 & 0 \\ 0 & 0 & 0 & \mathbf{M}_{BC} & 0 \\ 0 & 0 & 0 & 0 & \mathbf{M}_{CD} \end{bmatrix}, \quad (5.53)$$

where

$$\mathbf{M}_D = \begin{bmatrix} m_D & 0 \\ 0 & m_D \end{bmatrix} \quad (5.54)$$

$$\mathbf{M}_{AE} = \begin{bmatrix} I_{AE} + m_{AE}l_{AE}^2 + I_{ED} & I_{ED} \\ I_{ED} & I_{ED} \end{bmatrix} \quad (5.55)$$

$$\mathbf{M}_{ED} = \begin{bmatrix} m_{ED} & 0 \\ 0 & m_{ED} \end{bmatrix} \quad (5.56)$$

$$\mathbf{M}_{BC} = \begin{bmatrix} I_{BC} + m_{BC}l_{BC}^2 + I_{CD} & I_{CD} \\ I_{CD} & I_{CD} \end{bmatrix} \quad (5.57)$$

$$\mathbf{M}_{CD} = \begin{bmatrix} m_{CD} & 0 \\ 0 & m_{CD} \end{bmatrix}. \quad (5.58)$$

\mathbf{A} is the constraint matrix, which is computed by

$$\mathbf{A}_{i,j} = \frac{\partial C_i}{\partial q_j} \quad i = 1 \text{ to } h, j = 1 \text{ to } g, \quad (5.59)$$

where h is the number of generalized coordinates and g is the number of constraints. The constraint matrix, \mathbf{A} , is then given by

$$\mathbf{A} = \begin{bmatrix} -\mathbf{I} & \mathbf{A}_{xy1} & 0 & 0 & 0 \\ -\mathbf{I} & 0 & 0 & \mathbf{A}_{xy2} & 0 \\ 0 & \mathbf{A}_{ED} & -\mathbf{I} & 0 & 0 \\ 0 & 0 & 0 & \mathbf{A}_{CD} & -\mathbf{I} \end{bmatrix}, \quad (5.60)$$

where

$$\mathbf{I} = \begin{bmatrix} 1 & 0 \\ 0 & 1 \end{bmatrix} \quad (5.61)$$

$$\mathbf{A}_{xy1} = \begin{bmatrix} -L_{AE} \sin \theta_A - L_{ED} \sin(\theta_A + \theta_E) & -L_{ED} \sin(\theta_A + \theta_E) \\ L_{AE} \cos \theta_A + L_{ED} \cos(\theta_A + \theta_E) & L_{ED} \cos(\theta_A + \theta_E) \end{bmatrix} \quad (5.62)$$

$$\mathbf{A}_{xy2} = \begin{bmatrix} -L_{BC} \sin \theta_B - L_{CD} \sin(\theta_B + \theta_C) & -L_{CD} \sin(\theta_B + \theta_C) \\ L_{BC} \cos \theta_B + L_{CD} \cos(\theta_B + \theta_C) & L_{CD} \cos(\theta_B + \theta_C) \end{bmatrix} \quad (5.63)$$

$$\mathbf{A}_{ED} = \begin{bmatrix} -L_{AE} \sin \theta_A - l_{ED} \sin(\theta_A + \theta_E) & -l_{ED} \sin(\theta_A + \theta_E) \\ L_{AE} \cos \theta_A + l_{ED} \cos(\theta_A + \theta_E) & l_{ED} \cos(\theta_A + \theta_E) \end{bmatrix} \quad (5.64)$$

$$\mathbf{A}_{CD} = \begin{bmatrix} -L_{BC} \sin \theta_B - l_{CD} \sin(\theta_B + \theta_C) & -l_{CD} \sin(\theta_B + \theta_C) \\ L_{BC} \cos \theta_B + l_{CD} \cos(\theta_B + \theta_C) & l_{CD} \cos(\theta_B + \theta_C) \end{bmatrix}. \quad (5.65)$$

The full derivation of this model, including all derivatives, can be found in Appendix A. The model parameters are shown graphically in Figure 5.4 and numerically in Table 5.1. The mass and inertia of each arm includes all components that attach directly to it. All inertial properties were determined using I-DEAS 8.0.

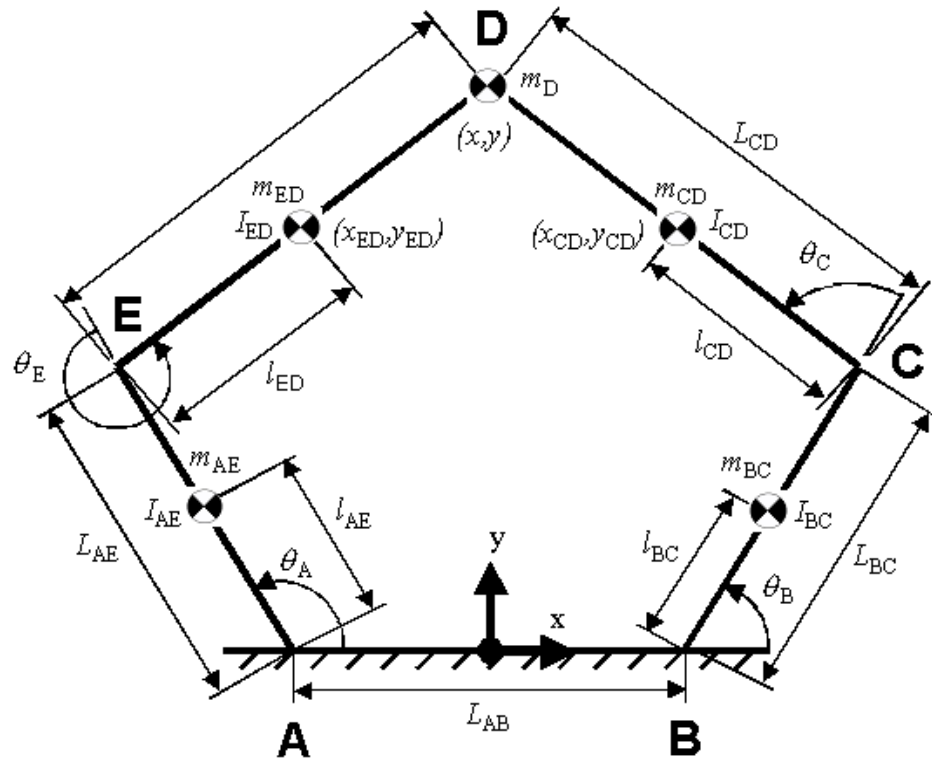


Figure 5.4. Key Dimensions and Variables for Robot Model

Table 5.1. Key Dimensions and Variables for Robot Model

Component	3-Brake				4-Brake			
	m (kg)	I (kgm ²)	L (m)	l (m)	m (kg)	I (kgm ²)	L (m)	l (m)
Arm AE	3.70	0.0661	0.305	0.166	3.70	0.0535	0.264	0.152
Arm ED	2.74	0.0336	0.305	0.096	2.74	0.0336	0.305	0.096
Arm BC	2.62	0.0355	0.305	0.109	3.70	0.0535	0.264	0.152
Arm CD	2.59	0.0355	0.305	0.188	3.48	0.0593	0.305	0.140
Length AB	--	--	0	--	--	--	0.267	--
Point D	0	--	--	--	0	--	--	--

5.3 Simulation

A simulation was devised based on the model presented above using a combination of Simulink models and MATLAB m-files. A block diagram representing the robot simulation is shown in Figure 5.5. At each time step a single integration block computes the position and velocity vectors from the previous velocity and acceleration vectors. The simulation consists of five main blocks representing the encoders, the forward kinematics and velocity, the controller, the brakes, and computation of acceleration. The following sections explain the function of each block in greater detail.

5.3.1 Encoders

The encoder block is designed to replicate the signals detected by the encoders on the robot. The base joint angles, θ_A and θ_B , are quantized at $.000360^\circ$ to match the resolution of the encoders.

5.3.4 Brakes

The brakes block computes the yield torque of each actuated joint based upon the shaft speed and applied current. Each of the three or four brakes is represented by a model of the form shown in Figure 3.6. The only difference is that yield torque is always positive and must lie between the off-state torque and the torque at maximum current (1 A). The sign and magnitude of actual torque is determined by the acceleration block.

5.3.5 Acceleration

The acceleration block is responsible for calculation of the acceleration vector, $\ddot{\mathbf{q}}$. The acceleration can be determined from the model parameters, generalized forces, and velocity vector using the following relationship [1]:

$$\begin{bmatrix} \mathbf{M} & -\mathbf{A}^T \\ -\mathbf{A} & 0 \end{bmatrix} \begin{bmatrix} \ddot{\mathbf{q}} \\ \lambda \end{bmatrix} = \begin{bmatrix} \mathbf{Q} \\ \dot{\mathbf{A}}\dot{\mathbf{q}} \end{bmatrix}. \quad (5.66)$$

The derivation of $\dot{\mathbf{A}}$ is shown in Equations A.42 through A.46 in the Appendix.

The challenge in this simulation lies in computing each of three or four braking torques in a 2-DOF device. As explained in Chapter 3, the MR fluid brakes exhibit Coulomb friction behavior. Therefore a numerical model is necessary to characterize this discontinuous behavior. A variation of the Karnopp friction model used by Swanson [22] in the simulation of PTER was selected:

$$\tau_i = \begin{cases} \tau_{i,y}, & |\omega| \geq \delta\omega \\ \tau_{i,y}, & |\omega| < \delta\omega, |\tau_{i,a}| > \tau_{i,y} \\ \tau_{i,a}, & |\omega| < \delta\omega, |\tau_{i,a}| \leq \tau_{i,y} \end{cases} \quad (5.67)$$

where

τ_i = brake torque
 $\tau_{i,y}$ = yield torque
 $\tau_{i,a}$ = applied torque
 ω = angular velocity
 $\delta\omega$ = very small angular velocity

If angular velocity is very close to zero and the magnitude of applied torque is less than yield torque, the model predicts that the brake will stick. Otherwise, the brake is in slip mode and torque is set to the yield torque from the brake model. The sign of the torque on each actuated joint is then determined as the negative sign of the corresponding joint velocity. However, if the absolute value of velocity is very small, the sign of the torque at the last time step is used. This ensures that the sign of torque is correct when a joint is transitioning from stuck to slip mode.

Calculation of applied torque is necessary in order to determine when a stuck brake will transition into slip mode. If the brake is in stuck mode, the torque applied by each brake is equal to the joint torque resulting from the user input force, F_x and F_y . These applied joint torques are computed using a method similar to that used by Swanson in the simulation of PTER [22]. If one brake is determined to be in the stuck mode, the applied torque is computed by solving the following equation with the acceleration of that joint set to zero:

$$\begin{bmatrix} \ddot{\mathbf{q}} \\ \boldsymbol{\lambda} \end{bmatrix} = \begin{bmatrix} \mathbf{M} & -\mathbf{A}^T \\ -\mathbf{A} & \mathbf{0} \end{bmatrix}^{-1} \begin{bmatrix} \mathbf{Q} \\ \dot{\mathbf{A}}\dot{\mathbf{q}} \end{bmatrix}. \quad (5.68)$$

This equation is simply a rearrangement of Equation 5.66. All of the terms in this equation are known except the torque at the stuck joint and the Lagrange multipliers. Putting the equation into this form allows a linear equation for applied torque to be pulled out that does not involve the Lagrange multipliers. This equation can be solved directly

for applied torque. If applied torque exceeds the breakaway (yield) torque, the brake torque is set to breakaway level and the joint begins to slip. If two brakes are locked, a similar procedure is used to solve for the two applied torques from two equations with two unknowns. If three or more brakes are locked, the equations extracted from Equation 5.68 are not linearly independent and cannot be used to solve for the applied torques. Again, this is a direct result of having more actuators than degrees of freedom.

If three or more brakes are in stuck mode, the applied torques are computed using the lumped actuator approach [22]. Here the entire system is stuck and one of three outcomes is possible. The system can either remain stuck (three or four brakes stuck) or transition to a free state with one or zero brakes stuck. If three brakes are in stuck mode, the torque on one brake is set to its breakaway value and the remaining applied torques are computed using the previous method. This step is repeated for each of the other two brakes. This results in three sets of possible brake torques. If both computed applied torques in any set are below their respective breakaway values, all three brakes remain stuck. If all computed applied torques exceed breakaway value, each brake is set to breakaway torque and all three brakes begin slipping. Otherwise the two brakes with the average applied torque closest to breakaway torque at the last time step are selected to slip. The torque on these brakes is set to breakaway value and the applied torque on the remaining joint is computed using Equation 5.68. If four brakes are in stuck mode, the same procedure is used except the torque on each set of two brakes is set to the breakaway value to compute six sets of possible torque values.

5.4 Simulation Verification

An experiment was devised to test how well the simulation predicts robot motion. An aluminum cylinder was secured to a location on the base. A constant force torsional spring was placed around the cylinder and attached on the other end to the handle using a PVC ring. A schematic of the setup is shown in Figure 5.6. The tip was held motionless and released from certain locations in the workspace. Separate experiments were conducted for free motion (no brakes actuated) and with full current supplied to each brake.

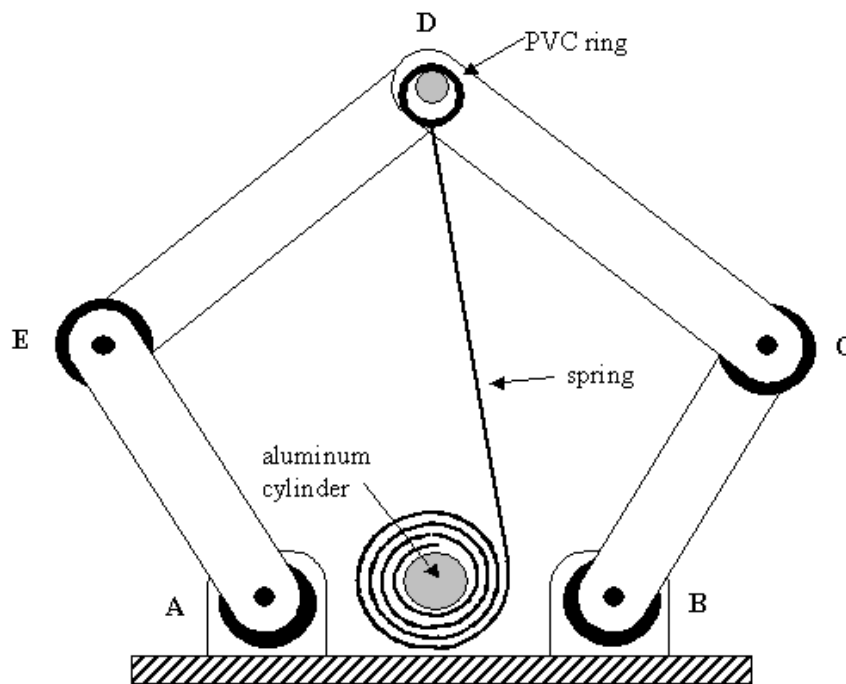


Figure 5.6. Schematic of Model Verification Tests

This experiment tests the validity of the equations of motion. Also, in the cases where a brake is locked, it tests the accuracy of the procedure that computes torque for

joints in stuck mode. A sample of the simulation verification data is shown in Figures 5.7a and 5.7b for the 3-brake configuration, and in Figures 5.8a and 5.8b for the 4-brake configuration. Each set of figures displays the position response relative to the robot workspace and relative to time. Representative trials for free motion and with brake A locked are shown here; additional results can be viewed in Appendix B. The simulation predicts a slightly faster response than the experimental data for the 3-brake configuration in free motion. However, with the exception of this case, there is negligible difference between the simulation output and the experimental data. These results indicate that the robot simulation is an effective tool for predicting motion and evaluating control techniques.

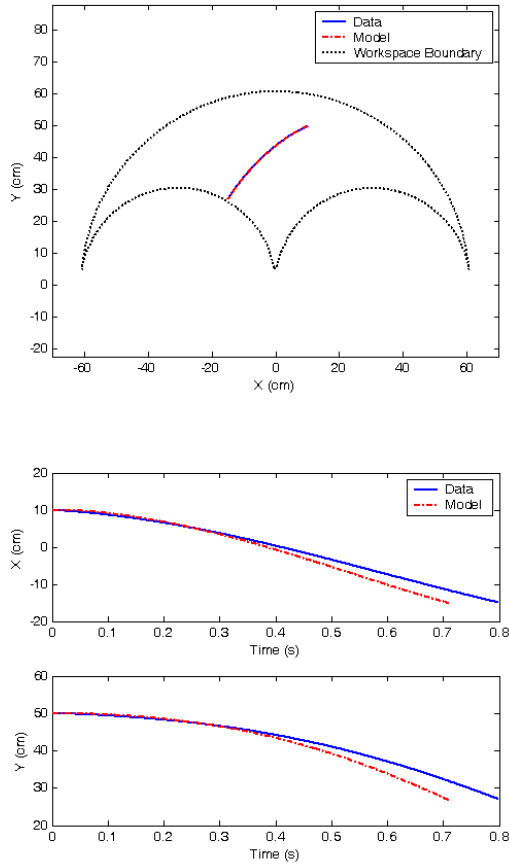


Figure 5.7a. Comparison of Model to Data for 3-Brake Configuration with Free Motion

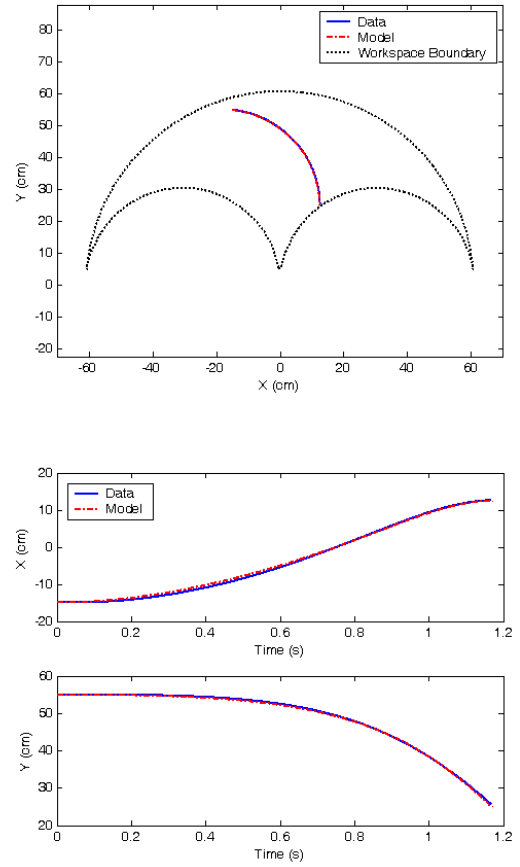


Figure 5.7b. Comparison of Model to Data for 3-Brake Configuration with Brake A Locked

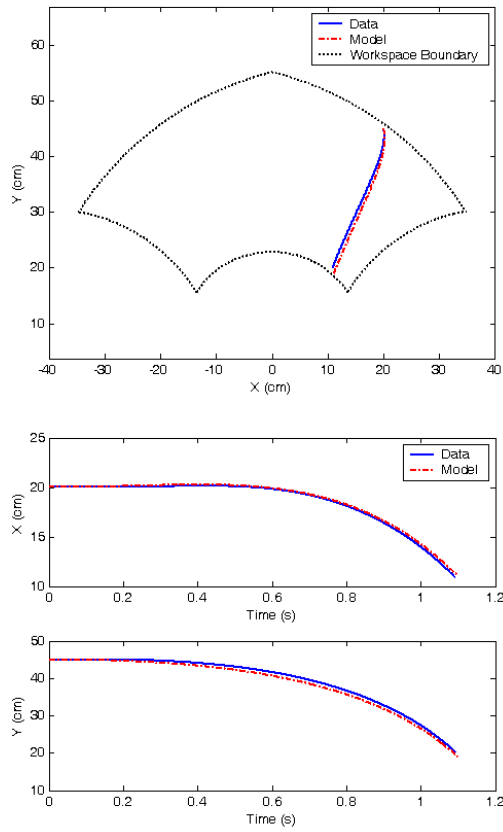


Figure 5.8a. Comparison of Model to Data for 4-Brake Configuration with Free Motion

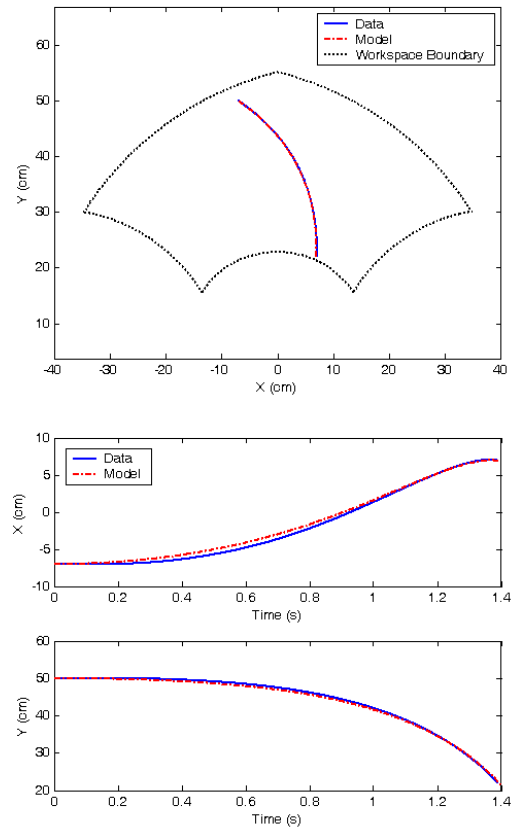


Figure 5.8b. Comparison of Model to Data for 4-Brake Configuration with Brake A Locked

CHAPTER 6

CONTROLLER DEVELOPMENT AND TESTING

The controllers investigated in this chapter focus on the path following problem. Two forms of velocity control are presented in Sections 6.2 and 6.3, which are based on an overall control framework that is discussed in Section 6.1. The main goal of these controllers is to minimize the distance from the endpoint to the desired path. However, since the robot interacts directly with humans, smoothness of operation and perceived workload must be considered. Initial testing with a set of human operators was performed and these qualities were examined using a set of proven performance metrics.

6.1 Controller Design

The control architecture is outlined in the block diagram shown in Figure 6.1. The system consists of four main blocks: desired velocity, velocity control, the Jacobian, and current gain. In the simulation block diagram (Figure 5.5), the output of the current gain is applied to the brake model in order to compute braking torque. In hardware, the output of current gain becomes the desired current signal for the appropriate amplifier, which then controls brake voltage using current feedback. The four main blocks are described in further detail in the following sections.

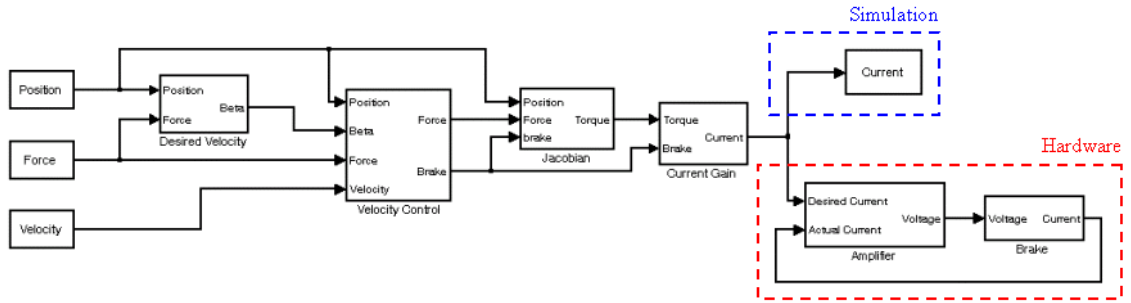


Figure 6.1. Controller Block Diagram

6.1.1 Desired Velocity

The desired velocity block computes the angular direction of desired velocity. A velocity field such as that used by Swanson was selected as the method for determining desired velocity [23]. A sample desired velocity field is shown in Figure 6.2, with the desired path set to the line $y = 40$ cm. Outside a specified boundary, the desired velocity always points toward the desired path. Within the boundary, the direction is linearly blended to the direction of the path. The direction of the path and the blend is determined by the direction of force input relative to the path. In this work, the boundary was set at a distance of 5 cm from the path.

6.1.2 Velocity Control

The velocity control block is responsible for deciding which, if any, brakes to actuate and the force contribution of each brake. Two forms of velocity control implemented in this block and are discussed in detail in Sections 6.2 and 6.3. The input of the desired velocity block is the desired velocity angle, β , and a combination of position, force, and/or velocity, depending on which controller is used. The output of the velocity control block is a desired tip force and the brake(s) that must generate that force. This method

assumes that the coupling effects on the link accelerations are negligible. The controllers presented in the following sections actuate only one brake at a time. However, they may act to immobilize the system by applying full current to all brakes if a locking condition is met.

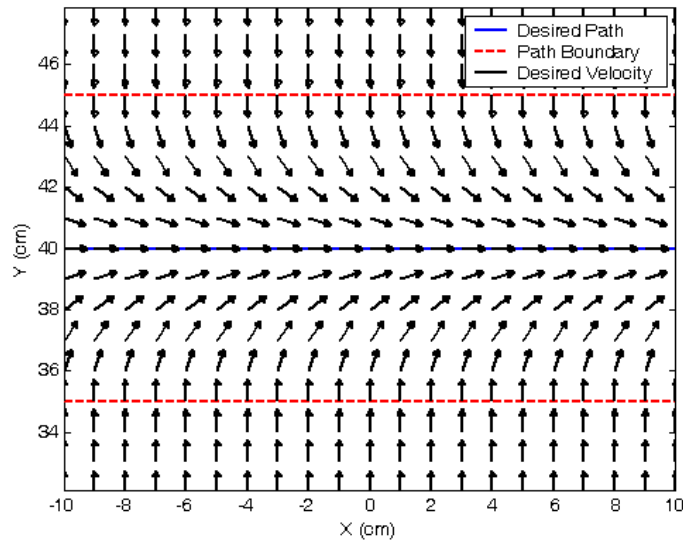


Figure 6.2. Sample Desired Velocity Field

Whenever the robot is in motion, each brake contributes a force to the tip. The direction of that force depends on the robot position. The force magnitude depends on the tip position and the current supplied to the brake. The desired force magnitude was normalized in order to create a consistent feel throughout the workspace. The maximum desired force output was set to the minimum force magnitude that can be generated among all brakes at maximum current. This was analyzed using the 4×2 Jacobian of Equation 5.33,

$$\begin{bmatrix} F_x \\ F_y \end{bmatrix} = \mathbf{J}^T \begin{bmatrix} \tau_A \\ \tau_E \\ \tau_B \\ \tau_C \end{bmatrix}, \quad (6.1)$$

where

$$\mathbf{J}^T = \begin{bmatrix} J_{Ax} & J_{Ex} & J_{Bx} & J_{Cx} \\ J_{Ay} & J_{Ey} & J_{By} & J_{Cy} \end{bmatrix}. \quad (6.2)$$

Each of the elements of \mathbf{J}^T is computed numerically based on tip position using the method described in Section 5.1.3. To analyze the force contribution of only one brake, the remaining joint torques are set to zero. The force magnitude can then be computed by the following formula:

$$|F_i| = |\tau_i| \sqrt{J_{ix}^2 + J_{iy}^2}, \quad (6.3)$$

where i represents the joint (A, E, B, or C). These equations were solved symbolically using MATLAB for each actuated joint to yield the following relationships:

$$|F_A| = \frac{|\tau_A|}{L_{AE} \cos(\theta_E + 90^\circ)} \quad (6.4)$$

$$|F_E| = \frac{|\tau_E| \sqrt{L_{ED}^2 + L_{AE}^2 + 2L_{ED}L_{AE} \cos \theta_E}}{L_{ED}L_{AE} \sin \theta_E} \quad (6.5)$$

$$|F_B| = \frac{|\tau_B|}{L_{BC} \cos(\theta_B + 90^\circ)} \quad (6.6)$$

$$|F_C| = \frac{|\tau_C| \sqrt{L_{CD}^2 + L_{BC}^2 + 2L_{CD}L_{BC} \cos \theta_C}}{L_{CD}L_{BC} \sin \theta_C}. \quad (6.7)$$

Interestingly, the force magnitude depends only on the angle θ_E for brakes A and E, and on θ_C for brakes B and C.

The torque gain equation (3.3) can be substituted for the torque in each of the preceding equations as follows:

$$\tau_i = K_i(I). \quad (6.8)$$

With current set to maximum value, the minimum force magnitude among Equations 6.4 through 6.7 can be determined by examining the entire valid range of θ_E and θ_C . Based on this analysis, maximum desired force magnitudes of 19.5 and 22.0 N were selected for the 3-brake and 4-brake configurations, respectively.

6.1.3 Jacobian

The Jacobian block uses the 4 x 2 Jacobian defined in Equations 5.36, 5.37, and 5.39 to compute the torque output of the appropriate brake that is needed to produce the desired force magnitude requested of the velocity control block. Since the force contribution from only one brake is considered, the remaining joint torques are set to zero and the equation has a unique solution.

6.1.4 Current Gain

The current gain block is the same as that shown in Figure 3.17 and is simply the inverse of the torque gain function described by Equation 3.3.

6.2 SDOF Velocity Control

The SDOF velocity controller operates by simply selecting the local SDOF path that most closely matches the desired velocity vector. The schematic shown in Figure 6.3 highlights the key parameters of SDOF control. The desired path in this case is a line at

angle α in the workspace. Any curve could be used as the desired path as long as the angle of the line of tangency is known at each point. The direction, β , of desired velocity, v_{des} , is determined by the desired velocity block. In this figure, four local SDOF paths, p_i , are available. The local SDOF path for each brake lies perpendicular to the force vector contributed by that brake. From Equations 6.1 and 6.2, the force angle for brake i is given by

$$\angle F_i = \tan^{-1}\left(\frac{F_y}{F_x}\right) = \tan^{-1}\left(\frac{J_{iy}}{J_{ix}}\right). \quad (6.9)$$

Therefore, the local SDOF path angle is given by

$$\angle p_i = \tan^{-1}\left(\frac{J_{iy}}{J_{ix}}\right) \pm 90^\circ. \quad (6.10)$$

The controller chooses to actuate the brake with the local SDOF path that points in the direction closest to the desired velocity vector. However, the selected local SDOF path direction must lie in the 90° span between vectors pointing parallel to the desired path in the direction of applied force and perpendicular toward the desired path. In the case shown in Figure 6.3, local SDOF paths p_2 and p_3 are valid, and p_2 would be selected. If a valid local SDOF path exists, the maximum normalized force is commanded to that brake. If there is no local SDOF path in the valid range, one of two control actions is taken. If the input force points away from the desired path, the system is locked. Otherwise, no brakes are actuated. Invalid solutions become possible when the maximum angle between local SDOF paths exceeds 90° .

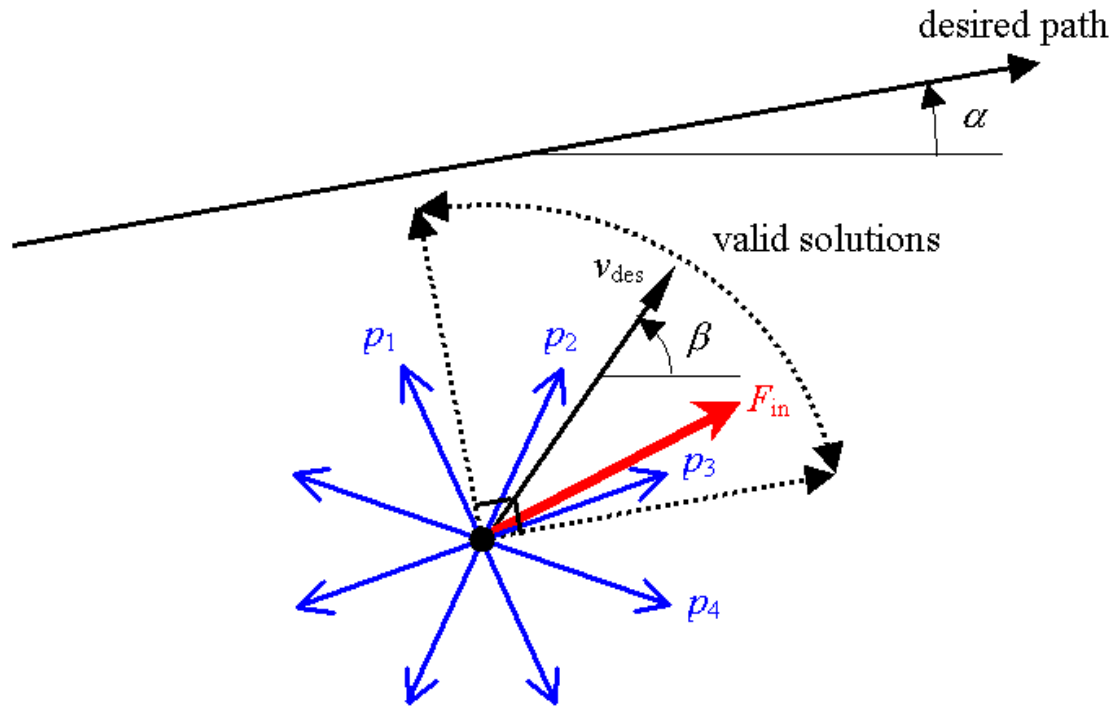


Figure 6.3. SDOF Velocity Control Schematic

6.3 Proportional Velocity Control

Proportional velocity control was adapted from Swanson's velocity ratio controller [23]. The main difference between the two controllers is that proportional velocity control operates in tip space while velocity ratio control operates in joint space. A schematic of the control technique and the necessary parameters are shown in Figure 6.4. The desired velocity is determined in the same way as the previous controller. The velocity is then decomposed into x- and y-components in the direction of desired velocity. The goal of the controller is to drive $v_{\beta y}$, the y-component of velocity in the desired velocity space, to zero by applying an appropriate force to the tip.

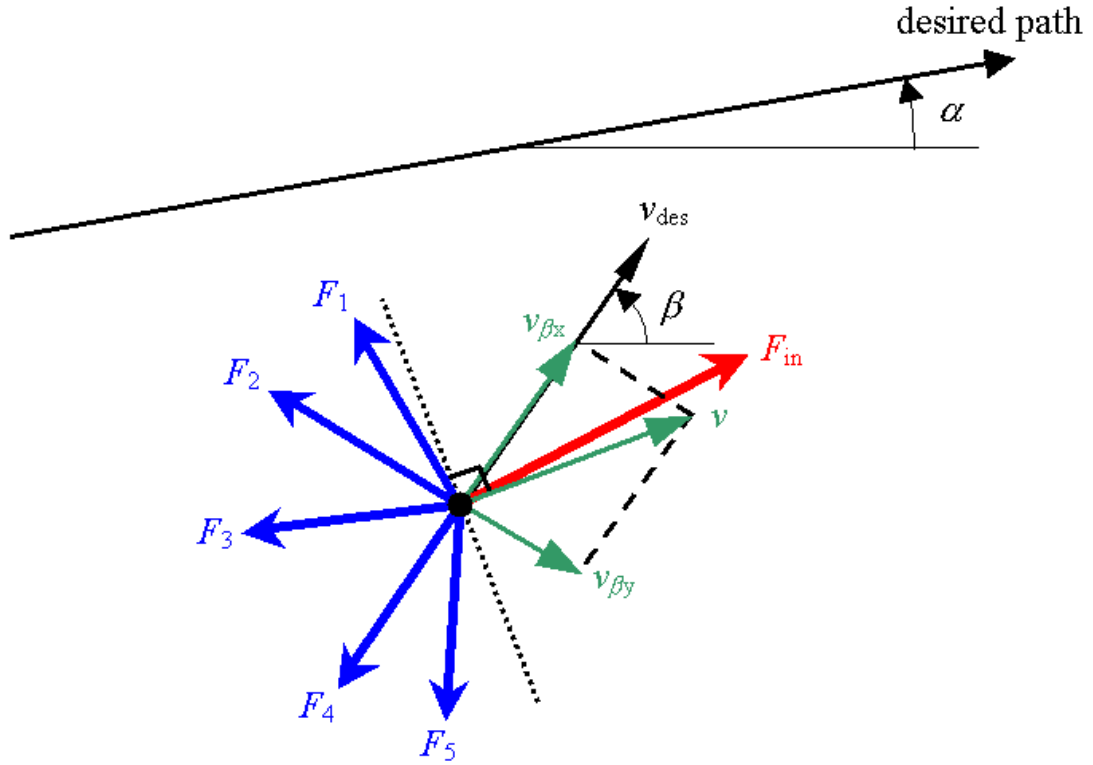


Figure 6.4. Proportional Velocity Control Schematic

The angle of each force is computed by the same method used in Equation 6.9. However, due to passivity constraints, the force contribution from each brake must act in a direction that opposes velocity. This constraint is indicated by the dotted line shown in Figure 6.5. Therefore the following method is used to calculate force angle:

$$\angle F_i = \begin{cases} \tan^{-1}\left(\frac{J_{iy}}{J_{ix}}\right), & F_i \cdot v < 0 \\ \tan^{-1}\left(\frac{J_{iy}}{J_{ix}}\right) + 180^\circ, & F_i \cdot v \geq 0 \end{cases} \quad (6.11)$$

Once the force direction of each brake is computed, a matrix, \mathbf{H} , of influence coefficients is formed. Each column of the influence matrix corresponds to a different brake. The first row corresponds to $v_{\beta x}$ and the second row correlates to $v_{\beta y}$. Each cell is assigned a 1

if the force from that brake will act to increase the magnitude of that velocity component, a value of -1 if the force will act to decrease the magnitude or change the direction of the velocity component, and a value of 0 if the force will have no effect. Although not applicable to this robot, Figure 6.5 shows five forces in order to demonstrate all possible cases. In this example, the influence matrix is given by

$$\mathbf{H} = \begin{bmatrix} 1 & 0 & -1 & -1 & -1 \\ -1 & -1 & -1 & 0 & 1 \end{bmatrix}. \quad (6.12)$$

It is most desirable to select a brake with the influence coefficients $[1 \ -1]^T$. In this case, the brake acts as a coupling actuator that transmits energy from the undesired direction to the desired direction. If this option is unavailable, priority shifts to brakes with influence coefficients of $[0 \ -1]^T$ and then to $[-1 \ -1]^T$. If any other set of influence coefficients are computed, then no brakes act to decrease the magnitude of v_{β_y} , and no brakes are actuated. If more than one brake share the best pair of influence coefficients, the brake with the force pointing in the direction closest to the desired velocity is selected. In accordance with the controller goal, that brake is then actuated according to the following control law:

$$F_i = K_y |v_{\beta_y}|, \quad (6.13)$$

where K_y is the proportional velocity controller gain. This controller can also lock the system under either of two conditions. The first results when no brakes are actuated and the input force points away from the desired path. The second occurs when v_{β_x} is less than zero.

6.4 Simulation Proof of Concept

The SDOF and proportional velocity controllers were implemented in simulation for purposes of debugging and evaluating their general effectiveness. A horizontal line placed at $y = 38$ cm was used as the desired path for both cases. The start point was set at 4 cm below the line. User input force was modeled with a constant x-component of 7 N and a y-component of 3 N pointing in the direction of the path.

Figures 6.5 and 6.6 show the simulation results for the SDOF velocity control in both configurations and Figure 6.7 and 6.8 show the results using proportional velocity control. Each set of figures displays the tip trajectory and the actuator commands for the controlled and uncontrolled case. In both cases, the 4-brake configuration exhibits slightly less path error than the 3-brake configuration. As expected, the proportional velocity controller exhibits much greater accuracy than the SDOF controller. The proportional controller also switches more rapidly between brakes.

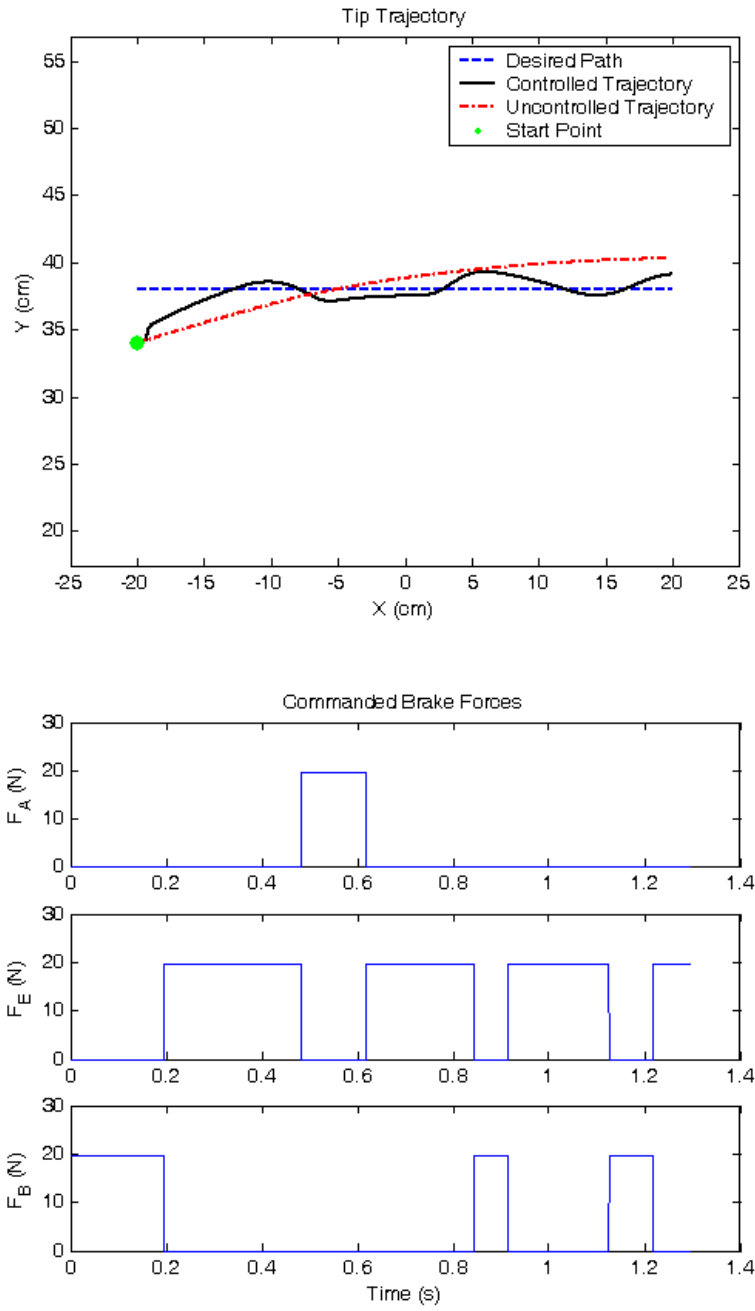


Figure 6.5. SDOF Velocity Control Simulation for 3-Brake Configuration

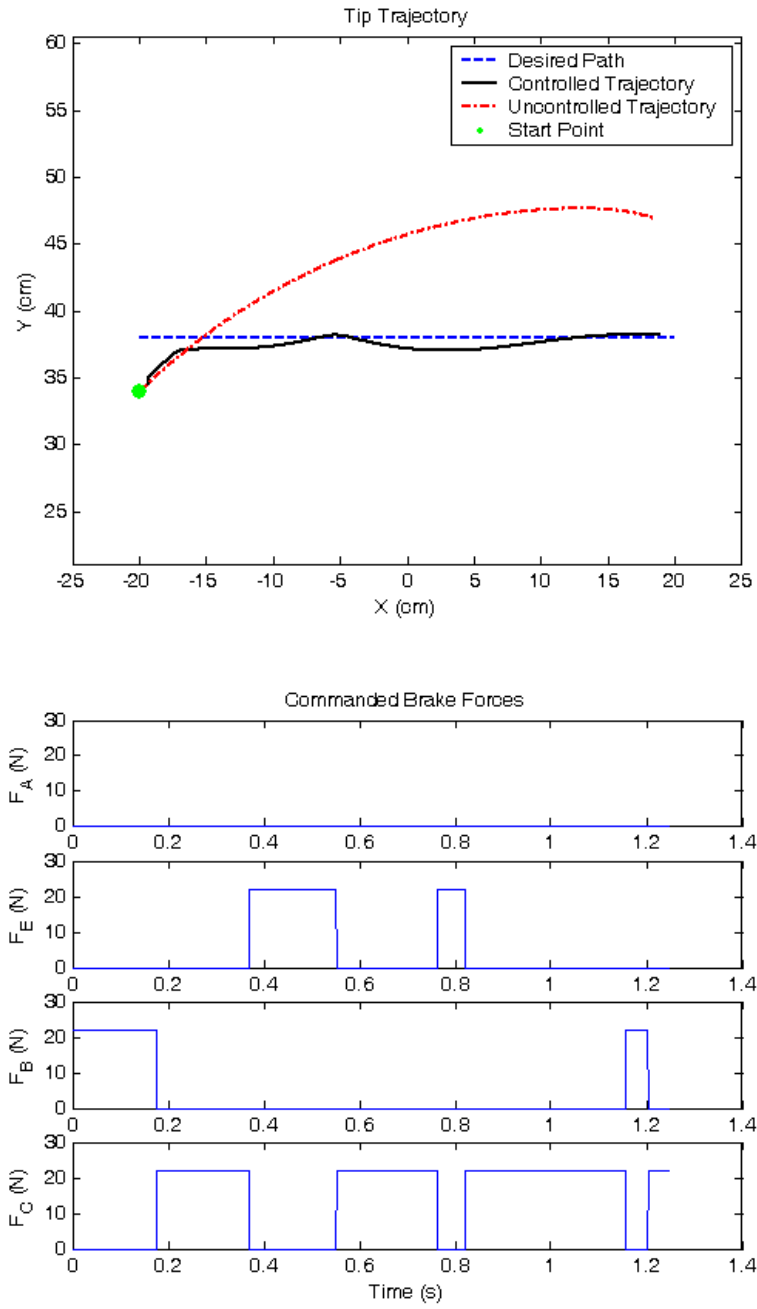


Figure 6.6. SDOF Velocity Control Simulation for 4-Brake Configuration

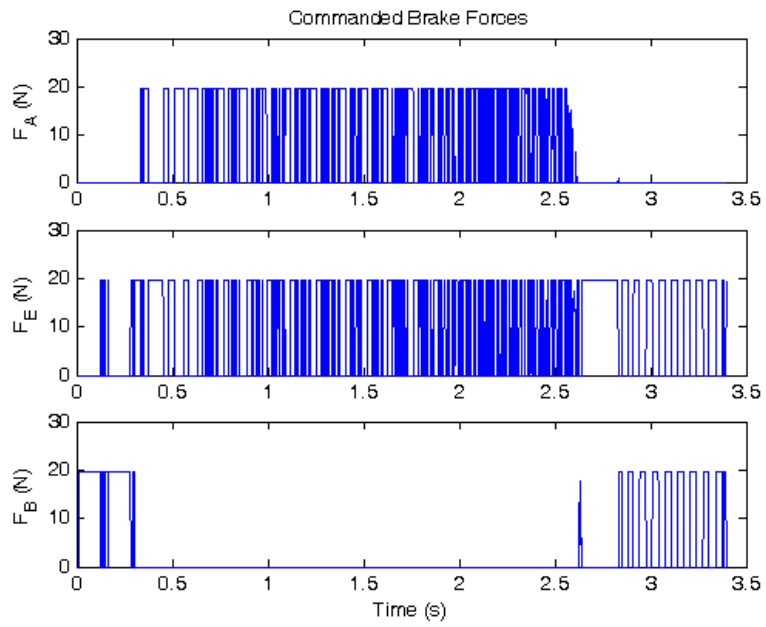
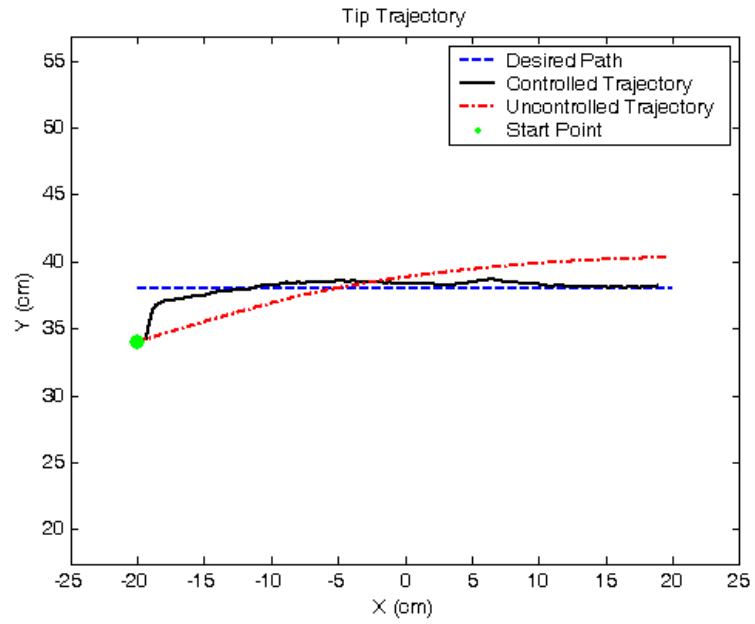


Figure 6.7. Proportional Velocity Control Simulation for 3-Brake Configuration

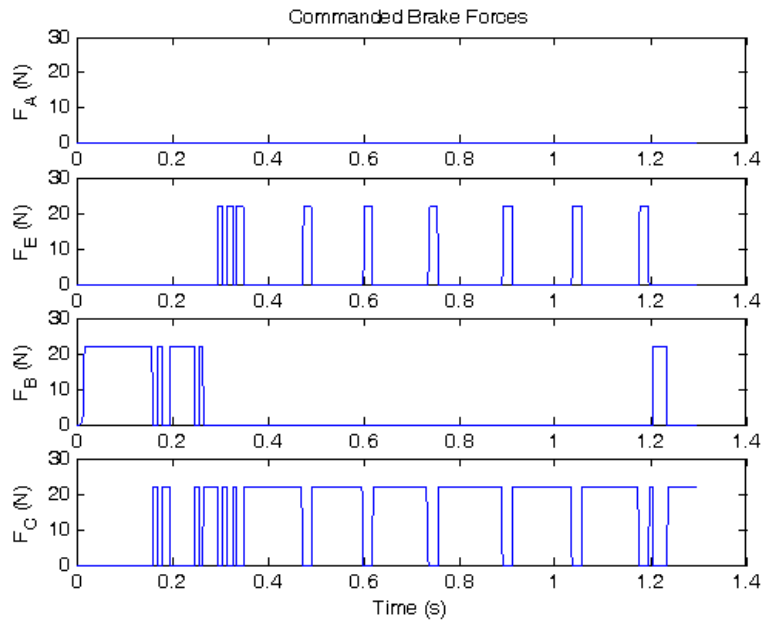
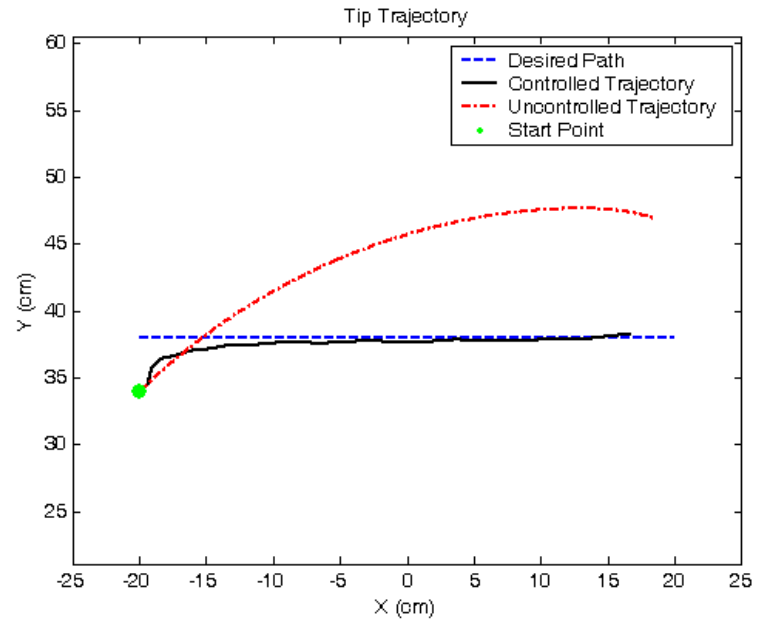


Figure 6.8. Proportional Velocity Control Simulation for 4-Brake Configuration

6.5 Preliminary Testing

Testing with human operator input was conducted in order to evaluate the performance of each controller and configuration. This section describes the design of experiments and the performance evaluation techniques.

6.5.1 Experiment Design

The SDOF and proportional velocity controllers were implemented in Simulink and interfaced to the dSPACE card using Real Time Workshop. A sampling rate of 1000 Hz was used for all experiments. Data was collected using dSPACE ControlDesk software. For the human operator experiments, the system was set up as shown in Figure 6.9. The computer monitor displayed the user interface shown in Figure 6.10. The large white graph displayed the desired path, the start and end points, and a real-time trace of tip position. Control initiated when the user exited the green circle and was shut off when the user entered the red circle. The users were instructed to follow the line to the best of their ability while maintaining an appropriate balance between accuracy and speed. The human operators consisted of three male graduate students with an interest in haptics research.

The human operator experiments tested five different controllers, as outlined in Table 6.1. The SDOF controller was tested as previously described and also with a gap surrounding the desired path within which no control action is taken. This capability was added to reduce the “jerkiness” felt when the controller rapidly switches brakes. The proportional velocity controller was tested with two gains. The high gain ensures

maximum normalized force is commanded to each actuated brake. The low gain was chosen such that there was no detectable vibration.

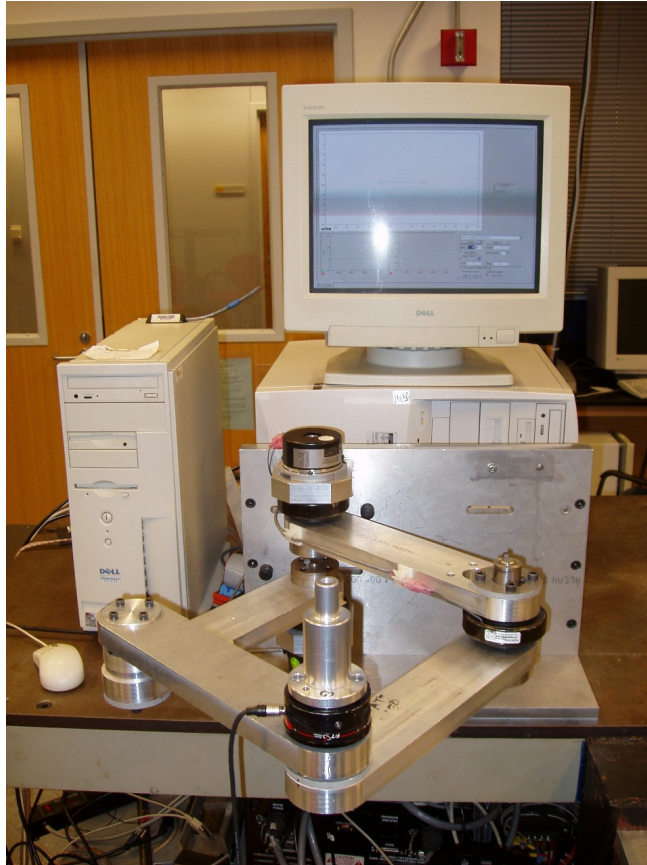


Figure 6.9. Experimental Setup for Human Subject Tests

Table 6.1. Control Methods

Experiment	Controller	Gap / Gain
1	None	--
2	SDOF without gap	0 cm
3	SDOF with gap	.50 cm
4	Proportional (low gain)	5 Ns/m
5	Proportional (high gain)	10,000 Ns/m

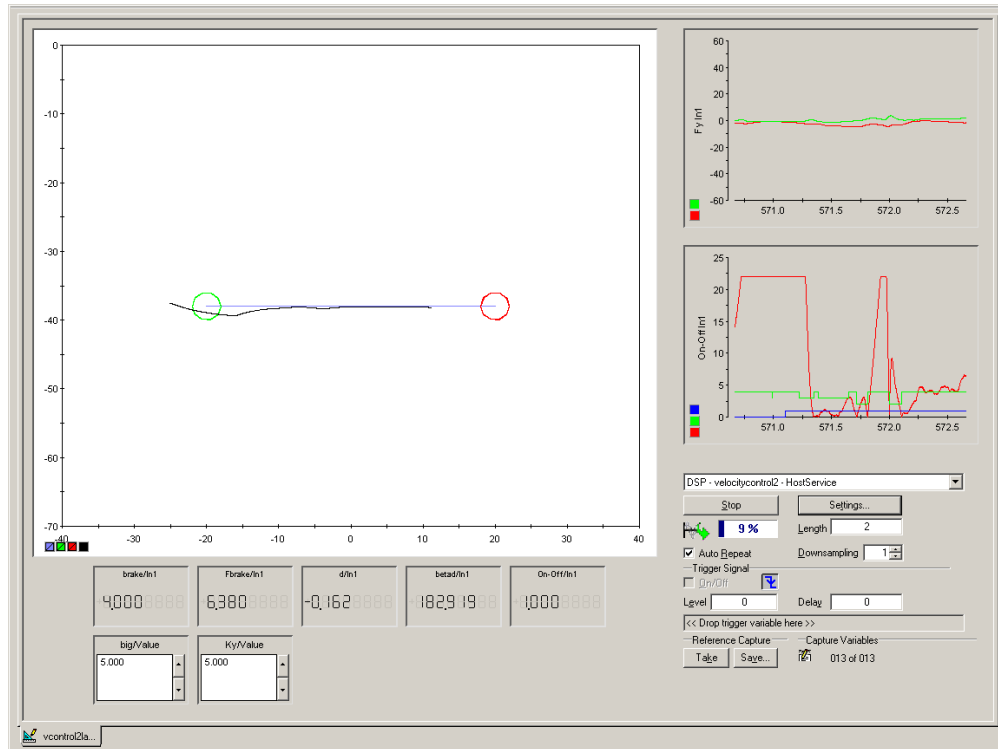


Figure 6.10. User Interface

Two separate line segments were selected as desired paths. As shown in Figure 6.9, both lines lie in the workspace of both robot configurations. Each operator was instructed to complete three practice trials followed immediately by three data collection trials for each set of experimental conditions. With three data sets for each combination of two lines, two configurations, five controllers, and three subjects, 180 total sets of data were analyzed. Five of these data sets were empty, which is most likely attributed to the operator not properly entering the green circle at the beginning of each trial. Therefore 175 data sets were analyzed.

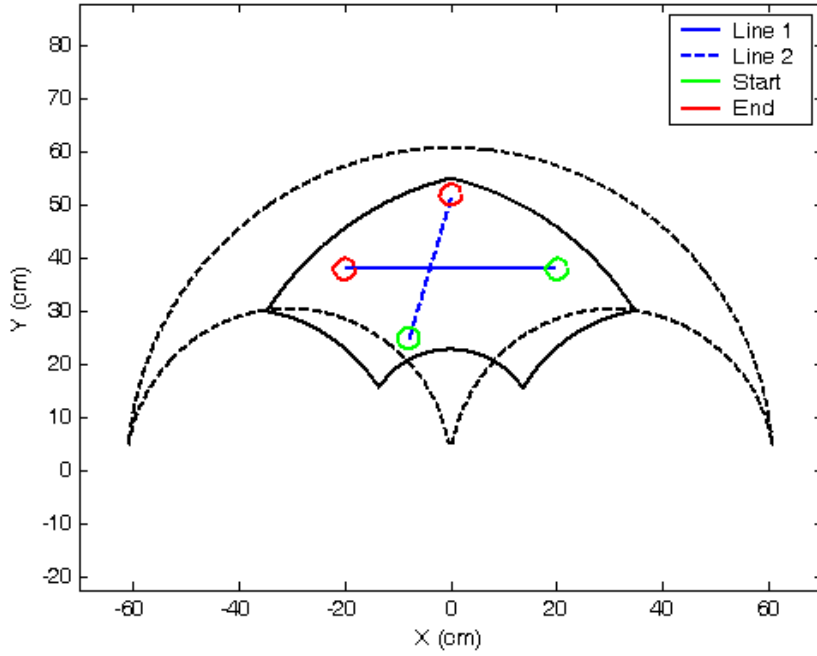


Figure 6.11. Desired Paths Selected for Control Experiments

6.5.2 Performance Evaluation

Three metrics were used to evaluate the performance of the various controllers. Together they quantify the accuracy, human workload, and smoothness of each controller.

Average path error, e_{avg} , measures how well the tip trajectory follows the desired path. It is computed using the following formula [23]:

$$e_{\text{avg}} = \frac{1}{L_p} \sum_{k=2}^{N-1} \varepsilon_k L_k, \quad (6.14)$$

where N is the number of data points and ε_k is the distance from the tip to the path at point k . The distance traveled during each time step, L_k , is approximated by

$$L_k = \frac{1}{2} \sqrt{(x_{k+1} - x_{k-1})^2 + (y_{k+1} - y_{k-1})^2}, \quad (6.15)$$

and the total path length, L_p , is given by

$$L_p = \sum_{k=2}^{N-1} L_k . \quad (6.16)$$

Since e_{avg} is computed as the average with respect to path length, this metric can be compared among different paths.

Time-average tip force, F_{avg} , was found by Swanson to correlate strongly with total user workload [23]. Average tip force was computed using the following formula:

$$F_{\text{avg}} = \frac{\sum_{k=1}^N \sqrt{F_{\text{xin},k}^2 + F_{\text{yin},k}^2}}{N} \quad (6.16)$$

The force signals were filtered with a fourth order low pass Butterworth filter with 25 Hz cutoff frequency before processing.

Swanson also observed a strong inverse correlation between perceived smoothness and a weighted sum of the discrete Fourier transform components of acceleration (**DFT sum of acceleration**) [23]. The acceleration was computed in post-processing using two iterations of a six-step balanced difference linear estimator,

$$\left(\frac{dx}{dt} \right) = \frac{x_{k+3} - x_{k-3}}{6T} \quad (6.17)$$

$$\left(\frac{dy}{dt} \right) = \frac{y_{k+3} - y_{k-3}}{6T}, \quad (6.18)$$

where T is the sampling period. After each differentiation, the signals were filtered by a fourth order low pass Butterworth filter with cutoff frequency 25 Hz. The following formula is then used to compute the DFT of acceleration:

$$A_n = \sum_{k=0}^{N-1} a_k e^{2\pi jkn/N}, \quad (6.19)$$

where a_k is acceleration magnitude at point k and A_n is the DFT magnitude at frequency window n/NT . The DFT sum of acceleration, h_a , is then given by

$$h_a = \sum_{k=0}^{N/2-1} A_k \frac{k}{NT}. \quad (6.20)$$

This form places a higher weighting on the higher frequency components of the signal.

6.6 Results

Figure 6.12 shows a sample of the data collected for the human subject experiments. In this case the proportional velocity controller with low gain was used. The three performance metrics were computed for each data set. Average numerical results for each human operator are shown in Appendix C. Here the results can be compared between each of the paths, configurations, controllers, and operators. In general, the average path error is greater for line 2 than for line 1.

The goal of these controllers is to minimize all three performance metrics. The performance metrics are summarized in Figures 6.13, 6.14 and 6.15. All trials for each combination of controller and configuration are combined and presented as box and whisker plots. The controller abbreviations used in the figures are defined in Table 6.2. The middle line in each box represents the median of the data. The upper and lower boundaries of the box represent the upper and lower quartiles. The whiskers span the entire range of data excluding outliers. Outliers are defined as points that are a distance of more than 1.5 times the span of the box away from the box boundary.

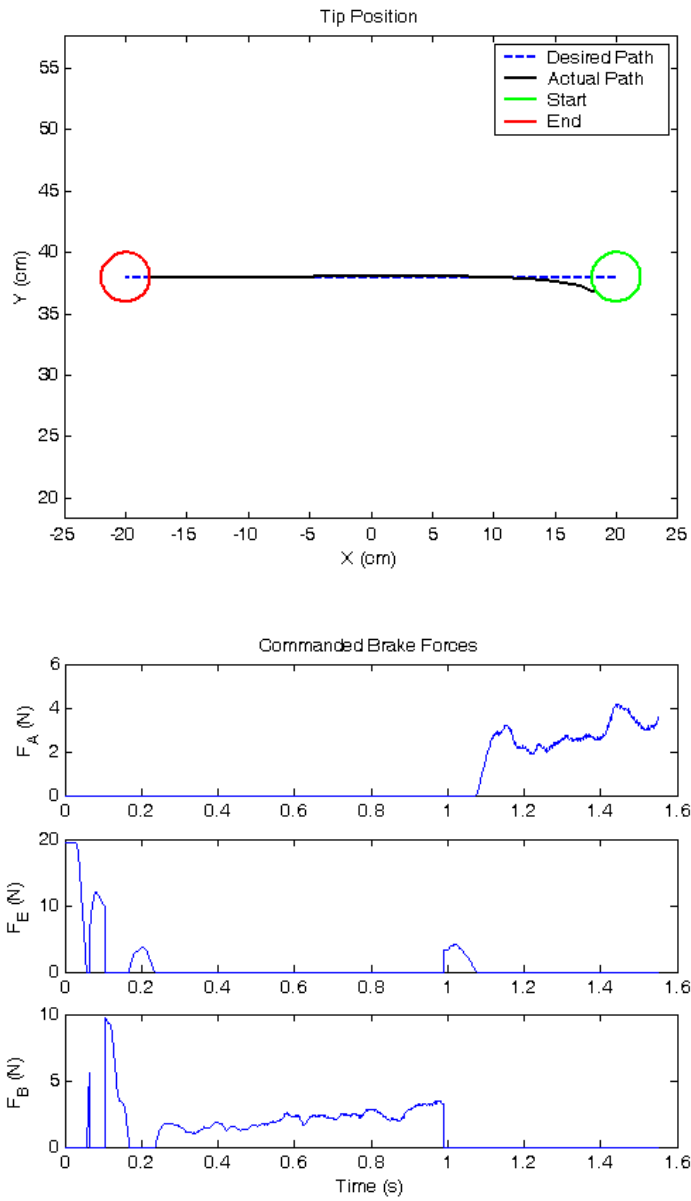


Figure 6.12. Sample of Human Subject Data Using Low Gain Proportional Velocity Control in the 3-Brake Configuration

Table 6.2. Controller Abbreviations

Abbreviation	Controller
N	No Control
S	SDOF Control
G	SDOF Control with Gap
H	Proportional Control (high gain)
L	Proportional Control (low gain)

Figure 6.13 compares the average path error for each combination of controller and configuration. Both controllers reduced path error significantly, regardless of the gain used. However, it is worthwhile to note that the SDOF velocity controller with uncontrolled gap resulted in far greater consistency in accuracy than the other systems.

Figures 6.14 and 6.15 summarize the average force data and DFT sum of acceleration data, respectively. As expected, adding an uncontrolled gap to the SDOF controller increased smoothness and decreased workload by sacrificing a negligible amount of accuracy. Likewise, by lowering the gain of the proportional controller, a significant reduction in workload and increase in smoothness was realized with little change in accuracy. Overall the proportional controller exhibited lower workload and higher levels of smoothness than the SDOF controller. In fact, the low gain proportional controller exhibited similar levels of workload and smoothness to the uncontrolled experiment.

Further conclusions can be made by comparing the results between the two robot configurations. As Figures 6.13, 6.14, and 6.15 indicate, the 4-brake configuration did not offer any measurable performance gains over the 3-brake configuration. Also, the path error for the uncontrolled 4-brake configuration varied over a much wider range than the uncontrolled 3-brake configuration. This suggests that the dynamics of the 3-brake

configuration are such that it is more intuitive for the operator to maneuver accurately than the 4-brake configuration. It should be emphasized that these results are preliminary, and may vary under a different set of testing conditions.

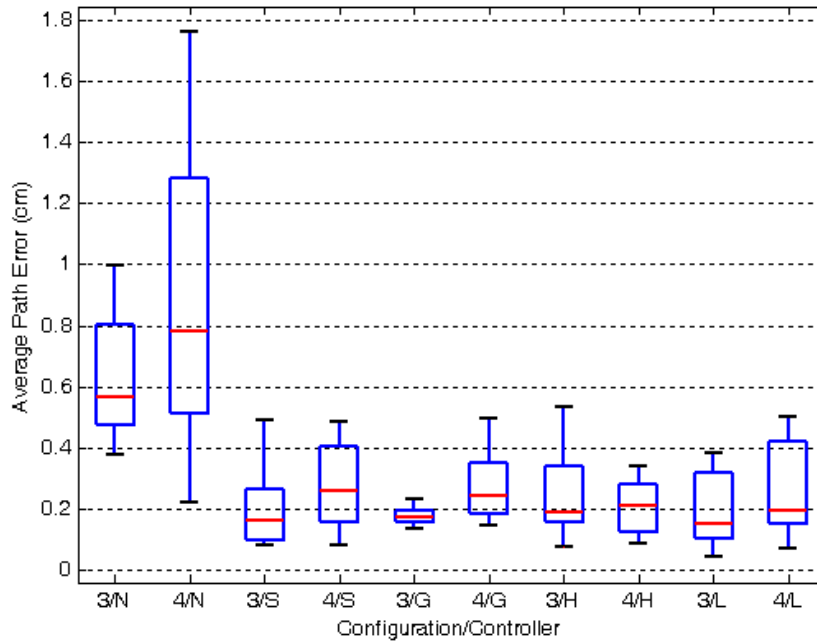


Figure 6.13. Average Path Error by Configuration and Controller

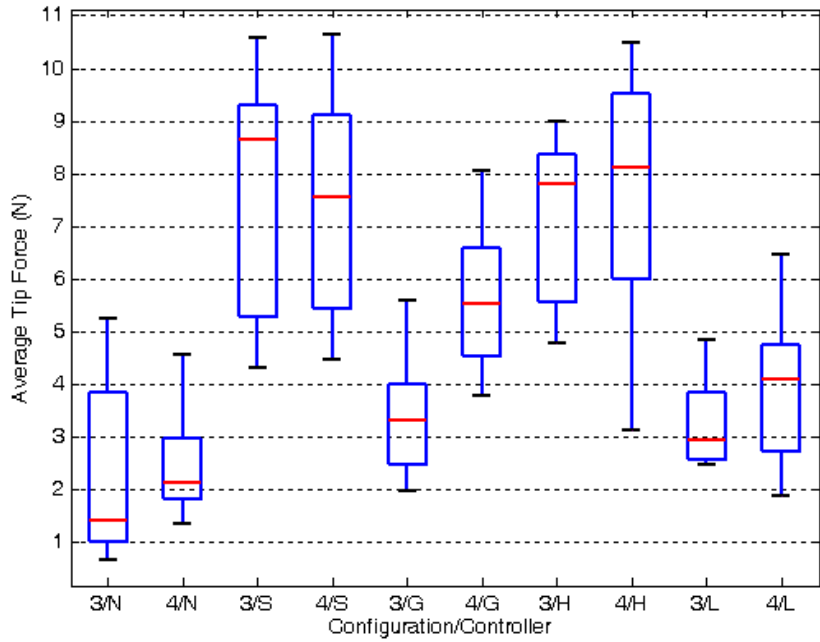


Figure 6.14. Average Tip Force by Configuration and Controller

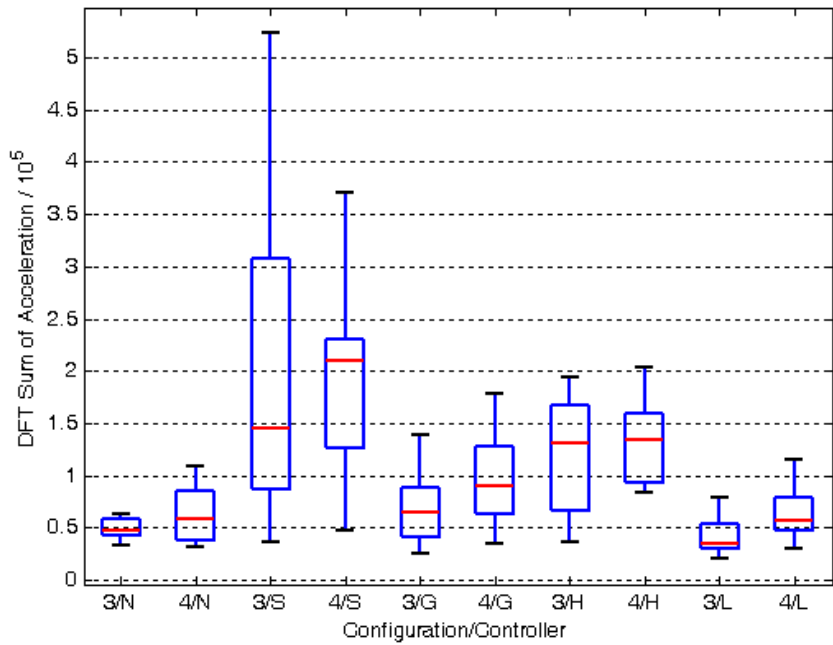


Figure 6.15. DFT Sum of Acceleration by Configuration and Controller

CHAPTER 7

CONCLUSIONS AND FUTURE WORK

This chapter provides a brief summary of the research discussed in this document. It continues by highlighting the major contributions of this work and concludes with some suggestions for future research.

7.1 Conclusions

The objective of this research was to develop an improved passive haptic display using MR fluid brakes as actuators. This goal was accomplished with the completion of four main tasks. First, a model was developed that accurately predicts the behavior of MR fluids in a low-speed braking device. Second, a dissipative passive haptic interface that could effectively utilize this technology was designed and constructed. Third, a robot simulation was developed that incorporated the brake model into the equations of motion of the system. Lastly, two velocity controllers were designed and evaluated in path following exercises involving human subjects.

The modeling technique for the MR fluid brakes was presented in Chapter 3. The model computes the yield stress in terms of the applied current, torque history, and shaft position and velocity. The yield stress is modeled as a first order system with varying gain and time constant. The torque gain is a quadratic function of current, yet an adjustment is made if the shaft is in the backlash region. The time constant is relatively constant, yet was found to increase at very low speeds. The comparison of the brake

model to experimental data indicated that the first order model accurately predicts braking torque for current steps and is satisfactory for other types of input. Additionally, the SDOF control experiments showed that accurate torque output of the MR fluid brakes can be achieved without torque feedback.

Chapter 4 presented four design concepts from which a single design with two possible configurations was chosen. The final design is a five-bar linkage with separate link arrangements corresponding to 3-brake and 4-brake operation. The geometry of the 3-brake configuration was selected such that the arms form a closed parallelogram, similar to the layout of PTER. The 4-brake configuration was selected using an optimization procedure that weighed the size and shape of the workspace and the spacing of local SDOF paths in the workspace. The resulting system features equivalent availability of local SDOF paths or forces to that of PTER. However, the selection of MR fluid brakes as actuators eliminated problems associated with time delays and stiction and resulted in less torque fluctuation.

The robot modeling and simulation procedure was discussed in Chapter 5. The forward and inverse kinematics were computed using geometric relationships. Also, a 4×2 Jacobian is presented that relates the joint torques to tip forces. Lagrange's equation was used to solve for the equations of motion of the system. A set of constraints was added to the system in order to eliminate the nonlinear terms and simplify the equations. Comparisons of the model output to experimental data showed that the robot model is an effective tool for predicting robot motion and evaluating control techniques.

Finally, Chapter 6 presents the control architecture used to implement two velocity controllers for path following control. The desired velocity is determined using a

velocity field that linearly blends velocity toward the desired path. The SDOF controller operates by locking the brake with the local SDOF path pointing in the direction closest to that of the desired velocity. The proportional velocity controller actuates a brake with a corresponding tip force that will reduce the velocity component perpendicular to the desired velocity. Each controller was evaluated in simulation before undergoing preliminary testing with human operators. The testing was used to evaluate the accuracy, smoothness, and workload associated with each controller and configuration. Both controllers offered a similar improvement in accuracy over the uncontrolled case. The main differences were observed in workload and smoothness, where the low gain proportional velocity controller was superior. Also, the results suggest that the 4-brake configuration offers no performance advantages over the 3-brake configuration.

7.2 Contributions

The method used to model the MR fluid brake is the first that is designed specifically for low-speed braking applications. The same procedure could potentially be used to model any MR fluid actuator subjected to low shear rates. Furthermore, it may also be applied to ER fluids since they share many of the same yield characteristics [7].

Computation of the forward and inverse kinematics, the 4×2 Jacobian, and the equations of motion assumed any set of arm lengths and inertial parameters. Therefore the techniques presented in Chapter 5 could be used to model the behavior of any robot with the configuration shown in Figure 5.4, with actuators located at Joints A, B, C, and/or E.

A new method is also presented for selecting the geometry of a dissipative passive haptic display. It allows the designer to visualize the workspace area in terms of the spacing between local SDOF paths or tip forces generated by each brake.

Both velocity controllers presented in Chapter 7 are based on previous work, yet each contributes new functionality. The SDOF controller is capable of highly accurate path following control, yet the rapid switching between brakes introduces vibration. The addition of a gap surrounding the desired path within which no brakes are actuated helped to alleviate this problem with a minimal sacrifice in accuracy. On the other hand, proportional velocity control chooses the appropriate brake to actuate using a matrix of influence coefficients relating the impact of each tip force on actual velocity translated into the desired velocity space. This approach ensures that the optimum brake is chosen rather than previous methods that simply choose the force vector based on location alone. The two control techniques presented in this work could be implemented on any dissipative passive haptic display that has the ability to lock an actuator. Furthermore, they can be used for any desired path as long as the slope of the tangent is known at every point.

Part of the motivation of this research was to compare the performance of two new designs for passive haptic displays. Much of this work was completed based on the assumption that additional actuators would increase the performance of a dissipative passive haptic display, assuming that the local SDOF paths or forces generated by those actuators are evenly spaced. However, as demonstrated in Section 6.6, adding an extra actuator does not necessarily increase the performance of the device. The changes made to accommodate that actuator may affect the dynamics in such a way that no additional

gain is realized. However, it should be emphasized that this conclusion is based on preliminary data. The results might vary for other control techniques and testing conditions.

7.3 Future Work

This project resulted in the successful development of a new dissipative passive haptic display. However, there are still many opportunities for continued research on this particular device and related systems.

There are several modifications that can be made to the mechanical system in order to enhance its performance. First, a modification to the base could be made such that the base joints would be allowed to rotate beyond their current structural limits. This would significantly increase the workspace of the robot. Second, the moving weight of the system could be reduced by milling out the center section of the arms and by reducing the size of the steel collars. With a lower inertia system, the force contribution from each brake will have a greater impact on tip trajectory. Finally, the MR fluid brakes could be replaced with brakes that do not have backlash. Personnel at Lord Corporation claim that MR fluid brakes without backlash will be available in the near future. There is no doubt that the backlash in the brakes has a negative impact on path following performance. For instance, in full lockdown, the tip of the robot is free to move within an area of several square centimeters. Therefore, new brakes should yield a substantial increase in accuracy.

Two path following controllers were tested in this research. There exists the opportunity for additional controllers to be tested on the new system, including a form of

Swanson's optimal control [23]. Furthermore, the device has yet to be tested in obstacle avoidance tasks. Either of the two velocity controllers discussed in this work could be modified for this application by treating the obstacle boundary as the desired path, yet control action would only be taken on the obstacle side of the path. Development of new control techniques will likely be followed by a more comprehensive investigation of performance using human subject testing. There is also the opportunity for a formal comparison of the performance of the new robot to that of PTER.

The graphical method for the design of a dissipative passive haptic display presented in this work displays the workspace in terms of the spacing of force vectors at the tip resulting from joint torques. As evidenced by the performance comparison of the 3-brake and 4-brake configurations, this design tool may not be the best method. Future methods may include using a different measure of the spacing of local SDOF paths. Furthermore, a method could be developed that takes into account the dynamics of the device.

The next step for dissipative passive haptic displays is to increase the number of degrees of freedom. This robot was designed in such a way that it could easily be converted into a 3-DOF spatial system. One option involves modifying the base and orienting the robot such that the y-direction becomes the z-direction and using an additional actuator to control rotation in the z-direction. A more challenging project would involve a complete redesign where multiple actuators control each degree-of-freedom.

Another suggestion for future research is the development of a hybrid steerable/dissipative passive haptic display. This would effectively combine the superior path following performance of steerable systems with the superior force reflection

capability of dissipative systems. A system such as this would be difficult to implement on the robot discussed in this work. However, PTER could be modified by replacing the coupling actuators with a clutch and CVT. This would allow variable coupling of the links and retain the ability to brake the links independently.

APPENDIX A

DERIVATION OF EQUATIONS OF MOTION

The following is a complete derivation of the equations of motion for the robot. All variables are defined in Chapter 5.

General Form of Dynamic Equation:

$$\mathbf{Q} = \mathbf{M}(\mathbf{q})\ddot{\mathbf{q}} + \mathbf{V}(\mathbf{q}, \dot{\mathbf{q}}) + \mathbf{G}(\mathbf{q}) \quad (\text{A.1})$$

Lagrange's Equation:

$$Q_j + \sum_{i=1}^k \lambda_j \frac{\partial C_i}{\partial q_j} = \frac{d}{dt} \left(\frac{\partial L}{\partial \dot{q}_j} \right) - \frac{\partial L}{\partial q_j} \quad j = 1 \text{ to } n \quad (\text{A.2})$$

Simplified Robot Model:

$$\mathbf{M}(\mathbf{q})\ddot{\mathbf{q}} = \mathbf{Q} + \mathbf{A}^T \boldsymbol{\lambda} \quad (\text{A.3})$$

$$\begin{bmatrix} \mathbf{M} & -\mathbf{A}^T \\ -\mathbf{A} & 0 \end{bmatrix} \begin{bmatrix} \ddot{\mathbf{q}} \\ \boldsymbol{\lambda} \end{bmatrix} = \begin{bmatrix} \mathbf{Q} \\ \dot{\mathbf{A}}\dot{\mathbf{q}} \end{bmatrix} \quad (\text{A.4})$$

Generalized Coordinates:

$$\mathbf{q} = [x \quad y \quad \theta_A \quad \theta_E \quad x_{ED} \quad y_{ED} \quad \theta_B \quad \theta_C \quad x_{CD} \quad y_{CD}]^T \quad (\text{A.5})$$

Generalized Forces:

$$\mathbf{Q} = [F_x \quad F_y \quad \tau_A \quad \tau_E \quad 0 \quad 0 \quad \tau_B \quad \tau_C \quad 0 \quad 0]^T \quad (\text{A.6})$$

Kinetic Energy:

$$T_{AE} = \frac{1}{2} I_{AE} \dot{\theta}_A^2 + \frac{1}{2} m_{AE} l_{AE}^2 \dot{\theta}_A^2 \quad (\text{A.7})$$

$$T_{BC} = \frac{1}{2} I_{BC} \dot{\theta}_B^2 + \frac{1}{2} m_{BC} l_{BC}^2 \dot{\theta}_B^2 \quad (\text{A.8})$$

$$T_{ED} = \frac{1}{2} I_{ED} (\dot{\theta}_E + \dot{\theta}_A)^2 + \frac{1}{2} m_{ED} (\dot{x}_{ED}^2 + \dot{y}_{ED}^2) \quad (\text{A.9})$$

$$T_{CD} = \frac{1}{2} I_{CD} (\dot{\theta}_C + \dot{\theta}_B)^2 + \frac{1}{2} m_{CD} (\dot{x}_{CD}^2 + \dot{y}_{CD}^2) \quad (\text{A.10})$$

$$T_D = \frac{1}{2} m_D (\dot{x}^2 + \dot{y}^2) \quad (\text{A.11})$$

Derivatives:

$$\frac{d}{dt} \left(\frac{\partial T}{\partial \dot{x}} \right) = m_D \ddot{x} \quad (\text{A.12})$$

$$\frac{d}{dt} \left(\frac{\partial T}{\partial \dot{y}} \right) = m_D \ddot{y} \quad (\text{A.13})$$

$$\frac{d}{dt} \left(\frac{\partial T}{\partial \dot{\theta}_A} \right) = (I_{AE} + m_{AE} l_{AE}^2 + I_{ED}) \ddot{\theta}_A + I_{ED} \ddot{\theta}_E \quad (\text{A.14})$$

$$\frac{d}{dt} \left(\frac{\partial T}{\partial \dot{\theta}_E} \right) = I_{ED} \ddot{\theta}_E + I_{ED} \ddot{\theta}_A \quad (\text{A.15})$$

$$\frac{d}{dt} \left(\frac{\partial T}{\partial \dot{x}_{ED}} \right) = m_{ED} \ddot{x}_{ED} \quad (\text{A.16})$$

$$\frac{d}{dt} \left(\frac{\partial T}{\partial \dot{y}_{ED}} \right) = m_{ED} \ddot{y}_{ED} \quad (\text{A.17})$$

$$\frac{d}{dt} \left(\frac{\partial T}{\partial \dot{\theta}_B} \right) = (I_{BC} + m_{BC} l_{BC}^2 + I_{CD}) \ddot{\theta}_B + I_{CD} \ddot{\theta}_C \quad (\text{A.18})$$

$$\frac{d}{dt} \left(\frac{\partial T}{\partial \dot{\theta}_C} \right) = I_{CD} \ddot{\theta}_C + I_{CD} \ddot{\theta}_B \quad (\text{A.19})$$

$$\frac{d}{dt} \left(\frac{\partial T}{\partial \dot{x}_{CD}} \right) = m_{CD} \ddot{x}_{CD} \quad (\text{A.20})$$

$$\frac{d}{dt} \left(\frac{\partial T}{\partial \dot{y}_{CD}} \right) = m_{CD} \ddot{y}_{CD} \quad (\text{A.21})$$

Mass Matrix:

$$\mathbf{M} = \begin{bmatrix} \mathbf{M}_D & 0 & 0 & 0 & 0 \\ 0 & \mathbf{M}_{AE} & 0 & 0 & 0 \\ 0 & 0 & \mathbf{M}_{ED} & 0 & 0 \\ 0 & 0 & 0 & \mathbf{M}_{BC} & 0 \\ 0 & 0 & 0 & 0 & \mathbf{M}_{CD} \end{bmatrix} \quad (\text{A.22})$$

$$\mathbf{M}_D = \begin{bmatrix} m_D & 0 \\ 0 & m_D \end{bmatrix} \quad (\text{A.23})$$

$$\mathbf{M}_{AE} = \begin{bmatrix} I_{AE} + m_{AE}l_{AE}^2 + I_{ED} & I_{ED} \\ I_{ED} & I_{ED} \end{bmatrix} \quad (\text{A.24})$$

$$\mathbf{M}_{ED} = \begin{bmatrix} m_{ED} & 0 \\ 0 & m_{ED} \end{bmatrix} \quad (\text{A.25})$$

$$\mathbf{M}_{BC} = \begin{bmatrix} I_{BC} + m_{BC}l_{BC}^2 + I_{CD} & I_{CD} \\ I_{CD} & I_{CD} \end{bmatrix} \quad (\text{A.26})$$

$$\mathbf{M}_{CD} = \begin{bmatrix} m_{CD} & 0 \\ 0 & m_{CD} \end{bmatrix} \quad (\text{A.27})$$

Constraints:

$$C_1 = L_{AE} \cos \theta_A + L_{ED} \cos(\theta_A + \theta_E) - \frac{L_{AB}}{2} - x = 0 \quad (\text{A.28})$$

$$C_2 = L_{AE} \sin \theta_A + L_{ED} \sin(\theta_A + \theta_E) - y = 0 \quad (\text{A.29})$$

$$C_3 = L_{BC} \cos \theta_B + L_{CD} \cos(\theta_B + \theta_C) + \frac{L_{AB}}{2} - x = 0 \quad (\text{A.30})$$

$$C_4 = L_{BC} \sin \theta_B + L_{CD} \sin(\theta_B + \theta_C) - y = 0 \quad (\text{A.31})$$

$$C_5 = L_{AE} \cos \theta_A + l_{ED} \cos(\theta_A + \theta_E) - \frac{L_{AB}}{2} - x_{ED} = 0 \quad (\text{A.32})$$

$$C_6 = L_{AE} \sin \theta_A + l_{ED} \sin(\theta_A + \theta_E) - y_{ED} = 0 \quad (\text{A.33})$$

$$C_7 = L_{BC} \cos \theta_B + l_{CD} \cos(\theta_B + \theta_C) + \frac{L_{AB}}{2} - x_{CD} = 0 \quad (\text{A.34})$$

$$C_8 = L_{BC} \sin \theta_B + l_{CD} \sin(\theta_B + \theta_C) - y_{CD} = 0 \quad (\text{A.35})$$

$$\mathbf{A} = \begin{bmatrix} -\mathbf{I} & \mathbf{A}_{xy1} & 0 & 0 & 0 \\ -\mathbf{I} & 0 & 0 & \mathbf{A}_{xy2} & 0 \\ 0 & \mathbf{A}_{ED} & -\mathbf{I} & 0 & 0 \\ 0 & 0 & 0 & \mathbf{A}_{CD} & -\mathbf{I} \end{bmatrix} \quad (\text{A.36})$$

$$\mathbf{I} = \begin{bmatrix} 1 & 0 \\ 0 & 1 \end{bmatrix} \quad (\text{A.37})$$

$$\mathbf{A}_{xy1} = \begin{bmatrix} -L_{AE} \sin \theta_A - L_{ED} \sin(\theta_A + \theta_E) & -L_{ED} \sin(\theta_A + \theta_E) \\ L_{AE} \cos \theta_A + L_{ED} \cos(\theta_A + \theta_E) & L_{ED} \cos(\theta_A + \theta_E) \end{bmatrix} \quad (\text{A.38})$$

$$\mathbf{A}_{xy2} = \begin{bmatrix} -L_{BC} \sin \theta_B - L_{CD} \sin(\theta_B + \theta_C) & -L_{CD} \sin(\theta_B + \theta_C) \\ L_{BC} \cos \theta_B + L_{CD} \cos(\theta_B + \theta_C) & L_{CD} \cos(\theta_B + \theta_C) \end{bmatrix} \quad (\text{A.39})$$

$$\mathbf{A}_{ED} = \begin{bmatrix} -L_{AE} \sin \theta_A - l_{ED} \sin(\theta_A + \theta_E) & -l_{ED} \sin(\theta_A + \theta_E) \\ L_{AE} \cos \theta_A + l_{ED} \cos(\theta_A + \theta_E) & l_{ED} \cos(\theta_A + \theta_E) \end{bmatrix} \quad (\text{A.40})$$

$$\mathbf{A}_{CD} = \begin{bmatrix} -L_{BC} \sin \theta_B - l_{CD} \sin(\theta_B + \theta_C) & -l_{CD} \sin(\theta_B + \theta_C) \\ L_{BC} \cos \theta_B + l_{CD} \cos(\theta_B + \theta_C) & l_{CD} \cos(\theta_B + \theta_C) \end{bmatrix} \quad (\text{A.41})$$

$$\dot{\mathbf{A}} = \begin{bmatrix} 0 & \dot{\mathbf{A}}_{xy1} & 0 & 0 & 0 \\ 0 & 0 & 0 & \dot{\mathbf{A}}_{xy2} & 0 \\ 0 & \dot{\mathbf{A}}_{ED} & 0 & 0 & 0 \\ 0 & 0 & 0 & \dot{\mathbf{A}}_{CD} & 0 \end{bmatrix} \quad (\text{A.42})$$

$$\dot{\mathbf{A}}_{xy1} = \begin{bmatrix} -L_{AE} \dot{\theta}_A \cos \theta_A - L_{ED} (\dot{\theta}_A + \dot{\theta}_E) \cos(\theta_A + \theta_E) & -L_{ED} (\dot{\theta}_A + \dot{\theta}_E) \cos(\theta_A + \theta_E) \\ -L_{AE} \dot{\theta}_A \sin \theta_A - L_{ED} (\dot{\theta}_A + \dot{\theta}_E) \sin(\theta_A + \theta_E) & -L_{ED} (\dot{\theta}_A + \dot{\theta}_E) \sin(\theta_A + \theta_E) \end{bmatrix} \quad (\text{A.43})$$

$$\dot{\mathbf{A}}_{xy2} = \begin{bmatrix} -L_{BC} \dot{\theta}_B \cos \theta_B - L_{CD} (\dot{\theta}_B + \dot{\theta}_C) \cos(\theta_B + \theta_C) & -L_{CD} (\dot{\theta}_B + \dot{\theta}_C) \cos(\theta_B + \theta_C) \\ -L_{BC} \dot{\theta}_B \sin \theta_B - L_{CD} (\dot{\theta}_B + \dot{\theta}_C) \sin(\theta_B + \theta_C) & -L_{CD} (\dot{\theta}_B + \dot{\theta}_C) \sin(\theta_B + \theta_C) \end{bmatrix} \quad (\text{A.44})$$

$$\dot{\mathbf{A}}_{ED} = \begin{bmatrix} -L_{AE}\dot{\theta}_A \cos\theta_A - l_{ED}(\dot{\theta}_A + \dot{\theta}_E)\cos(\theta_A + \theta_E) & -l_{ED}(\dot{\theta}_A + \dot{\theta}_E)\cos(\theta_A + \theta_E) \\ -L_{AE}\dot{\theta}_A \sin\theta_A - l_{ED}(\dot{\theta}_A + \dot{\theta}_E)\sin(\theta_A + \theta_E) & -l_{ED}(\dot{\theta}_A + \dot{\theta}_E)\sin(\theta_A + \theta_E) \end{bmatrix} \quad (\text{A.45})$$

$$\dot{\mathbf{A}}_{CD} = \begin{bmatrix} -L_{BC}\dot{\theta}_B \cos\theta_B - l_{CD}(\dot{\theta}_B + \dot{\theta}_C)\cos(\theta_B + \theta_C) & -l_{CD}(\dot{\theta}_B + \dot{\theta}_C)\cos(\theta_B + \theta_C) \\ -L_{BC}\dot{\theta}_B \sin\theta_B - l_{CD}(\dot{\theta}_B + \dot{\theta}_C)\sin(\theta_B + \theta_C) & -l_{CD}(\dot{\theta}_B + \dot{\theta}_C)\sin(\theta_B + \theta_C) \end{bmatrix} \quad (\text{A.46})$$

APPENDIX B

ROBOT SIMULATION VERIFICATION RESULTS

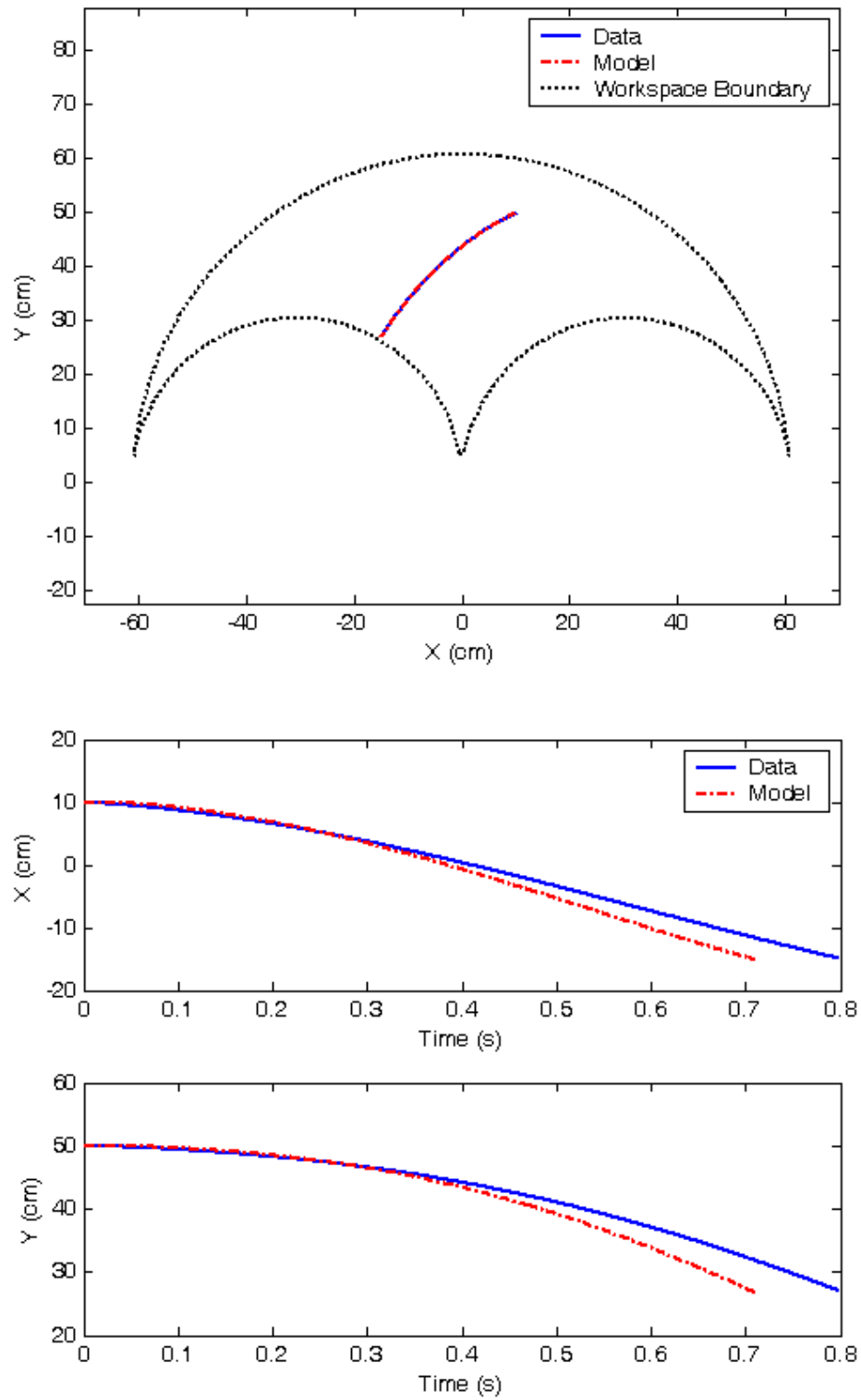


Figure B.1. 3-Brake Configuration Free Motion

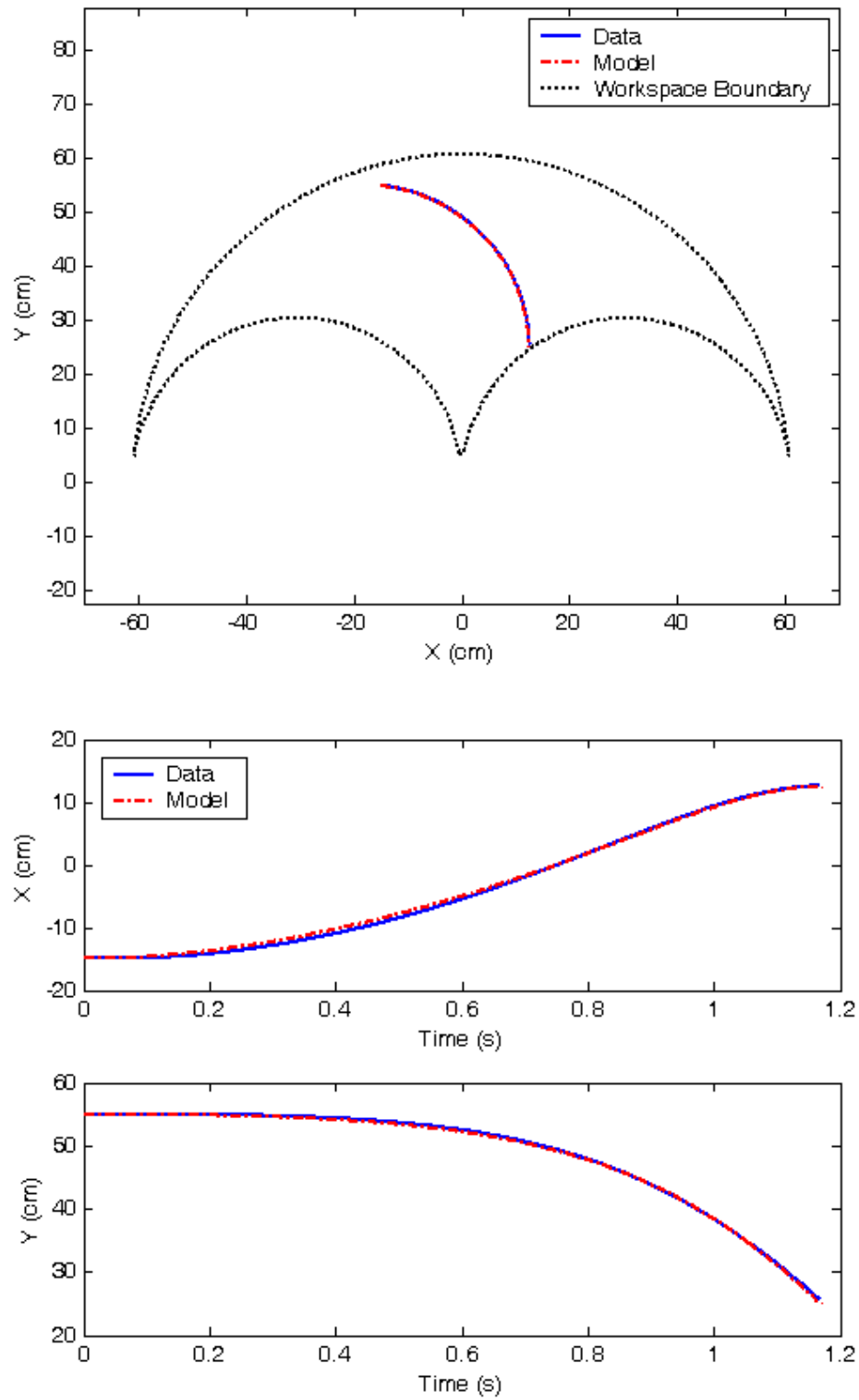


Figure B.2. 3-Brake Configuration with Brake A Locked

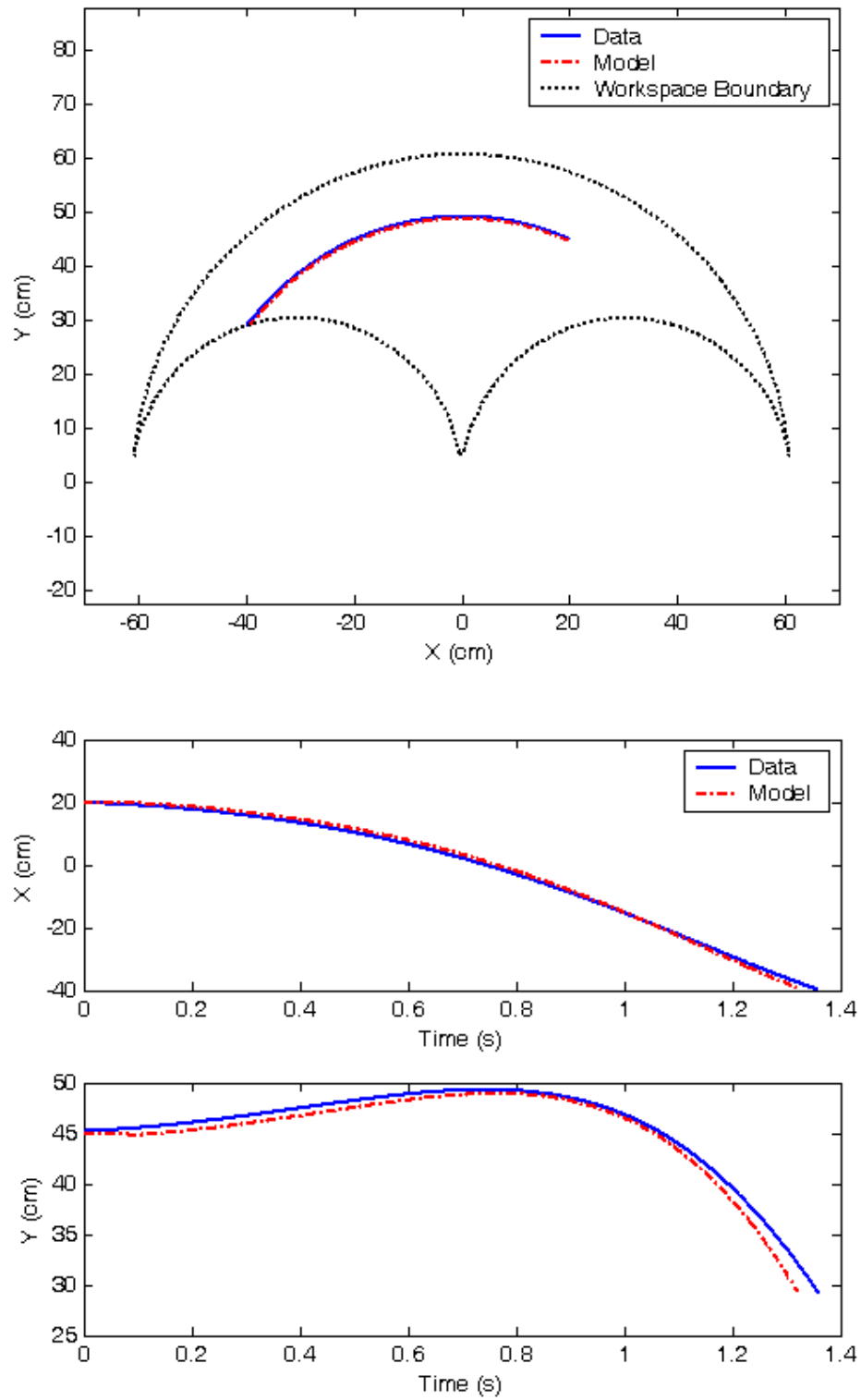


Figure B.3. 3-Brake Configuration with Brake E Locked

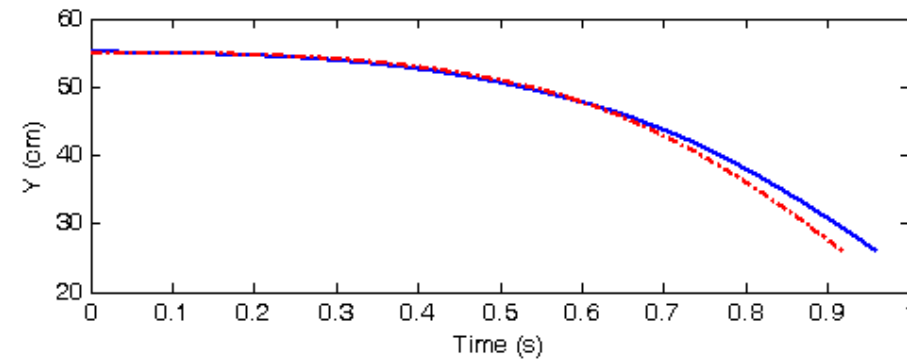
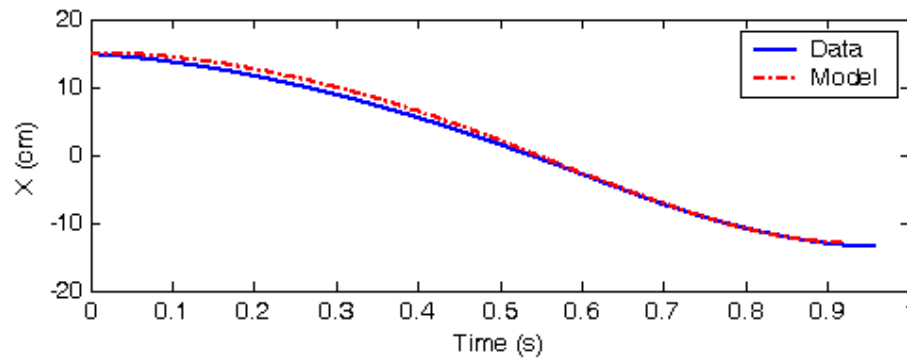
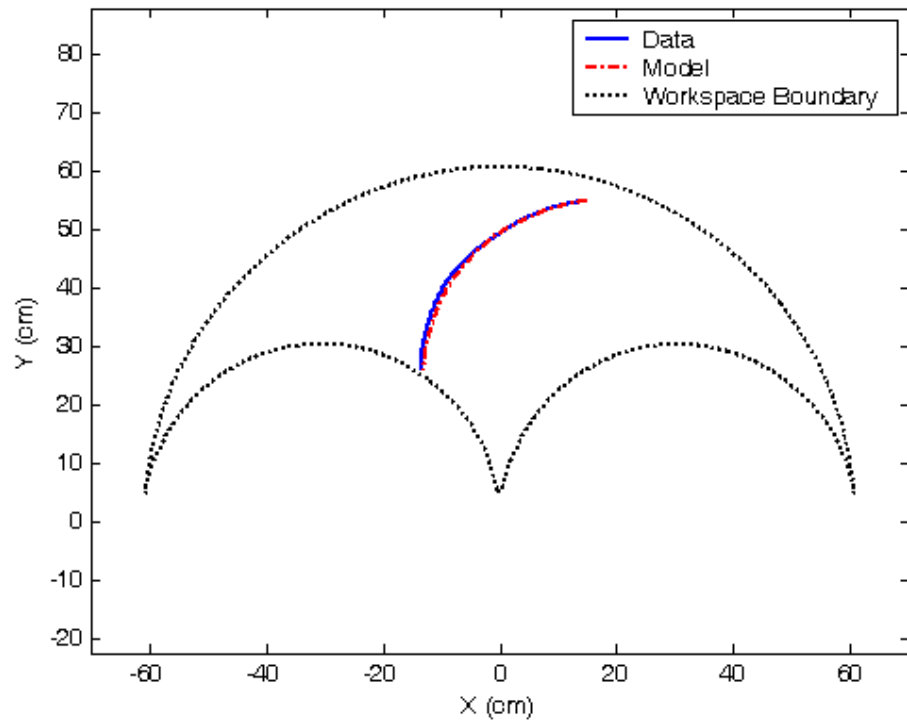


Figure B.4. 3-Brake Configuration with Brake B Locked

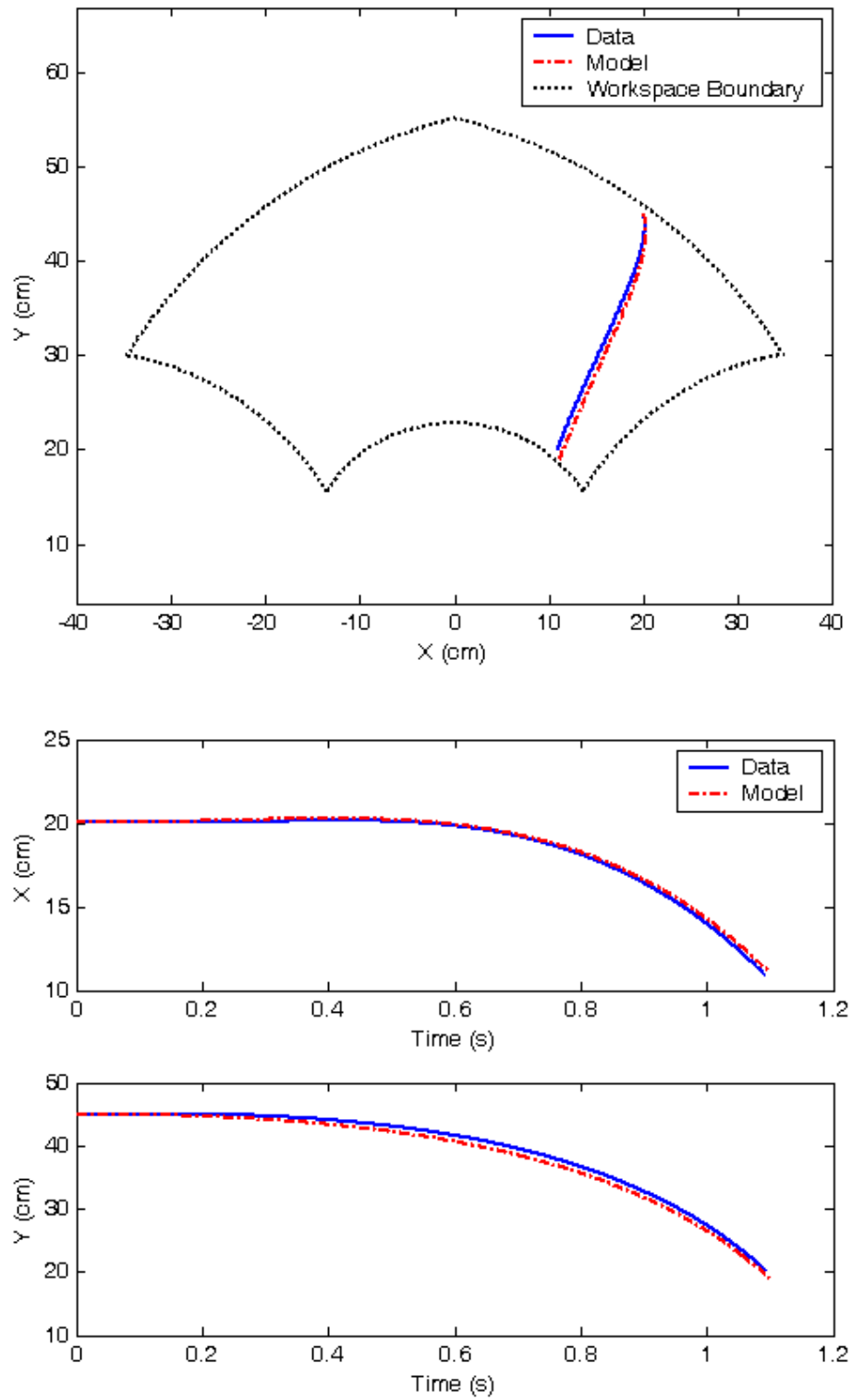


Figure B.5. 4-Brake Configuration Free Motion

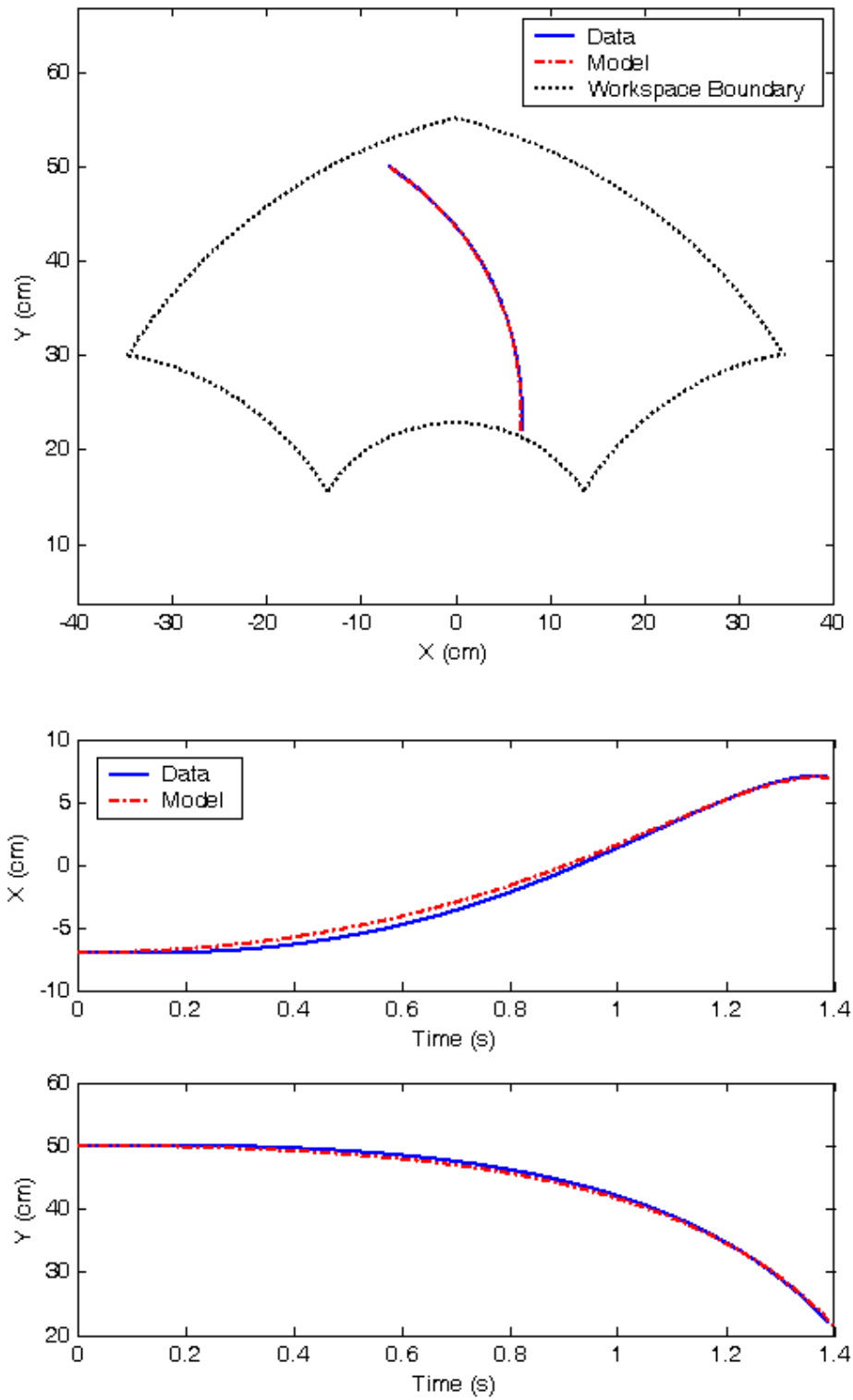


Figure B.6. 4-Brake Configuration with Brake A Locked

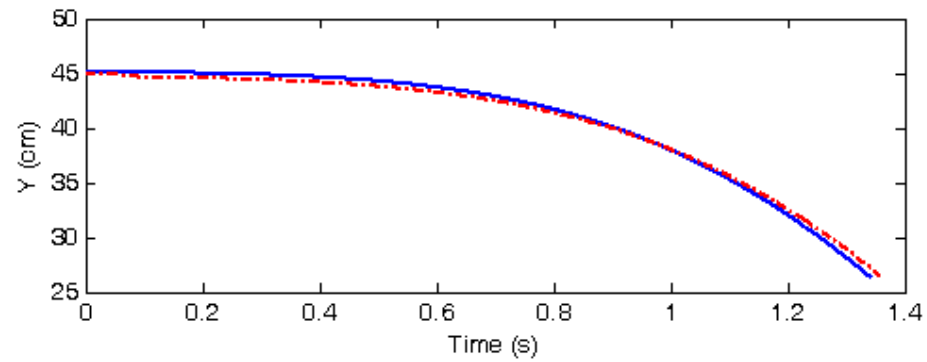
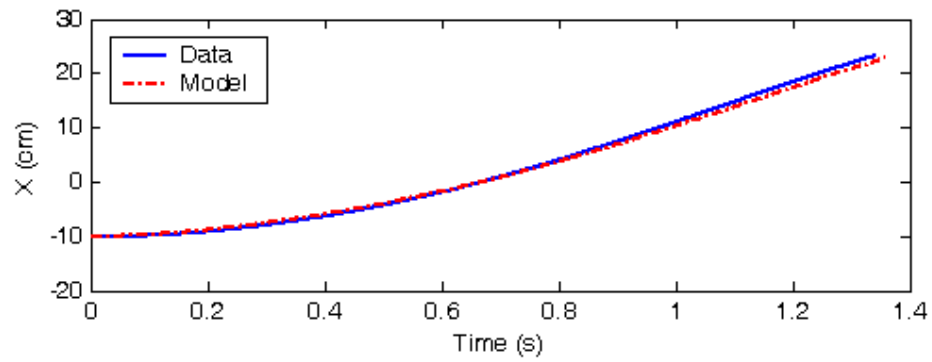
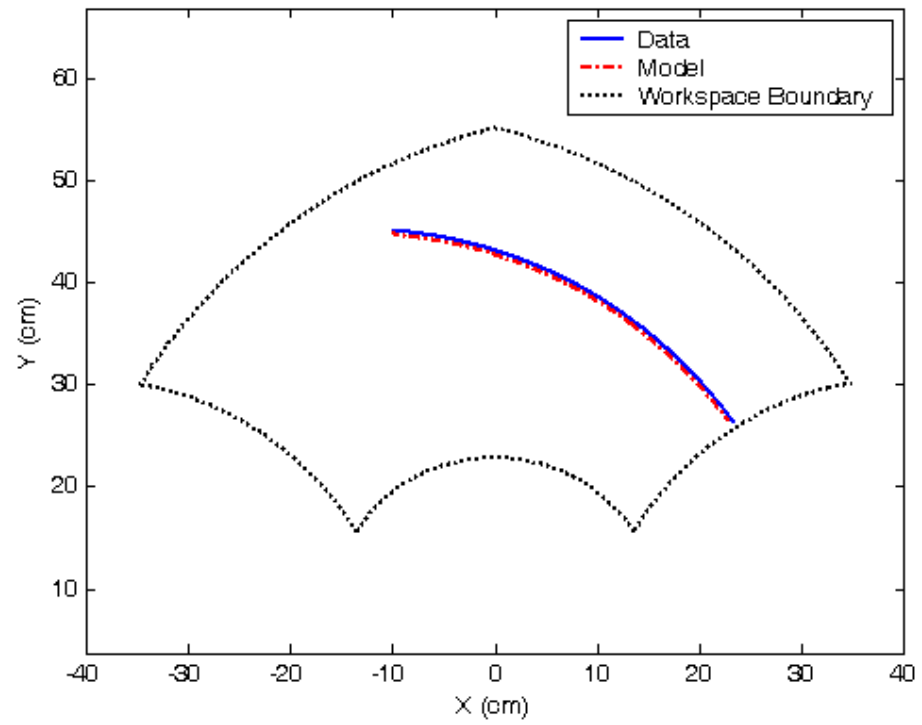


Figure B.7. 4-Brake Configuration with Brake E Locked

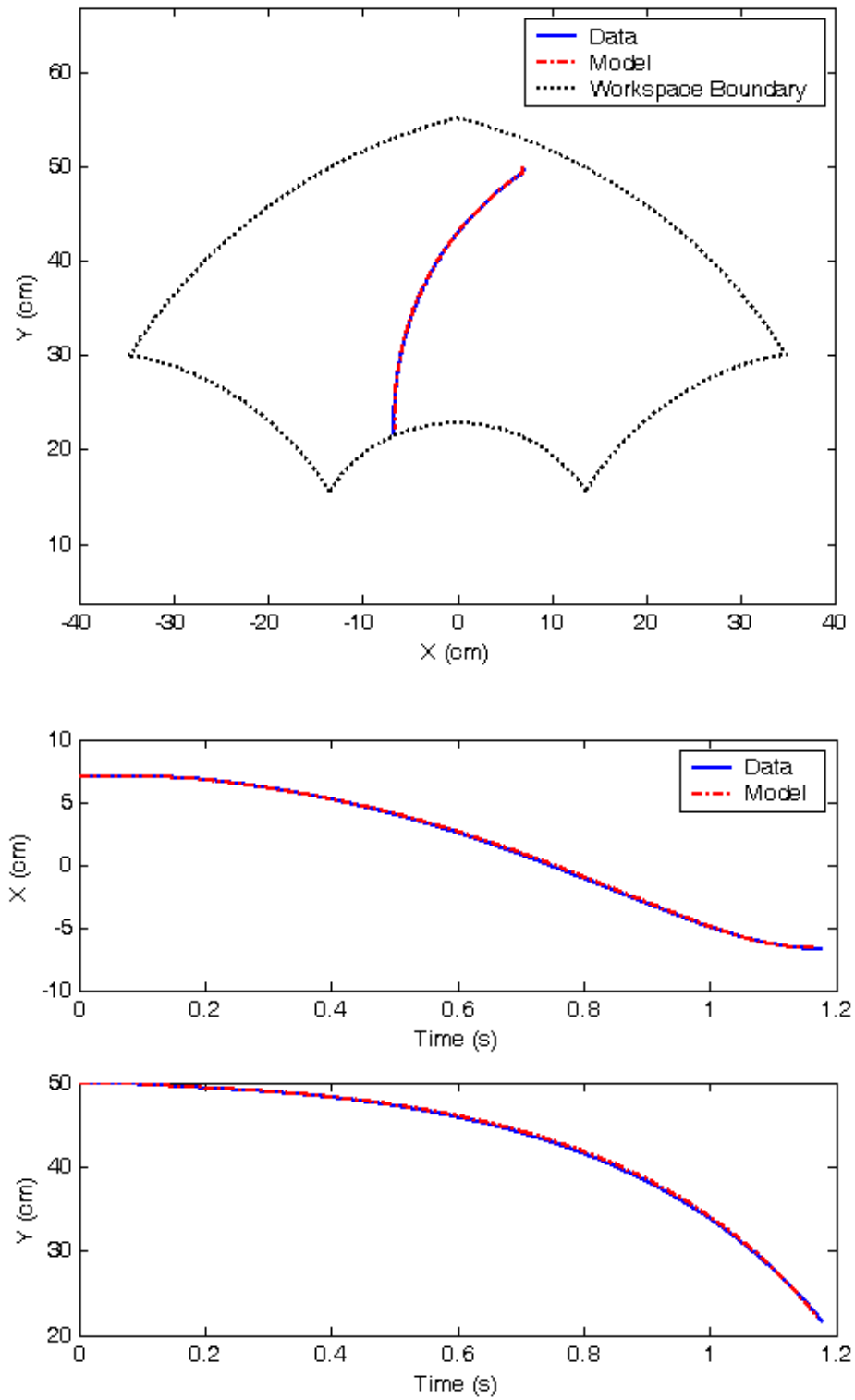


Figure B.8. 4-Brake Configuration with Brake B Locked

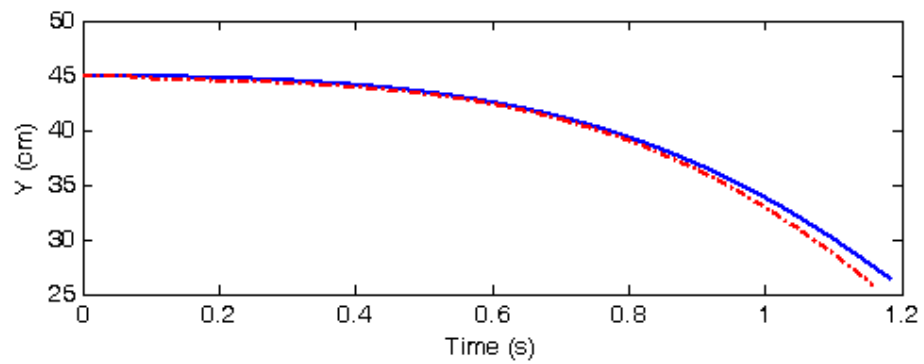
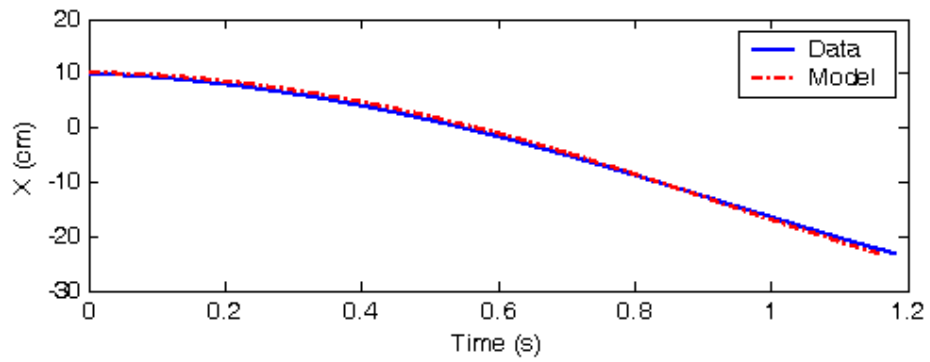
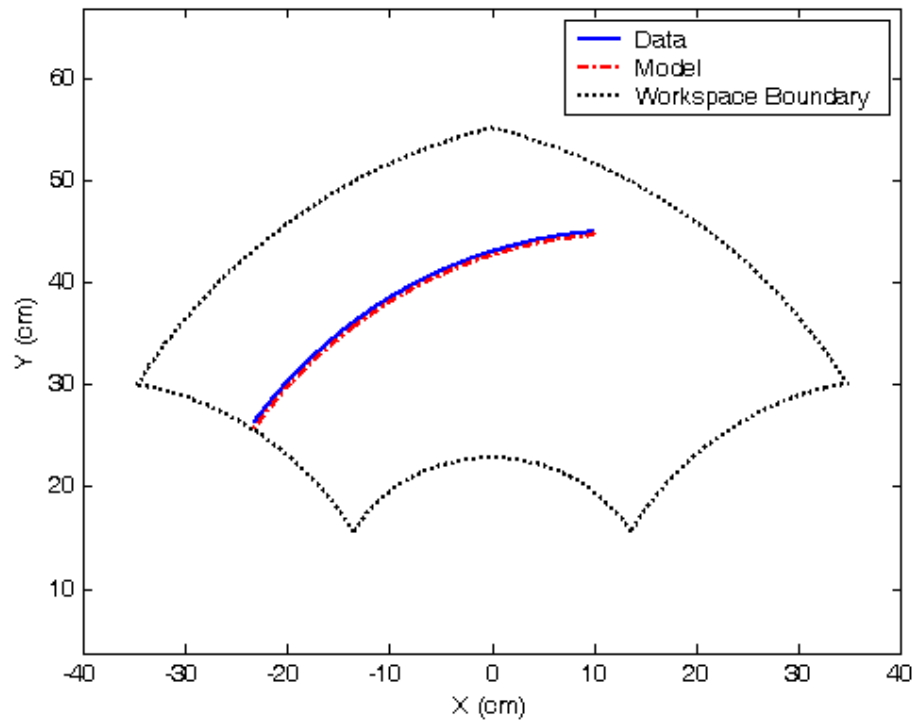


Figure B.9. 4-Brake Configuration with Brake C Locked

APPENDIX C

RESULTS FROM HUMAN OPERATOR EXPERIMENTS

Table C.1. Average Performance Metrics for Human Operator 1 in 3-Brake Configuration

Controller	Avg Path Error (cm)		Avg Tip Force (N)		DFT Sum of Acc / 10 ⁵	
	Line 1	Line 2	Line 1	Line 2	Line 1	Line 2
No Control	0.568	1.674*	4.47	4.36*	0.880	0.569*
Controlled Gap SDOF	0.156	0.308	7.57	9.90	2.161	0.909
Free Gap SDOF	0.193	0.179	5.41	2.83	0.715	0.496
Proportional (high gain)	0.309	0.222	7.97	8.69	1.462	0.533
Proportional (low gain)	0.219	0.162	4.09	3.37	0.593	0.351

*2 data sets missing

Table C.2. Average Performance Metrics for Human Operator 2 in 3-Brake Configuration

Controller	Avg Path Error (cm)		Avg Tip Force (N)		DFT Sum of Acc / 10 ⁵	
	Line 1	Line 2	Line 1	Line 2	Line 1	Line 2
No Control	--**	0.575	--**	0.75	--**	0.404
Controlled Gap SDOF	0.151	0.088	5.35	9.29	2.780	0.855
Free Gap SDOF	0.181	0.184	3.45	2.31	1.007	0.442
Proportional (high gain)	0.131	0.215	5.51	7.95	1.701	0.673
Proportional (low gain)	0.073	0.192	2.86	2.57	0.267	0.279

** 3 data sets missing

Table C.3. Average Performance Metrics for Human Operator 3 in 3-Brake Configuration

Controller	Avg Path Error (cm)		Avg Tip Force (N)		DFT Sum of Acc / 10 ⁵	
	Line 1	Line 2	Line 1	Line 2	Line 1	Line 2
No Control	0.599	0.787	1.51	1.36	0.547	0.475
Controlled Gap SDOF	0.164	0.280	4.99	9.36	3.579	3.058
Free Gap SDOF	0.182	0.256	3.67	3.15	0.771	0.549
Proportional (high gain)	0.235	0.312	5.27	8.16	4.360	1.218
Proportional (low gain)	0.120	0.332	2.65	3.72	0.387	0.596

Table C.4. Average Performance Metrics for Human Operator 1 in 4-Brake Configuration

Controller	Avg Path Error (cm)		Avg Tip Force (N)		DFT Sum of Acc / 10 ⁵	
	Line 1	Line 2	Line 1	Line 2	Line 1	Line 2
No Control	0.705	0.657	5.40	2.93	0.545	0.431
Controlled Gap SDOF	0.174	0.390	6.69	9.28	1.330	1.788
Free Gap SDOF	0.225	0.273	5.91	5.37	0.861	0.696
Proportional (high gain)	0.135	0.200	6.66	9.69	1.339	1.235
Proportional (low gain)	0.255	0.285	4.95	5.22	0.584	0.470

Table C.5. Average Performance Metrics for Human Operator 2 in 4-Brake Configuration

Controller	Avg Path Error (cm)		Avg Tip Force (N)		DFT Sum of Acc / 10 ⁵	
	Line 1	Line 2	Line 1	Line 2	Line 1	Line 2
No Control	0.582	0.558	1.96	1.95	0.542	0.445
Controlled Gap SDOF	0.175	0.325	5.29	8.94	2.095	1.805
Free Gap SDOF	0.192	0.223	4.40	7.69	0.551	1.337
Proportional (high gain)	0.179	0.163	6.34	8.73	1.510	0.905
Proportional (low gain)	0.101	0.157	3.90	4.91	0.520	0.510

Table C.6. Average Performance Metrics for Human Operator 3 in 4-Brake Configuration

Controller	Avg Path Error (cm)		Avg Tip Force (N)		DFT Sum of Acc / 10 ⁵	
	Line 1	Line 2	Line 1	Line 2	Line 1	Line 2
No Control	1.312	1.517	1.50	2.38	0.871	0.811
Controlled Gap SDOF	0.146	0.374	5.11	9.56	1.790	3.118
Free Gap SDOF	0.281	0.472	4.80	5.34	0.965	1.374
Proportional (high gain)	0.598	0.258	3.79	9.98	1.482	2.159
Proportional (low gain)	0.453	0.606	2.64	2.62	0.826	0.752

REFERENCES

- [1] Chan, Vincent K., *Singularity Analysis and Redundant Actuation of Parallel Manipulators*, Master's thesis, Georgia Institute of Technology, March 2001.
- [2] Charles, Robert A., *The Development of the Passive Trajectory Enhancing Robot*, Master's thesis, Georgia Institute of Technology, June 1994.
- [3] Davies, B, "A review of robotics in surgery", *Proceedings of the Institution of Mechanical Engineers, Part H, Journal of Engineering in Medicine*, Vol. 214, Issue 1, 2000.
- [4] Davis, Hurley T., *An Investigation of Passive Actuation for Trajectory Control*, Master's thesis, Georgia Institute of Technology, June 1996.
- [5] Elhajj, Imad, Ning Xi, Wai K. Fung, Yun H. Liu, Wen J. Li, Tomoyuki Kaga, and Toshio Fakuda, "Haptic information in Internet-Based Teleoperation," *IEEE/ASME Transactions on Mechatronics*, Vol. 6, No. 3, September 2001.
- [6] Gomes, Mario W., *An Examination of Control Algorithms for a Dissipative Passive Haptic Interface*, Master's thesis, Georgia Institute of Technology, March 1997.
- [7] Kamath, G. M., and N. M. Wereley, "Nonlinear visco-elastic plastic mechanisms-based model of an electrorheological damper, *Journal of Guidance, Control, and Dynamics*, Vol. 20, No. 6, November-December 1997.
- [8] Kordonski, W., S. Gorodkin, and N. Zhuravski, "Static yield stresses in magnetorheological fluid," *International Journal of Modern Physics B*, Vol. 15, Nos. 6 and 7, World Scientific Publishing Company, New Jersey, 2001.
- [9] Koyanagi, Ken'ichi, Takafumi Inoue, and Junji Furusho, "Rehabilitation application of force display system using ER fluid," *International Conference on Motion and Vibration Control*, (Saitama, Japan) August 2002.
- [10] Li, W. H., G. Chen, S. H. Yeo, and H. Du, "Temperature dependence of MR fluids," *International Journal of Modern Physics B*, Vol. 16, Nos. 17 and 18, World Scientific Publishing Company, New Jersey, 2002.
- [11] Lord Corporation website, <http://www.mrfluid.com>, Accessed October 26, 2003.
- [12] Lord Materials Division, "What is the difference between MR and ER fluid?" *Presentation*, May 2002.

- [13] Loureiro, Rui, William Harwin, and Lawrence Normie, "An investigation of the properties of magnetorheological fluids for assisting upper limb movement disorders on adl," *International Journal of Human-Friendly Welfare Robotic Systems*, Vol. 4, No. 1, April 2003.
- [14] Madhavan, V., G.M. Kamath, and N. M. Wereley, "Hysteresis modeling of semi-active magnetorheological helicopter dampers," *Journal of Intelligent Material Systems and Structures*, Vol. 10, No. 8, August 1999.
- [15] Mammar, S., J. Sainte-Marie, and S. Glaser, "On the use of steer-by-wire systems in lateral driving assistance applications," *IEEE International Workshop on Robot and Human Interactive Communication*, 2001.
- [16] Moore, Carl A., Michael A. Peshkin, and J. Edward Colgate, "Design of a 3R cobot using continuously variable transmissions," *Proceedings of the IEEE International Conference on Robotics and Automation*, (Detroit, Michigan), May 1999.
- [17] Munir, S., L. Tognetti, and W. J. Book, "Experimental evaluation of a new braking system for use in passive haptic displays," *American Control Conference*, (San Diego, California), June 1999.
- [18] Sakaguchi, Masamichi, Junji Furusho, and Naoyuki Takesue, "Passive Force Display using ER brakes and its control experiments," *Proceedings of the IEEE Virtual Reality Conference*, (Yokohama, Japan), March 2001.
- [19] Schneider, O., J. Troccaz, O. Chavanon, and D. Blin, "PADyC: a synergistic robot for cardiac puncturing," *Proceedings of the IEEE International Conference on Robotics and Automation*, (San Francisco, California), April 2000.
- [20] Scilingo, Enzo P, Antonio Bicchi, Danilo De Rossi, and Adriano Scotto, "A magnetorheological fluid as a haptic display to replicate perceived biological tissue compliance," *International IEEE-EMBS Special Topic Conference on Microtechnologies in Medicine and Biology*, (Lyon, France), October 2000.
- [21] Swanson, Davin K. and Wayne J. Book, "Obstacle avoidance methods for a passive haptic display," *Proceedings of the IEEE/ASME International Conference on Advanced Intelligent Mechatronics*, (Como, Italy), July 2001.
- [22] Swanson, Davin K., *Dynamic Simulation of an Improved Passive Haptic Display*, Master's thesis, Georgia Institute of Technology, May 1999.
- [23] Swanson, Davin K., *Implementation of Arbitrary Path Constraints Using Dissipative Passive Haptic Displays*, PhD thesis, April 2003.

- [24] Tognetti, Lawrence J., *Actuator Design for a Passive Haptic Display*, Master's thesis, Georgia Institute of Technology, June 1999.
- [25] Tsai, Lung-Wen, *Robot Analysis: The Mechanics of Serial and Parallel Manipulators*, Wiley, New York, 1999.
- [26] Vallabh, Priya, *Electrorheological Brake for Haptic Interface Systems*, Master's thesis, Georgia Institute of Technology, August 2002.